FAULT-CONTROLLED ADVECTIVE, DIFFUSIVE, AND ERUPTIVE CO2 LEAKAGE FROM NATURAL RESERVOIRS IN THE COLORADO PLATEAU, EAST-CENTRAL UTAH

by

Na-Hyun Jung

A Thesis Submitted in

Partial Fulfillment of the

Requirements for the Degree of

Master in Science

in Geosciences

at

The University of Wisconsin-Milwaukee

December 2014

ABSTRACT

FAULT-CONTROLLED ADVECTIVE, DIFFUSIVE, AND ERUPTIVE CO2 LEAKAGE FROM NATURAL RESERVOIRS IN THE COLORADO PLATEAU, EAST-CENTRAL UTAH

by

Na-Hyun Jung

The University of Wisconsin-Milwaukee, 2014
Under the Supervision of Professor Weon Shik Han, PhD

This study investigated a natural analogue for CO_2 leakage near Green River, Utah, aiming to understand the influence of various factors on CO_2 leakage and to reliably predict underground CO_2 behavior after injection for geologic CO_2 sequestration. Advective, diffusive, and eruptive characteristics of CO_2 leakage were assessed via a soil CO_2 flux survey and numerical modeling. The field results show anomalous CO_2 fluxes (> 10 g m^{-2} d^{-1}) along the faults, particularly adjacent to CO_2-driven cold springs and geysers (e.g., 36,259 g m^{-2} d^{-1} at Crystal Geyser), ancient travertines (e.g., 5,917 g m^{-2} d^{-1}), joint zones in sandstone (e.g., 120 g m^{-2} d^{-1}), and brine discharge zones (e.g., 5,515 g m^{-2} d^{-1}). Combined with similar isotopic ratios of gas and progressive evolution of brine chemistry at springs and geysers, a gradual decrease of soil CO_2 flux from the Little Grand Wash (LGW; ~36,259 g m^{-2} d^{-1}) to Salt Wash (SW; ~1,428 g m^{-2} d^{-1}) fault zones reveals the same CO_2 origin and potential southward transport of CO_2 over 10-20 km.

The numerical simulations exhibit lateral transport of free CO_2 and CO_2-rich brine from the LGW to SW fault zones through the regional aquifers (e.g., Entrada, Navajo, Kayenta, Wingate, White Rim). CO_2 travels predominantly as an aqueous phase (X_{co2}=~0.045) as previously suggested, giving rise to the convective instability that further accelerates CO_2 dissolution. While the buoyant free CO_2 always tends to ascend, a fraction of dense CO_2-rich brine flows laterally into the aquifer and mixes with the formation fluids during upward migration along the fault. The fault always enhances advective CO_2 transport regardless of its permeability (k). However, only low-k fault prevents unconditional upright migration of CO_2 and induces fault-parallel movement, feeding the northern aquifers with more CO_2. Low-k fault also impedes lateral southward fluid flow from the northern aquifers, developing anticlinal CO_2 traps at shallow depths (<300 m). The regional k of the LGW fault in which CO_2 flux coincides with the field spatial variation is estimated between $0.01 \leq k_h < 0.1$ md and $0.5 \leq k_v < 1$ md. The anticlinal trap serves as an essential fluid source and conducive environment for intensifying eruption at Crystal Geyser. Geyser-like discharge in the simulations sensitively responds to varying well permeability and radius, and CO_2 recharge rate. Indeed, the cycling behavior of wellbore CO_2 leakage turns into a constant discharge with time, indicating the potential switch of Crystal Geyser to a CO_2-driven cold-water spring or even fumarole.

TABLE OF CONTENTS

LIST OF FIGURES

LIST OF TABLES

ACKNOWLEDGEMENTS

I owe my deepest gratitude to Dr. Weon Shik Han, without whom this astonishing project would not have been possible. His consistent encouragement, support and hard work led me to comprehend what being a scientist truthfully means; it has been an honor and privilege to work with him these past two years. I would also like to appreciate Dr. Timothy Grundl, Dr. Dyanna Czeck, and Dr. John Isbell for their invaluable and insightful guidance throughout this process.

Next, I thank Zach Watson, Jack Graham, and Cheng Thao for their assistance in collection of soil gaseous CO_2 flux in addition to their generosity and hospitality in the field. I am also grateful to Ethan Guyant for proofreading my writings as well as Zach and Jack. Additional thanks to Dr. Kue-Young Kim at Korea Institute of Geoscience and Mineral Resources and Dr. Eungyu Park at Kyungpook National University for their scientific and valuable advice on scientific research and writing. Dr. Woonsup Choi and Dr. Hyejin Yoon at the UWM Geography Department, and Dr. Changsoo Kim at the UWM Materials Science and Engineering Department are also to be thanked for their hearty support.

I would also like to thank the National Science Foundation, Korea National Oil Corporation, Korea Institute of Energy Technology Evaluation and Planning, Geological Society of America, and UWM Geosciences Department for financial support.

Lastly, I would like to deeply appreciate my parents, Nami and Hyungseok, my brother, Inseong, my hubby, Munseok Lee, Dr. Nam-Chil Woo at Yonsei University, Kyungdoe Han, Jah-Yeing Ahn, Hyun A Lee, Sung-uk Min, Junehyuck Jeon, Rina Kim,

Sujeong Yi, Julianna Mari, Adrianna Avery, and Lisa Alzalde, who have supported me with no question. Mom and Dad, thank you for teaching me to work my hardest for what I want; Dr. Nam-Chil Woo, my academic father, thank you for recommending and encouraging me to study in a bigger world; and Munseok, my dear, thank you for convincing me I could do this, even when I thought I couldn't. It was your encouragement and faith in me that made this project possible.

1. Introduction

An increasing demand for abating global climate change has led to enormous support for scientific studies and projects on reduction of CO_2 concentration in the atmosphere (IPCC, 2007). Among variable abatement strategies, geologic CO_2 sequestration (GCS) has been regarded as one likely method to diminish anthropogenic CO_2 emissions to atmosphere (Bachu, 2000; Celia and Bachu, 2003; Gale, 2004; Reichle et al., 1999). This includes the injection and storage of CO_2 in geologic formations at a depth below 800 m. Deep saline aquifers, depleted oil and gas reservoirs, and even coal formations are commonly proposed formations suitable for GCS (Anderson and Newell, 2004; Holloway, 2005; IPCC, 2005). In particular, deep porous reservoirs saturated with brine are well known for the most potential GCS sites because of their large storage potential and widespread locations throughout the world (Birkholzer et al., 2009; Castelletto et al., 2013; Gale et al., 2001; Oldenburg and Rinaldi, 2011). Indeed, deep saline formations are estimated to have a global storage capacity of at least 1,000 $GtCO_2$ and even up to 11,000 Gt, favorably compared with total annual emissions from global power production of 24 $GtCO_2$ (IPCC, 2005; White et al., 2003).

Both industrial and natural analogues have demonstrated that CO_2 can be safely segregated within subsurface reservoirs for a desirable time spanning at least a few hundred years under appropriate management (Allis et al., 2001; Anderson and Newell, 2004; Benson et al., 2002; Carey et al., 2007; Haszeldine et al., 2005; Korbøl and Kaddour, 1995; Rochelle et al., 1999). However, there still remain uncertainties about sealing integrity for GCS despite an abundance of research on this promising technology.

The main concerns that could significantly threaten the completeness of GCS involve potential CO_2 leakage; if flow paths (e.g., faults, fractures, and boreholes) unrecognizable at the stage of site screening process are present in and/or near stored formations, CO_2 could migrate away from a storage site and eventually reach the surface. Once CO_2 leakage begins, the leakage processes are likely to be amplified by self-enhancing feedbacks (e.g., the large mobility of CO_2 due to its low viscosity and density, further density decrease driven by volumetric expansion with declining pressure, and increase in porosity and permeability by mineral dissolution) even though it is also suppressed by self-limiting feedbacks (e.g., decrease in fluid mobility under multiphase conditions, reduction of porosity and permeability by mineral precipitation, and temperature drop due to Joule-Thomson expansion and phase transitions between liquid and gaseous CO_2) (Gherardi et al., 2007; Pruess, 2008a; Pruess and García, 2002). In other words, a significant amount of injected CO_2 could emanate back to the atmosphere until it stops by self-limiting processes or other external factors.

CO_2 leakage after a failure of stored sites could be accompanied by successive contamination of natural reserves such as shallow potable groundwater. For instance, although below a hazardous level, a rapid and progressive degradation of shallow groundwater was evidently observed after 300 kg/d of CO_2 injection for a month through a perforated pipe arranged horizontally at 2-2.3 m depths at the Zero Emission Research and Technology (ZERT) field site, Montana, USA; pH was lowered from 7.0 to 5.6 while the concentrations of the trace metals and BTEX increased (e.g., Ca, 90-240 mg/l, Fe 5-1,200 ppb, and benzene, 0-0.8 ppb) (Kharaka et al., 2010). In addition, influx of CO_2-rich brine from depth led to local contamination of groundwater with Na, Cl and trace metal

(e.g., Fe, As, U) concentrations exceeding US EPA drinking water standards at a shallow sandstone aquifer of the Tesuque Formation of Santa Fe Group near Chimayó in New Mexico, USA (Keating et al., 2010).

While CO_2 leakage can result in a vain effort to reduce CO_2 emission, adverse health effects on the public and the environment could also arise due to spatially and/or temporally elevated CO_2 concentration (Lewicki et al., 2007). Various examples of the lethal effect of CO_2 leaks are found around the world: the gas burst at Lake Monoun, Cameroon in 1984 (Sigurdsson et al., 1987), the catastrophic CO_2 degassing at Lake Nyos, Cameroon in 1986 (McCord and Schladow, 1998), and the slow but steady release of CO_2 gas at Mammoth Mountain, California, USA in 1990 (Farrar et al., 1995; Rogie et al., 2001). Therefore, CO_2 dynamics in the subsurface must be well understood for a proper risk assessment of possible leakage of injected CO_2 and a subsequent optimal deployment of GCS (Siirila et al., 2012).

Dynamics of leaking CO_2 have been investigated many times over the last two decades (IPCC, 2005) via two chief approaches: (1) field-oriented studies of natural and industrial analogues such as CO_2 natural reservoirs (Allis et al., 2005a; Glennon and Pfaff, 2005; Han et al., 2013a; Kampman et al., 2014b; Lewicki et al., 2003; Shipton et al., 2005), volcanic and geothermal areas (Lu et al., 2005; Roberts et al., 2011; Rogie et al., 2000), and CO_2 injection sites (Arts et al., 2008; Carey et al., 2007; Kharaka et al., 2010; Klusman, 2005; Smyth et al., 2009), and (2) numerical modeling on the basis of the governing physical, chemical, and thermodynamic processes (Castelletto et al., 2013; Gherardi et al., 2007; Han et al., 2010a; Han et al., 2010b; Oldenburg et al., 2010; Oldenburg et al., 2001; Oldenburg and Rinaldi, 2011; Pruess, 2008a; Taku Ide et al.,

2007; Tueckmantel et al., 2012). Indeed, valuable lessons about the key characteristics of long-term CO_2 flow behavior can be obtained from both naturally leaking and artificially injected fields for GCS, enhanced oil recovery (EOR) or enhanced coal bed methane (ECBM), which cannot be replicated readily by laboratory experiments (Benson et al., 2002; Lewicki et al., 2007; Pearce et al., 2004).

Numerical modeling approaches can provide a further understanding of post-injection behavior of CO_2 in both space and time. They also present advantageous tools that make it easy to handle and test the effects of different parameters (Class et al., 2009; Han et al., 2011; Mukhopadyay et al., 2012). However, there have been a few studies that thoroughly investigated the main features of CO_2 leakage by combining field study with numerical modeling. Most of those studies focused on industrial analogues such as EOR or ECBM, which have been operated for less than a hundred years. The research preferences on industrial repositories may be attributed to abundant data attained from detailed investigations during exploration and production of fossil fuels over multiple decades at CO_2-EOR and -ECBM sites rather than at natural CO_2 fields. Nevertheless, without such investigation at natural analogues, the accurate and reliable prediction of CO_2 transport could be problematic over a sufficient time required for GCS (Benson et al., 2002; Haszeldine et al., 2005; Lewicki et al., 2007; Pearce et al., 2004).

The main objectives of this study are to elucidate coupled migration of CO_2 and CO_2-saturated brine in the subsurface, to quantify the roles of faults on CO_2 leakage with varying hydrogeologic parameters, and to define hydrogeologic conditions and mechanisms for the development of eruptive CO_2 leakage, i.e. CO_2-driven cold-water geyser. The crucial results of a field soil CO_2 gas survey at Green River in Utah at which

CO_2 has naturally leaked within fault zones for >400 ka (Burnside et al., 2013; Kampman et al., 2012) were presented by Jung et al. (2014). They implied the nature of the Little Grand Wash (LGW) and Salt Wash (SW) faults as conduits for upflow and barriers for horizontal flow of CO_2 with low permeability. Nevertheless, a detailed range of regional fault permeability was not identified. In this study, different scenarios of the subsurface CO_2-brine migrations within the LGW fault zone over time were investigated by numerical simulations. The` results were validated with the field CO_2 flux, allowing reasonable estimates of regional permeability of the LGW fault. Finally, the conditions for the formation of CO_2-driven cold-water geyser were tested with varying hydrogeologic parameters, e.g., permeability of well and the surroundings, well radius and porosity.

2. Study Area Description

2.1. Geological Settings

The research area is one of the prominent sites for studying naturally-leaking CO_2 around the world (Glennon and Pfaff, 2005; Lewicki et al., 2007; Price et al., 2007) and located at the northwestern edge of the Paradox Basin near Green River in East-Central Utah (Fig. 1). Similarly to typically proposed geologic CO_2 sequestration sites (IPCC, 2005; Shipton et al., 2005), sedimentary rocks constitute of the Paradox Basin with multiple aquifers and their intervening aquitards. There exist 6 major aquifers in this area: the Permian White Rim Sandstone, the Lower Jurassic Wingate/Kayenta/Navajo Sandstones, and the Middle Jurassic Entrada/Curtis Formations (Kampman et al., 2014b;

Shipton et al., 2004). Each aquifer is capped by the aquitards such as the Triassic Moenkopi/Chinle/Carmel Formations, and the shale-rich lower part of the Entrada Sandstone, and the Middle Jurassic Summerville Formation. The region also contains two major fault systems: the LGW and SW faults (Fig. 1). The arcuate LGW fault is made of two parallel strands nearby the Green River while two normal fault systems of the SW fault forms a shallow graben long striking N 70° W. Both the faults cut the gently north plunging Green River Anticline, dipping 70-80° south except the southernmost normal fault of the SW graben which dips 70-80° north. Timing of continued movement along these faults is poorly known, though estimated as Early Tertiary and Quaternary slip (Shipton et al., 2004). Though the areas of outcropped faults are very restricted, Dockrill and Shipton (2010) found that the faults are dominated by foliated clay-rich gouges (0.7 to 3 m thick) with highly-fractured damage zones (~20 m thick).

Interestingly, a series of CO_2-driven geysers and springs, active and fossil travertines, and carbonate veins are present along both the LGW and SW fault traces (Fig. 1), implying fault-controlled CO_2 leakage. Crystal Geyser is an abandoned well drilled for oil exploration in the mid 1930's within the LGW fault zone (Baer and Rigby, 1978; Gouveia and Friedmann, 2006). It has displayed periodic, intense eruptions of CO_2 and brine ($4.77 \pm 1.92 \times 10^3$ tCO_2/yr estimated in Watson et al. (2014)), depositing travertines. However, consistent changes in eruption interval, duration, and height from the surface suggest that eruption intensity at Crystal Geyser has decreased for several decades (Han et al., 2013a; Watson et al., 2014). U-Th dating of travertines and embedded veins reveal that CO_2 has constantly leaked to the surface for >400 ka; yet spatially dispersed travertines with different volumes indicate that the location of CO_2

leakage has varied depending on permeability alteration of each unit due to mineral precipitation, seismic activities, climate changes and regional unloading (Burnside et al., 2013; Kampman et al., 2012). Consequently, the study area provides an unparalleled natural analogue for long-term CO_2 leakage after a failure of GCS.

2.2. CO_2 and Brine Origins

Many studies have documented deep crustal CO_2 origins in this area using chemical and isotopic analyses of CO_2 gas and brine, which were emitted from springs and geysers, as well as travertines and carbonate veins. Mayo et al. (1991) reported enriched $\delta^{13}C$ of -1.2 ‰ in HCO_3^- at Crystal Geyser and suggested CO_2 production by thermal decomposition of carbonate rocks. This observation coincides with the fact that CO_2 gas is produced via thermal decarbonation of the Mississippian Leadville Limestone at the McElmo Dome that also lies on the Paradox Basin in southern Colorado (Cappa and Rice, 1995). Shipton et al. (2004) found further enriched $\delta^{13}C$ ranging +4 ‰ to +5 ‰ from travertines and veins along with Crystal Geyser, Tenmile Geyser, and Torrey's Spring, also indicating thermal degradation of carbonates. Potential CO_2 production by contact metamorphism in the vicinity of Crystal Geyser, resulting from the heat of Tertiary intrusions into marine carbonates deposited beneath the Middle Pennsylvanian Paradox Formation, is also possible. Heath et al. (2009) concluded that CO_2 was generated by thermal decarbonation and/or clay-carbonate reaction in the deep crust (>800 m depth), based upon their measurement of relatively high $\delta^{13}C$ (from -6.42 ‰ to -6.76‰) and low $^3He/^4He$ (0.3 R_a) of gas samples from every spring and geyser.

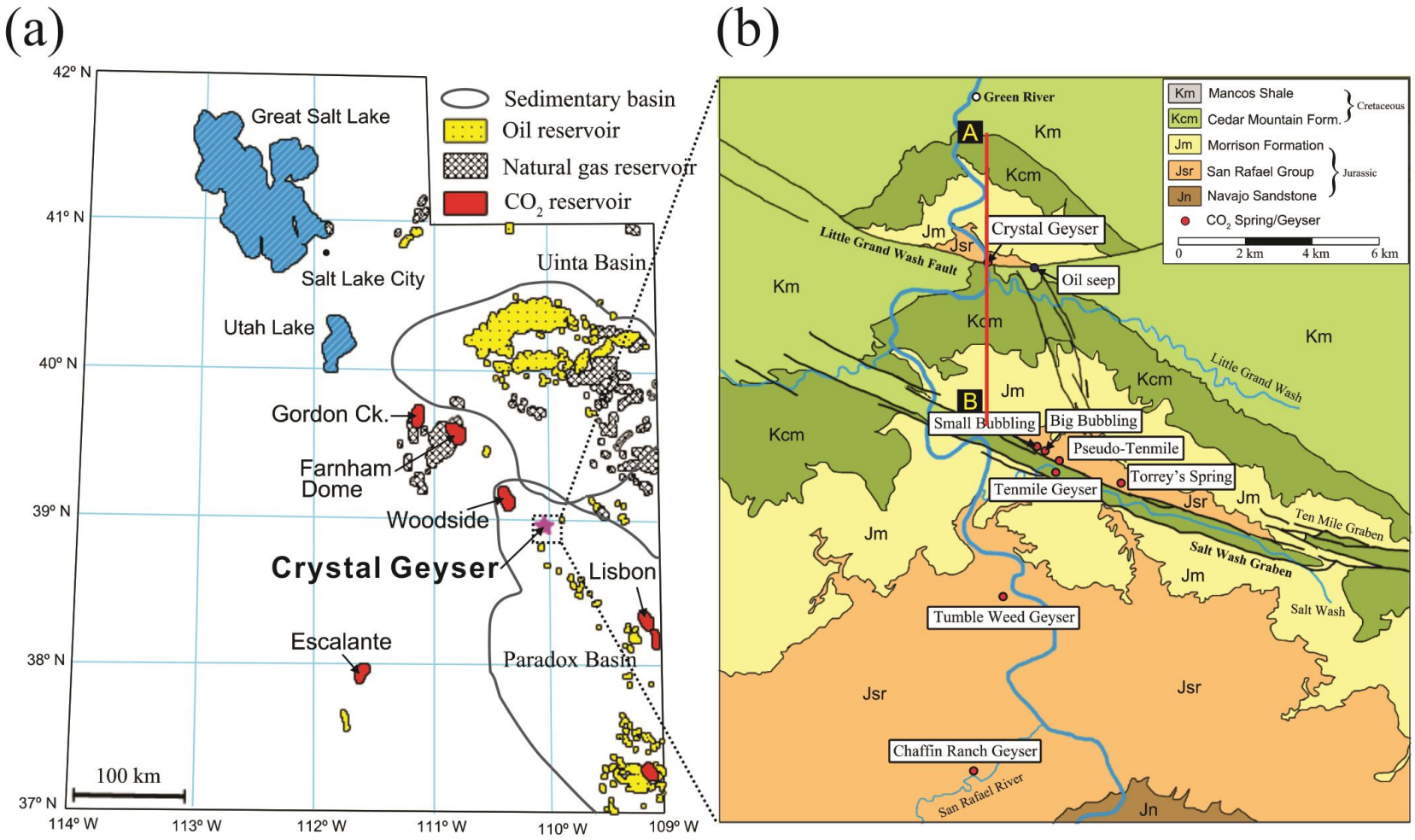

Figure 1. A geological setting of the study area. (a) A map shows the spatial distribution of oil, natural gas and CO_2 fields in Utah (Chidsey et al., 2004; Han et al., 2013b). The study area is indicated by a dotted box. (b) Locations of CO_2 springs/geysers with the LGW and SW fault traces (black heavy lines) in the study area (modified from Dockrill and Shipton (2010); Doelling (2002); Kampman et al. (2009)).

Chemical profiles of fluid were recently analyzed at a scientific hole drilled ~90 m north of the main trace of LGW fault and ~285 m west of Crystal Geyer (Kampman et al., 2014a; Kampman et al., 2014b). Analyses of *in situ* water chemistry suggested that CO_2 may originate from the deep reservoirs (>2 km depth) and migrate through the LGW fault mostly as a dissolved phase in brine to feed the local shallow aquifers (Navajo and Entrada Sandstones). These aquifers would host free CO_2 for the area by exsolution due to the reduced solubility of CO_2 with decreasing depth (Wilkinson et al., 2009). These CO_2 degassing processes explain well the enriched $\delta^{13}C$ values for both brine (from -0.94 ‰ to -0.19 ‰) and CO_2 gas (from -7.55 ‰ to –6.61 ‰) (Assayag et al., 2009; Kampman et al., 2009). Nonetheless, the aquifers are also likely to be fed by CO_2-undersaturated meteoric groundwater, which recharges from the San Rafael Swell and flows from northwest to southeast (Fig. 2) (Baer and Rigby, 1978; Hood and Patterson, 1984).

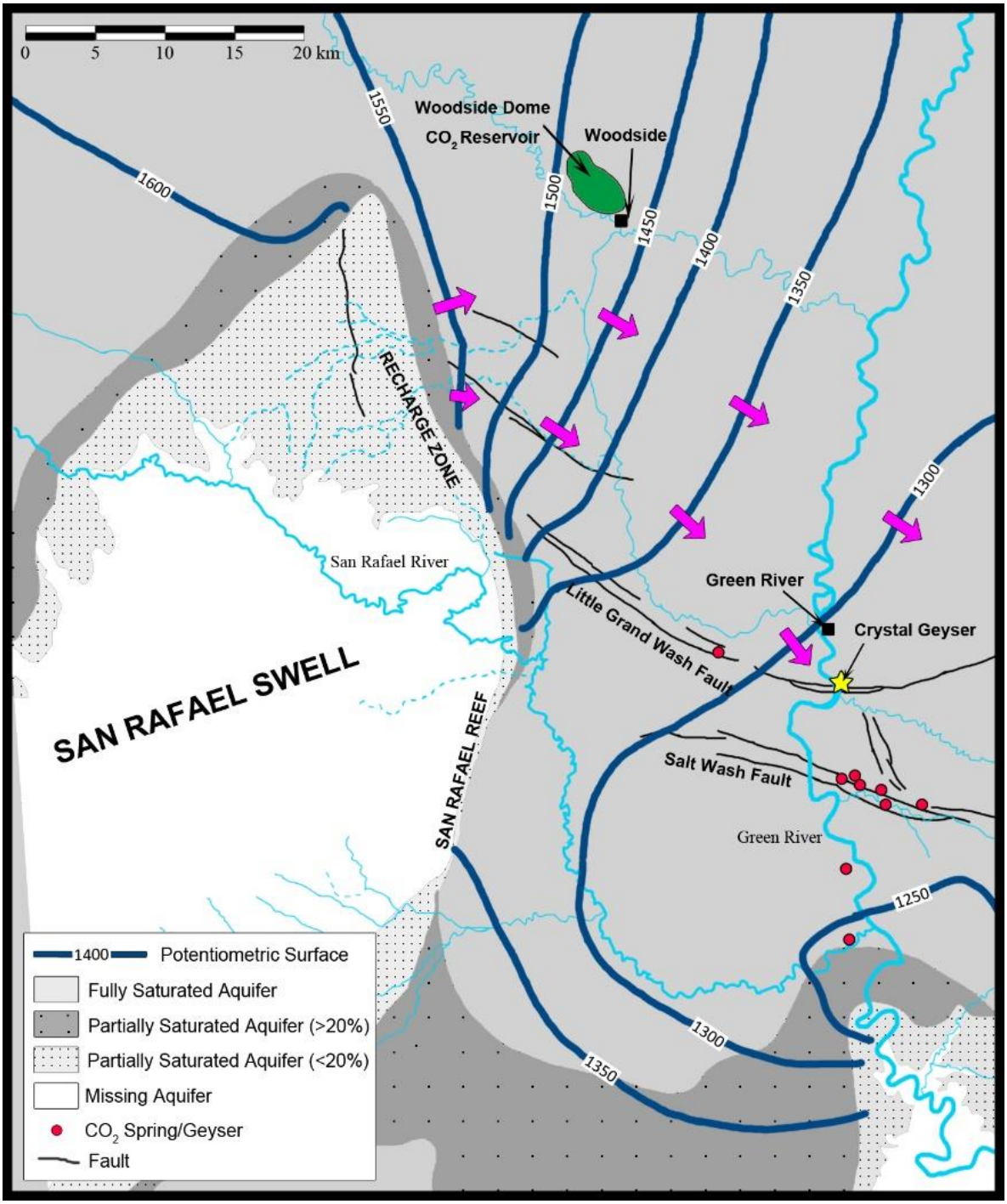

Figure 2. The potentiometric surface (m) for the Navajo Sandstone in East-Central Utah. Note that meteoric groundwater recharges by percolation to the exposed Navajo Sandstone along the east side of the San Rafael Swell and flows southeastward (pink arrows) to the study area [Baer and Rigby, 1978] (modified from Hood and Patterson [1984] and Kampman et al. [2009]).

2.3. Historical Variations in Crystal Geyser Eruption

Crystal Geyser, initially referred to as Glen Ruby #1-X, extends to approximately 800 m depth near the crest of the Green River anticline within the Paradox Basin, Utah (Fig. 1a). It is only cased at the surface, a height of 1.73 m and diameter of 0.39 m. Manifesting a very unique feature of massive and periodic eruption of cold CO_2-brine mixtures, Crystal Geyser has been widely investigated in both quantitative and qualitative fashions to figure out its specific mechanisms (Glennon and Pfaff, 2005; Gouveia and Friedmann, 2006; Han et al., 2013a; Kampman et al., 2014b; Kelsey, 1991; Shipton et al., 2005; Watson et al., 2014). Their results indicate that eruption patterns of Crystal Geyser have significantly varied over time since it was drilled (Fig. 3a). At first in 1936, the geyser was reported to exhibit very intensive and bimodal eruption, reaching a height of 25-45 m from the surface (Kelsey, 1991). The eruption changed to unimodal with a decrease in its intensity (21-27 m high) in 1968 and 1972 when Baer and Rigby (1978) tried to prevent saline water discharge from Crystal Geyser to the Green River. Until then, an average eruption interval was below 5 hr with a short-duration of <10 min (Fig. 3a). However, in the late 1980's, Murray (1989) reported less intensive eruption with a relatively prolonged interval (13-15 hr) and duration (16-25 min). Accordingly, the lowest eruption height was reduced (18 m) while the maximum height was still large (40 m). At present, the eruption still remains unimodal but with a much longer interval (72-87 hr) and duration (25-28 hr), showing a constant decrease of vigor in eruption (Han et al., 2013a; Watson et al., 2014) (Fig. 3a).

Remarkable advances to improve an understanding of CO_2-driven geysering processes have recently been made via in-well measurements of Crystal Geyser (Han et

al., 2013a; Kampman et al., 2014b; Watson et al., 2014). Han et al. (2013a) presented the first measurements of *in situ* pressure and temperature (6 and 14.5 m depth) in 2010 and unveiled a consistent cycle comprised of two major and minor eruptions with two intervening recharge periods. Watson et al. (2014) also recorded pressure and temperature within the wellbore at 6 m depth in 2013, showing a new 4-part eruption cycle composed of minor and major eruption (mEP and MEP), after shock (Ae) and recharge (R) periods (Fig. 3b). Based on their *in situ* observations, Han et al. (2013a) and Watson et al. (2014) provided a convincing conceptual model of geyser mechanism, highlighting a vigorous increase of bubble volume fraction with increasing flash depth as eruption proceeds. Kampman et al. (2014b) chemically analyzed temporal fluid samples from Crystal Geyser and found rapid declines in salinity, temperature, and radioactivity of fluid with the outset of a large-scale eruption, revealing changes in fluid sources from the deeper Navajo to shallower Entrada Sandstone.

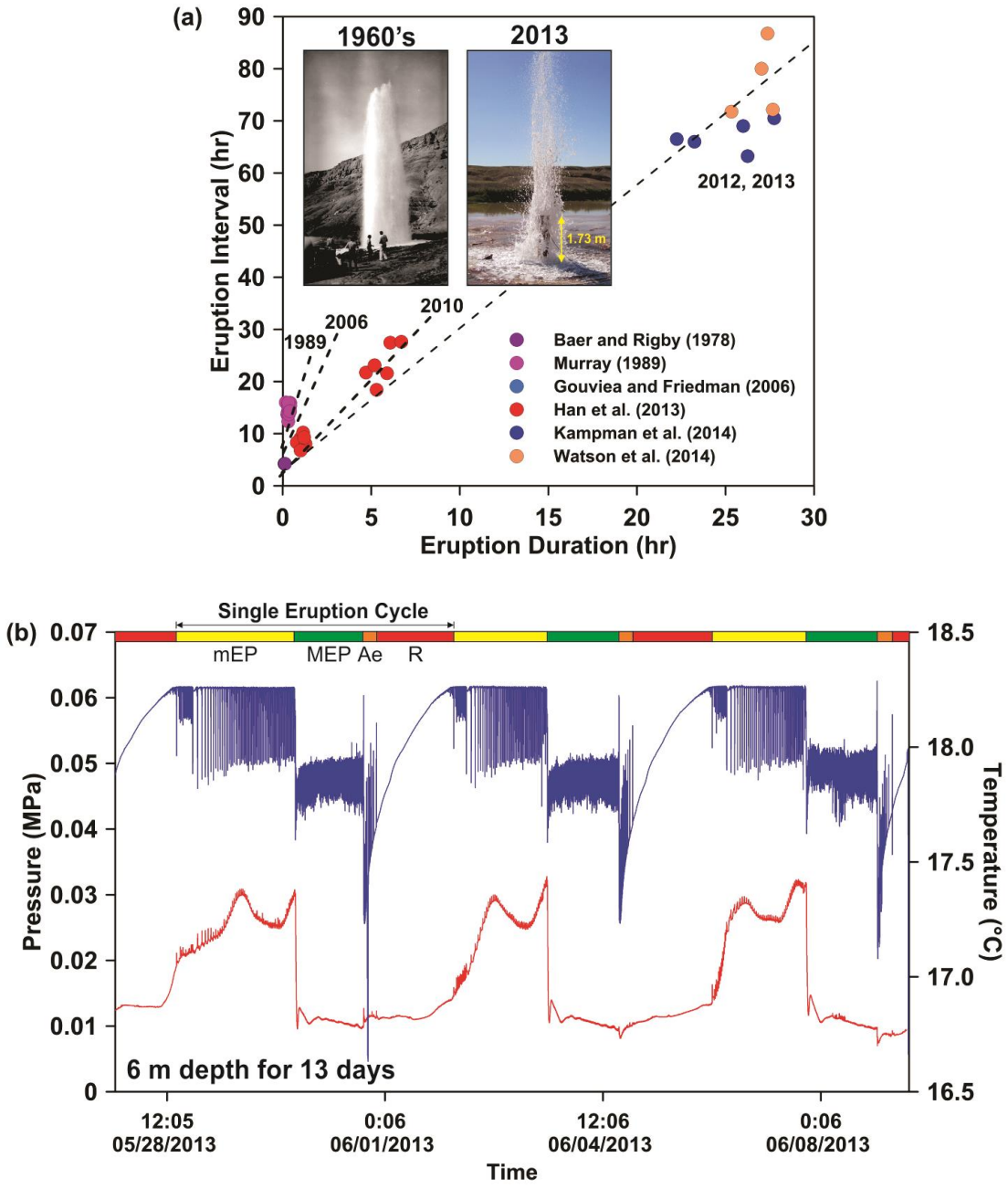

Figure 3. Historical variations in eruption pattern of Crystal Geyser (a) Comparison of eruption intervals to durations with their trends (dashed lines) and two photos of Crystal Geyser taken in the 1960's (provided by John Wesley Powell River History Museum in Green River, Utah) and 2013. (b) Periodicity of Crystal Geyser represented by *in situ* pressure and temperature measured at 6 m depth for 13 days in 2013. Single eruption cycle consists of minor eruption period (mEP), major eruption period (MEP), aftershock eruptions (Ae), and recharge (R).

3. Field CO_2 Flux Monitoring

3.1. Methods

Soil gas CO_2 flux was measured over a period of 8 days in 2010 (August 4-6/September 1-5) and 24 days in 2013 (May 23-June 15) to identify where the anomalous CO_2 flux would be found in the fault zones. The survey was undertaken using an automated soil CO_2 flux measurement system, LI-COR 8100A. An open-bottomed chamber was placed on a PVC collar (outside diameter of 21.34 cm, inside diameter of 20.3 cm, and 20 cm high) partially inserted into the soil; then, an infrared gas analyzer (measurement accuracy = 1.5% of its reading) measured the changes in CO_2 and H_2O concentrations in the soil chamber for 2-3 minutes at each site in order for the system to be stabilized. Measurements were made consistently during the daytime between 9 AM and 4 PM, minimizing diurnal variances of fluxes. The CO_2 flux, F (g m^{-2} d^{-1}), was calculated by equation (1)

$$F = k\frac{10VP_0\left(1-W_0/1000\right)}{RS\left(T_0+273.15\right)}\frac{d\left[CO_2\right]}{dt}, \quad (1)$$

in which k is a unit conversion constant (3.80 g s μmol^{-1} d^{-1}), V is the system volume (cm^3), R is the universal gas constant (8.31 m^3 Pa K^{-1} mol^{-1}), S is the soil surface area (cm^2; herein, 317.8 cm^2 for a 20 cm diameter chamber), P_0 is the initial pressure (kPa), T_0 is the initial air temperature (°C), W_0 is the initial water vapor mole fraction (mmol mol^{-1}), and $d[CO_2]/dt$ is the initial rate of change in water-corrected CO_2 mole fraction (μmol mol^{-1} s^{-1}).

Measurement sites for CO_2 flux were chosen based upon accessibility, exposed or discernible configurations of the faults and joints/fractures, and the presence of CO_2-driven springs/geysers, travertine and carbonate veins. The selected sites included structural highs and steep travertine mounds between washes unlike the survey from Allis et al. (2005b) whose sites were located solely in washes. A total of 332 (= 0 to 36,259 g m^{-2} d^{-1}) and 140 measurements (= 0 to 1,428 g m^{-2} d^{-1}) of CO_2 flux were taken at 287 and 129 multiple locations in the LGW and SW fault zones, respectively.

Raich and Schlesinger (1992) found typical CO_2 respiration rates of 10-20 g m^{-2} d^{-1} in temperate grasslands, croplands, and tropical savannas. Allis et al. (2005b) reported the background CO_2 flux of ~5 g m^{-2} d^{-1} in arid regions with poor vegetation; however, wet ground with heavy vegetation at Springerville-St. Johns gave higher background CO_2 flux of ~20 g m^{-2} d^{-1}, which results from shallow root zone activity. In this study, hot and hyper-arid weather continued with daytime temperatures from 20 to 34 °C throughout the survey period and desert vegetation scarcely covered the study area. Therefore, background CO_2 fluxes resulting from bioactivities in soil were assumed to range from 0 to 10 g m^{-2} d^{-1}. In addition, when the measured CO_2 fluxes were anomalously high (>10 g m^{-2} d^{-1}), multiple measurements were conducted to assure CO_2 flux anomalies and then the arithmetic mean was taken as a representative CO_2 flux.

After the survey, CO_2 fluxes were analyzed in both north-south and east-west directions. Spatial variations of CO_2 flux were determined in terms of values of maximum, minimum, median and selected percentiles (10%, 25%, 75%, and 90%). A correlation with the faults being of the main interest, various factors were simultaneously considered with CO_2 flux anomalies (e.g., surface elevation, location/age/volume of

travertines, joint/fracture/groundwater discharge zones, CO_2-spring/geysers). Henceforth, an interrelation of CO_2 concentration and flux was investigated in each fault zone in order to account for a diffusive/advective transport of CO_2. Finally, a conceptual model that illustrates leakage processes of CO_2 on a regional scale was developed in the both LGW and SW fault zones.

3.2. Little Grand Wash (LGW) Fault Zone

In the LGW fault zone, the anomalous fluxes (>10 g m^{-2} d^{-1}) appeared within ~20 m of the LGW fault traces (Fig. 4). Indeed, 74% of CO_2 flux anomalies were localized in the northern footwall of the LGW fault. The extraordinary CO_2 flux anomalies (>500 g m^{-2} d^{-1}) were observed in close proximity to both ancient (5-114 ka, Burnside et al. (2013)) and actively-depositing travertines, particularly where the dual fault traces nearly adjoined to each other. For example, an anomalous range of CO_2 fluxes (25-111 g m^{-2} d^{-1}) was found near the ancient L1 travertine across the river from Crystal Geyser (Fig. 4b). Other flux anomalies (67, 94, and 155 g m^{-2} d^{-1}) were also found where the fault outcropped.

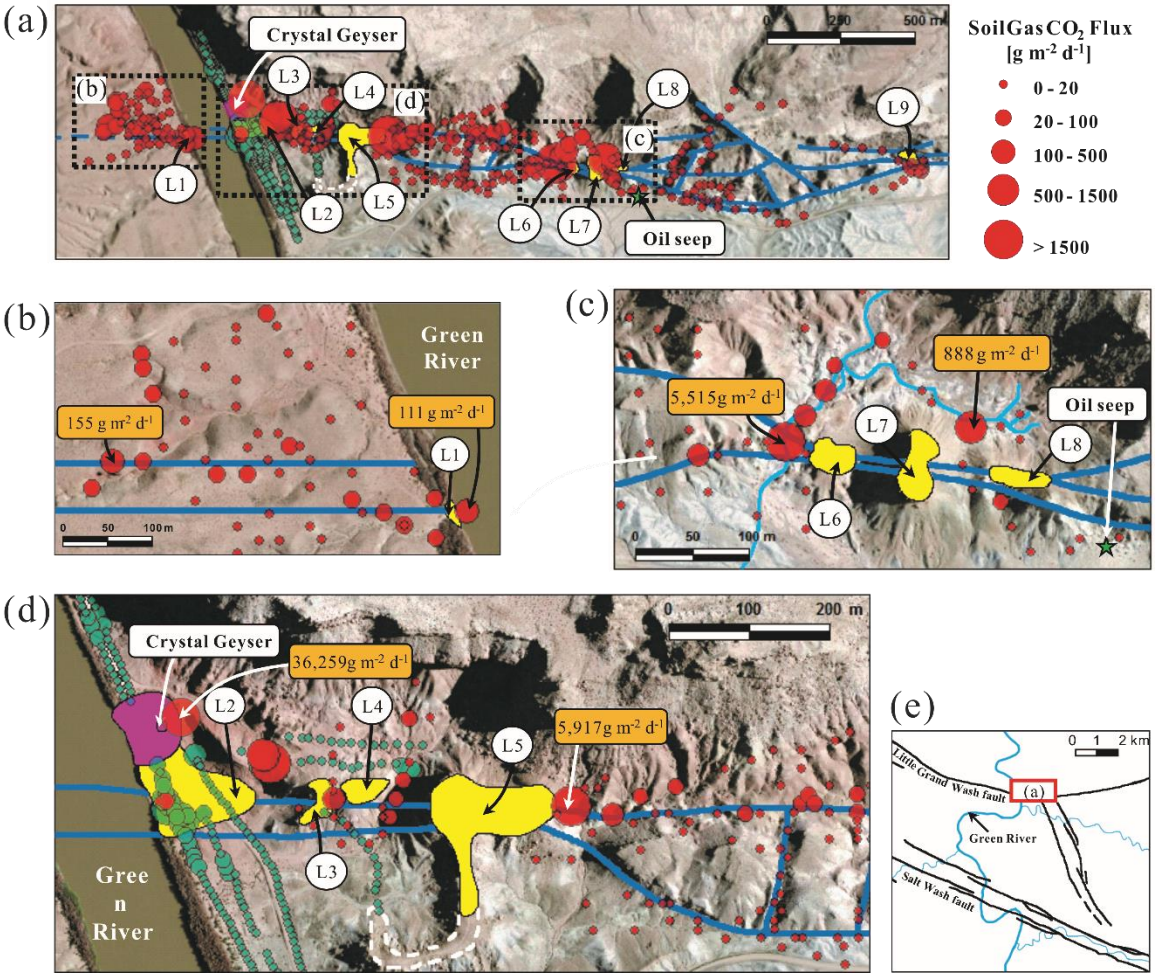

Figure 4. The spatial variations of soil gas CO_2 fluxes adjacent to travertines, fault traces, Crystal Geyser and an oil seep in the LGW fault zone. The fault traces are accentuated in navy blue, ancient travertine in yellow and active CO_2 springs and geysers in purple (Burnside, 2010). Soil gas CO_2 flux data were obtained during the field trip of May 23–June 15, 2013 (Red) and August 4–6 and September 1–5, 2010 (Green). (a) Overall CO_2 flux measurements taken within the LGW fault zone with locations of magnified maps (b), (c), and (d). (e) Location of soil CO_2 survey field (a) in the LGW fault zone, East-Central Utah.

Additional CO_2 flux anomalies were observed in the vicinity of Crystal Geyser where travertines are actively depositing due to periodic CO_2 and brine eruptions (Fig. 4d). Anecdotal evidence from local residents suggests that there were mud pots ~5 m east of Crystal Geyser; however, water has dried up completely so that the mud pots were no longer observed during the CO_2 flux survey period. Herein, we refer to them as inactive mud pots. The most anomalous flux of 36,259 g m^{-2} d^{-1} was recorded at one of inactive

mud pots during non-eruption period at Crystal Geyser; moreover, we could hear CO_2 degassing at this mud pot just below the surface. However, soil gas CO_2 flux substantially decreased (2,124 g m^{-2} d^{-1}) by up to 94% of its maximum when the small-scale eruption occurred at Crystal Geyser. This suggests that the mud pots are connected to the geyser probably by a fracture network, allowing high surface CO_2 leakage at this location.

The low-lying surface at the northeastern end of the ancient L5 travertine, 0.5 km east of Crystal Geyser, showed the second largest CO_2 flux anomaly of 5,917 g m^{-2} d^{-1} (Fig. 4d). Further about 0.6 km to the east, anomalous CO_2 fluxes ranging from 84 to 5,515 g m^{-2} d^{-1} were measured along a wash entrenched generally in northwest of the ancient L6 travertine (Fig. 4c). These anomalous fluxes gradually increased towards downstream wash, closer to the fault traces. In addition to intermittent flow of upstream water, a small quantity of brine discharges consistently, prevents sand/mud from drying out, and concurrently leaves large amounts of salt deposits in the base of the wash.

Interestingly, an active petroleum seep lies immediately on the southernmost fault strand 80 m southeast of the travertine L8 (Fig. 4c), showing that there are leakage pathways for oil (Dockrill and Shipton, 2010; Shipton et al., 2004). However, despite the presence of conduits for oil, only background CO_2 fluxes ranging from 0 to 14 g m^{-2} d^{-1} were observed around the oil seep. As leakage pathways are highly isolated along the LGW fault (Burnside et al., 2013), it can be determined that low surface CO_2 leakage at this location is resulting from hydrocarbon biodegradation rather than upflow of deep-sourced CO_2. Further isotopic analyses of emitted gases are needed to clearly determine the source of CO_2 that vents near the oil seep.

3.3. Salt Wash (SW) Fault Zone

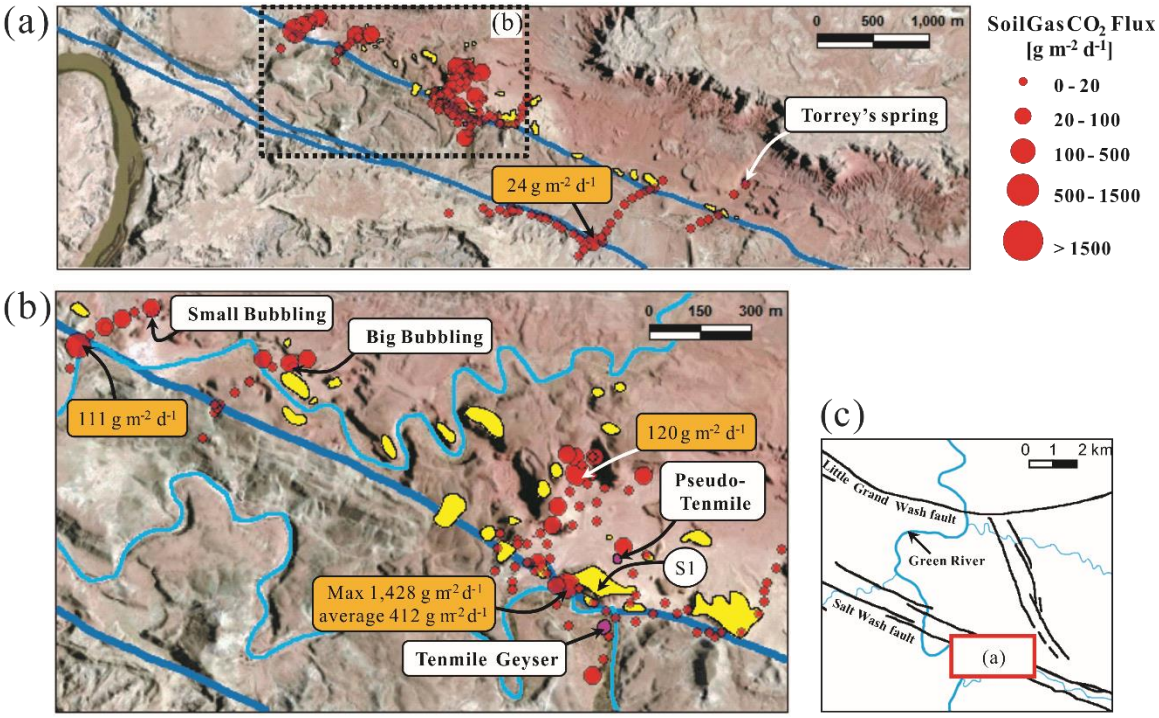

Figure 5. The spatial variations of soil gas CO_2 fluxes adjacent to travertines, fault traces, and springs/geysers in the SW fault zone. The fault traces are accentuated in navy blue, ancient travertine in yellow and active CO_2 springs and geysers in purple (Burnside, 2010). (a) Entire CO_2 flux measurements taken within the SW fault zone. (b) Magnified map in the vicinity of Pseudo-Tenmile, Tenmile Geyser, and Small/Big Bubbling Springs. (c) Location of soil CO_2 survey field (a) in the SW fault zone, East-Central Utah.

In the SW fault zone, most measurements were made proximal to the northernmost fault trace (Fig. 5a) since there was no noticeable manifestation of CO_2 leakage in the SW Graben except Tenmile Geyser (Shipton et al., 2005). Anomalous CO_2 fluxes were concentrated in the north side of the graben, whereas very low or no fluxes were dominant in the graben and on the southernmost fault trace akin to those found by Allis et al. (2005b). The most anomalous CO_2 flux with an average of 412 g m^{-2} d^{-1} was observed at the wet salt deposits on the base of a wash, which lies directly on the northern

fault trace next to the large ancient travertine S1 (Fig. 5b). Additional anomalous CO_2 fluxes of 78 and 34 g m^{-2} d^{-1} were measured at the north fault trace, about 30 m and 110 m northwest of this location, respectively. These observations suggest that the north fault trace in this region behaves as a conduit for upflow of CO_2 from the subsurface. Elsewhere along the northern fault trace, however, low fluxes of CO_2 <10 g m^{-2} d^{-1} were measured. Similarly, 25 measurements along the southern fault trace gave negligible CO_2 fluxes with an arithmetic mean value of 4.5 g m^{-2} d^{-1} except for one spot (24 g m^{-2} d^{-1}).

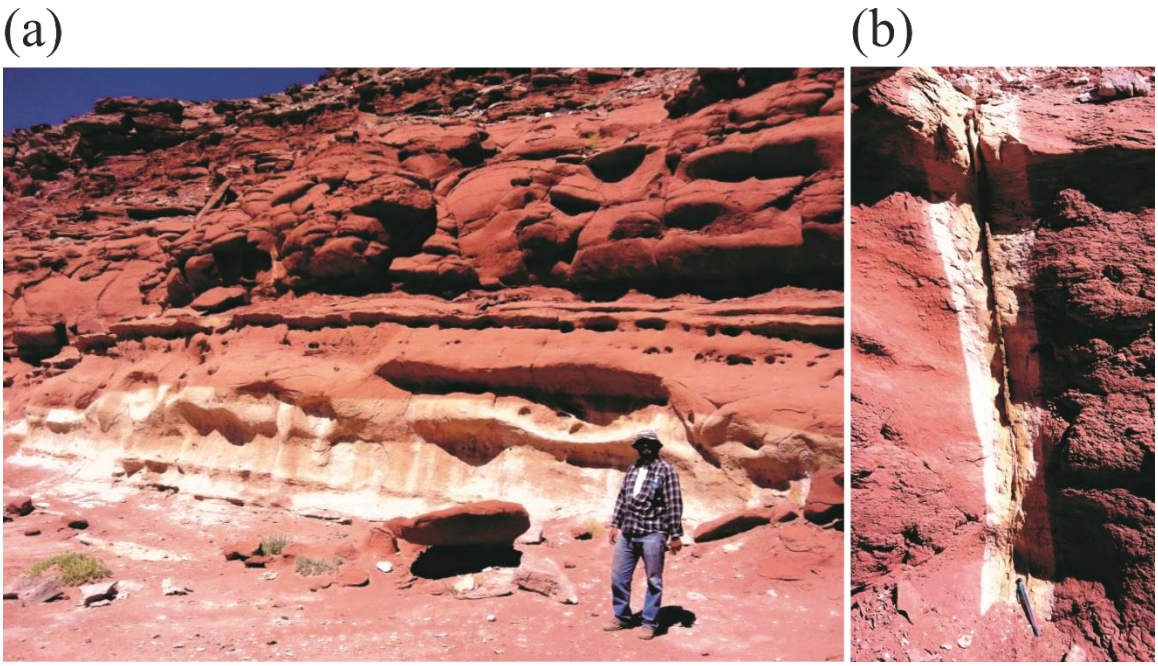

Figure 6. Bleached Entrada Sandstone in the northern footwall of the Salt Wash Graben by reduction of iron-oxide. (a) Extensive reduction of hematite with undulating front in the bottom unit of the Entrada Sandstone indicates that change in color is not associated with depositional controls. Upper unit was bleached only around fractures. (b) Reduction halos around a fracture in the bottom unit (a mechanical pencil 15 cm long).

Similarly to Allis et al. (2005b), CO_2 flux anomalies observed in this study do not always coincide with mapped fault traces. Instead, more anomalous fluxes of CO_2

ranging from 27 to 120 g m^{-2} d^{-1} appeared around joint zones within the bleached Entrada Sandstone exposed in the northern footwall (Fig. 6). Extensive and massive bleaching of the Entrada Sandstone from red to pale yellow is attributed to the reduction of hematite by reducing fluids (e.g., hydrocarbon) that migrated through fractures and joints (Dockrill and Shipton, 2010; Kampman et al., 2009; Wigley et al., 2013a; Wigley et al., 2013b; Wigley et al., 2012). Our detailed observations of CO_2 flux anomalies therefore indicate that CO_2 is still released through the fractures, the pathways for ancient reducing fluids. Two profiles obtained from Big Bubbling/Small Bubbling Springs traversing the fault trace showed similar spatial distribution of CO_2 flux anomalies adjacent to Crystal Geyser; substantial CO_2 was emitted not only from springs but also from surrounding ground and washes (Fig. 5b). Specifically, abnormal fluxes generally decreased further from springs. However, the profile near Small Bubbling Spring displayed an abrupt increase in the flux to 111 g m^{-2} d^{-1} at the fault trace and a subsequently sharp drop to zero across the fault trace. High fluxes also appeared adjacent Pseudo-Tenmile (25 g m^{-2} d^{-1}) but not in the vicinity of Torrey's Spring.

4. Numerical Simulations

4.1. Modeling Approach

4.1.1. Description of a Conceptual Model

As previously indicated by a number of studies, an ultimate driving force of CO_2 migration in the subsurface is buoyancy (Han et al., 2010b; Oldenburg and Unger, 2003;

Pruess, 2008a; Pruess and García, 2002; Taku Ide et al., 2007): lower density than water gives rise to the tendency for CO_2 to ascend buoyantly against gravity, which is reinforced by higher volumetric flow rate resulting from lower viscosity. In addition, larger compressibility of CO_2 compared to water results in much larger volume expansion during depressurization (Pruess, 2008a; Vilarrasa et al., 2010), resulting in further density decrease and saturation increase along flow paths. However, CO_2 upward movement is also subordinate to self-limiting effects: adiabatic volume expansion of CO_2 upon decompression accompanied by Joule-Thomson cooling (Han et al., 2010b; Mathias et al., 2010; Oldenburg, 2007; Pruess, 2008b). This cooling could cause phase transitions and thereby an evolution of a multiphase system with severe flow disturbance (Pruess, 2008b). Dissolution of CO_2 into water will also increase the amount of CO_2 trapped within reservoirs because aqueous CO_2 is not subject to buoyancy (Kneafsey and Pruess, 2010). Therefore, CO_2 leakage in the subsurface should be understood in terms of its thermodynamic, chemical and hydrodynamic properties under a given circumstance (Gherardi et al., 2007; Pruess, 2008a).

In order to demonstrate and characterize CO_2 leakage through faults and wellbores relating to hydrodynamic properties of faults and geysering processes, numerical simulations were performed using a TOUGH2-MP/ECO2N. This is a massively-parallel numerical simulator based on an integrated finite difference method and can simulate multiphase flow of H_2O-NaCl-CO_2 under typical reservoir conditions ($T \leq 100$ °C and $P \leq 60$ MPa) (Pruess et al., 1999; Zhang et al., 2008). Both isothermal and non-isothermal conditions were selectively chosen for the purpose of studies. For CO_2 flow through faults without geysering process, an isothermal assumption is legitimate

because CO_2 migration is not instantaneous enough to maintain adiabatic conditions. By contrast, non-isothermal processes are important for simulating the eruption of Crystal Geyser (Pruess, 2008a).

A 2-D numerical model was developed along the north-south cross section traversing Crystal Geyser and the LGW fault (Line AB in Fig. 1b), corresponding roughly to local geology of the study area (Fig. 7) (Heath et al., 2009; Shipton et al., 2004; Williams, 2005). The model domain was 1,424 m deep by 9,800 m wide with the number of grid blocks assigned 89 and 205, respectively. For numerical simulations, the model was discretized in space with Δz=16 m grid blocks in which Δx fines from 200 m to 1 m in the vicinity of the Crystal Geyser and LGW fault (Fig. 7). This local mesh refinement allows use of a small, detailed model in the area of interest. Thus, it is possible to minutely resolve processes of CO_2-brine migration adjacent to fault and geyser. In addition, small grids with a 1 m width are beneficial for geyser simulations since they enable pressure to build up in a well by CO_2 accumulations, similarly at Crystal Geyser at which the borehole diameter is only 0.39 m.

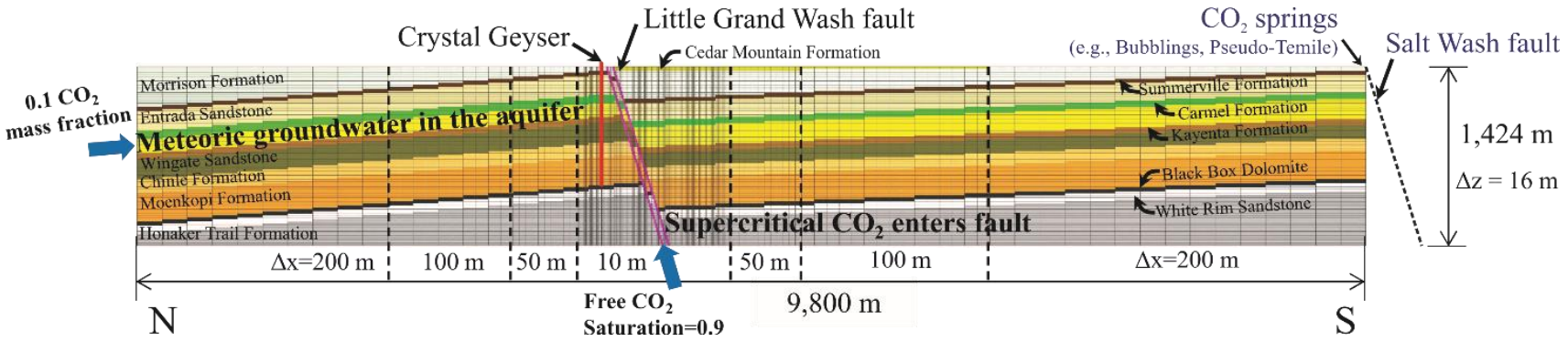

Figure 7. A 2-D north-south cross-sectional flow domain in the LGW fault zone was developed along a line AB on Fig. 1. CO_2-undersaturated brine (Navajo Sandstone) and supercritical CO_2 (the fault) were included as CO_2 sources. Presumable location of the SW fault and nearby CO_2-driven springs are shown at the right edge of the model but not actually included in simulations.

Table 1. Hydrogeologic parameters of each geologic formation in the study area[a].

	Formation	Abbr[b]	Porosity	k_h[c] (md)	k_v[c] (md)
CERT[c]	Cedar Mountain Formation	Ce	0.10	1	0.1
JURASSIC	Morrison Formation	M	0.20	1	0.1
	Summerville Formation	S	0.10	0.01	0.001
	Entrada Sandstone[d]	E	0.30	100	10
	Carmel Formation	Ca	0.20	0.01	0.001
	Navajo Sandstone[d]	N	0.20	528	52.8
	Kayenta Formation[d]	K	0.20	1	0.1
	Wingate Sandstone[d]	Wi	0.20	356	35.6
TRIASSIC	Chinle Formation	Ch	0.05	0.02	0.002
	Moenkopi Formation	Mo	0.05	0.02	0.002
PERMIAN	Black Box Dolomite	Bl	0.20	0.01	0.001
	White Rim Sandstone[d]	Wh	0.30	100	10
PENN[c]	Honaker Trail Formation	Ho	0.20	0.01	0.001

[a]Data were collated from Allis et al. [2001], Burnside [2010], Hansley [1995], Hood and Patterson [1984], and White et al. [2004]. When no data were available, hydrogeologic parameters were hypothetically assigned to individual formation, based on their potential as aquifers: (1) high (k_h=100 md), (2) intermediate (k_h=1 md), and (3) low (k_h=0.01 md).

[b]Abbreviation of geologic formation names used in Figs. 8, 9, and 10 for convenience.

[c]k_h, horizontal permeability; k_v, vertical permeability; CERT, Cretaceous; PENN, Pennsylvanian.

[d]5 major aquifers for the region with Curtis Formation incorporated into the Entrada Sandstone.

Each geologic formation was assumed homogeneous and anisotropic (Table 1). Porosity and permeability values in Table 1 were collated from the literature that investigated the study area and/or adjacent fields (Allis et al., 2001; Burnside, 2010; Hansley, 1995; Hood and Patterson, 1984; White et al., 2004). A constant heat flux of 0.053 J m^{-2} s^{-1} was applied at the bottom to match the terrestrial heat flow around the town of Green River (Heath et al., 2009; Nuccio and Condon, 1996). With an assumption of a hydrostatic groundwater condition, initial conditions for all simulations were obtained by running a brine-only system until the steady state conditions were reached. Brine concentration (mass fraction [X_{NaCl}]=0.011) was taken from our chemistry data on brine effluent from Crystal Geyser.

Consequent pressure and temperature profiles with depth ranged from 0.1 to 13.8 MPa and 25.0 to 62.5 °C, respectively. Capillary pressure and relative permeability parameters for CO_2 and brine were taken from the literature (Table 2) (Han et al., 2012; Pruess and García, 2002). Note that van Genuchten function (van Genuchten, 1980) can overestimate the amount of CO_2 gas entry into a caprock due to zero gas-entry pressure (Gherardi et al., 2007). For boundary conditions, constant atmospheric pressure and land temperature (P=0.1 MPa and T=25 °C) were imposed on the top while no fluid flow conditions were given at the bottom boundary (Table 2). As the model contains a part of regionally extensive aquifers, hydrostatic pressure and temperature were maintained at both lateral boundaries throughout simulations. Further model parameters and conditions are presented in Table 2.

Table 2. Initial physical parameters and conditions used for numerical simulations in this study.

Number of elements	x-direction: 205; y-direction: 1; z-direction: 89
Size of each element (m)	Δx = 200, 100, 50, 10, 1; Δy = 1; Δz = 16
Rock density (kg m^{-3})	2650
Rock heat capacity (kJ kg^{-1} $°C^{-1}$)	1000
Salinity	0.011 NaCl mass fraction
Boundary conditions	Top: constant pressure (0.1013 MPa) and temperature (25 °C)
	Lateral: constant hydrostatic pressure/temperature
	Bottom: no flow and constant heat flux (0.053 J s^{-1} m^{-2})

Relative Permeability		
Phase	Liquid[a]	Gas[b]
Functions	$k_{rl} = \sqrt{S^*}\left\{1-\left(1-\left[S^*\right]^{1/\lambda}\right)^{\lambda}\right\}^2$	$k_{rg} = \left(1-\bar{S}\right)^2\left(1-\bar{S}^2\right)$
	$S^* = \frac{S_l - S_{lr}}{1-S_{lr}}$	$\bar{S} = \frac{S_l - S_{lr}}{1-S_{lr}-S_{gr}}$
Parameters	$S_{lr} = 0.2$	$S_{gr} = 0.2$
	$\lambda = 0.457$	

Capillary Pressure[a]	
Functions	Parameters
$P_{cap} = -P_0\left(\left[S^*\right]^{-1/\lambda} - 1\right)^{1-\lambda}$	$S_{lr} = 0.0$
	$\lambda = 0.457$
$S^* = \frac{S_l - S_{lr}}{1-S_{lr}}$	P_0 = 19.61 kPa

[a]Relative permeability of liquid and capillary pressure equations were taken from van Genuchten [1980].

[b]Relative permeability equations of gas were taken from Corey [1954].

Based on CO_2 origins discussed in the previous Section 2.2, CO_2 was released from two sources: (1) as a supercritical phase ($SCCO_2$) at the bottom cell (approximately 1,400 m depth) of the fault and (2) as a dissolved phase at the leftmost cells (600-690 m depth) of the Navajo Sandstone (Fig. 7). High saturation of supercritical CO_2 (S_{CO2}=0.9) was invoked with an assumption that CO_2 is generated below the base of the model, migrates along the fault and enters to the bottom of fault in the model. CO_2-undersaturated brine (X_{CO2}=0.1) was released in the northernmost part of the Navajo Sandstone (Fig. 7), following the regional groundwater flow to southeast (Fig. 2) (Hood and Patterson, 1984).

4.1.2. Modeling Scenarios

The two parallel fault strands were set to be separated by 40 m apart at the surface (Burnside, 2010). They were also set to have a constant width of 20 m including damage zone (Kampman et al., 2014b) and a total vertical throw of 180 m with no geometrical complexity (Dockrill and Shipton, 2010). Due to a lack of data on regional-scale fault permeability, variable fault permeabilities (k_v=0.01-500 md) were tested corresponding to high-, intermediate-, and low-permeable fault. In addition, Bense and Person (2006) found that hydraulic anisotropy can vary by two to three orders of magnitude with increasing fault throw of ~200 m. Accordingly, various fault anisotropy ratios ($k_v/k_h=\gamma$) of 1, 10, 50, and 100 were also tested in the simulations. A base case model was chosen representing highly permeable faults (k_v=500 md and γ=50) in order to discuss co-migration of CO_2 and brine within fault zone through time. The models with different properties of the LGW fault were also evaluated by matching computed results with field

soil CO_2 flux measurements at the surface. Then, an approximate range of regional fault permeability was determined.

Finally, an isotropic well with a diameter of 1 m was inserted into the model (k_v=0.5 md and γ=50) in which the computed CO_2 fluxes properly coincide with the field measurements, demonstrating Crystal Geyser within the northern footwall of the LGW fault. The coupled eruption dynamics of CO_2-brine mixture were investigated and the associated results were compared with the in-well observations of Crystal Geyser (Fig. 3). For better implications for a wellbore leakage of CO_2, sensitivity analysis of geysering patterns was also conducted with respect to four different parameters: intrinsic permeabilities of a well (k_w) and the surrounding matrix adjoining to a well (k_a), well porosity (ϕ_w), and well radius (r_w). There have been constant efforts to define thermodynamic and hydrogeologic conditions and mechanisms which drive geothermal or CO_2-driven geysering processes by numerical simulations. For instance, Ingebritsen and Rojstaczer (1996) used the porous medium approach (Darcian flow), showing a large sensitivity in eruption behavior of geothermal geyser to intrinsic and relative permeabilities and pressure gradients in the matrix. However, the connate limitations of Darcian model which assumes laminar flow through a relatively small flow path (e.g., porous media or tiny cracks in the cement plugs) led to use of drift flux model (Pruess, 2008b) or pipe approach (Lu, 2004; Lu et al., 2006; Watson et al., 2014) for studying on open-hole geyser processes. In this study, pseudo-geysering patterns were observed similar to Ingebritsen and Rojstaczer (1996) throughout the simulations due to the limitations on accurate description of Crystal Geyser in a regional-scale model (e.g., Darcian flow assumption, heterogeneity, well dimension and configuration). However,

examination of CO_2-driven geyser at a regional-scale could still improve our grasp of geysering procedures as previous interpretation of Crystal Geyser (Gouveia and Friedmann, 2006; Han et al., 2013a; Kampman et al., 2014b; Watson et al., 2014) was grounded on site-specific measurements.

4.2. Simulation Results

4.2.1. Co-Leakage of CO_2 and Brine within the LGW Fault Zone

4.2.1.1. Free CO_2 Leakage

Spatial Variations of Free CO_2 Migration

The base case (case 1) model represents the LGW fault (k_v=500 md and γ=50) as a favorable CO_2 leakage pathway. Fig. 8a illustrates free-phase CO_2 migration after 100 yr of CO_2 release for case 1. $SCCO_2$ gradually leaks from the bottom source (1,416 m depth) at the north trace of the LGW fault while the hydrostatic pressure is maintained. Buoyancy-driven advection appears a dominant mechanism for vertical CO_2 mass flow (864 kg d^{-1}) within the LGW fault. A certain portion of free CO_2 within the fault prefers to ascend vertically due to the buoyancy rather than following the diagonal fault plane. However, the vertical movement of deep sourced $SCCO_2$ is hampered by the presence of several intervening aquitards (e.g., Chinle, Moenkopi, Black Box Dolomite). At 1 km depth, for instance, $SCCO_2$ with S_{CO2}=0.24 keeps rising diagonally along the dip of the north fault trace (Fig. 8b). By contrast, the remainder of $SCCO_2$ with S_{CO2}=0.46 accumulates within the White Rim Sandstone between two fault traces under the Black

Box Dolomite. The cumulated $SCCO_2$ within the White Rim aquifer then reaches the south trace of the LGW fault and begins to leak through it.

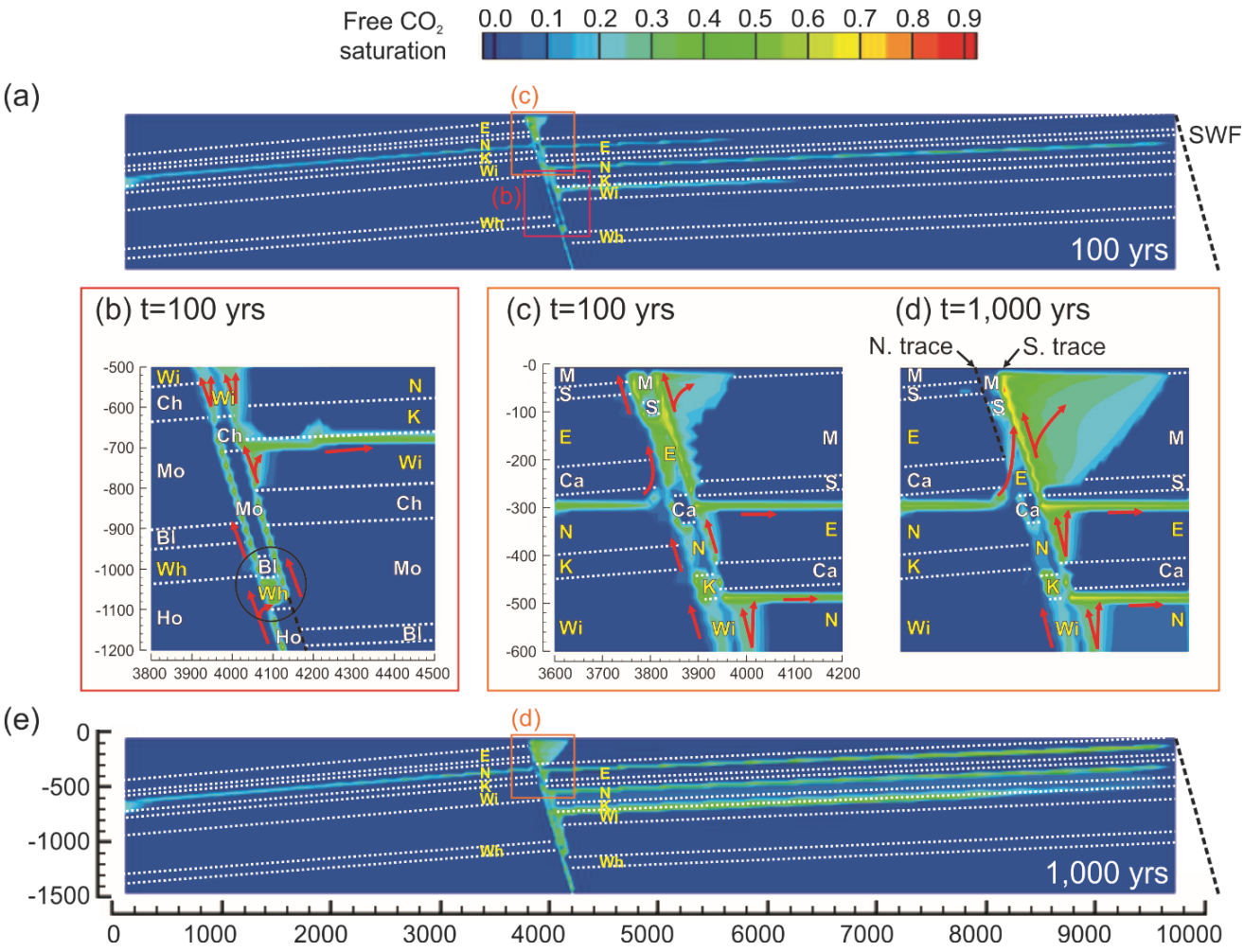

Figure 8. Computed free CO_2 leakage within the LGW fault zone through time for case 1 (high-k fault of k_v=500 md with γ=50) delineated by S_{CO2} at (a) t=100 yr and (e) t=1,000 yr. (b) A magnified model domain of a red box (700 m × 700 m) presented in (a). (c) A magnified model domain of an orange box (600 m × 600 m) presented in (a). (d) A magnified view of an orange box (600 m × 600 m) shown in (e). The presumable location of the SW fault is indicated by black dash lines with a mark of SWF at the right edge of the model. 5 major aquifers are denoted by yellow letters (refer to Table 1 for abbreviation). Intervening aquitards are represented by white letters for convenience (Table 1). Red arrows portray general movements of free CO_2. The scale for the size of a domain is given in meters.

Interestingly, free CO_2 rising vertically from the south fault trace flows into the aquifers that are located to the south of the LGW fault since the fault is south-dipping while the beddings are dipping north. (Figs. 8a and 8b). High k_v (500 md) of the LGW fault promotes CO_2 entry into to the southern aquifers (Entrada, Navajo, Wingate); for example, a CO_2 mass flow rate from the south fault trace to the bottom Wingate Sandstone was 533 kg d^{-1}. Subsequently, free CO_2 within the southern aquifers migrates further south and eventually reaches the SW fault about 6 km apart from the LGW fault (Fig. 8a).

Within the Navajo Sandstone, CO_2 was released as an aqueous phase (X_{CO2}=0.1) at the northernmost cells, considering a southward regional flow of CO_2-undersaturated brine from the San Rafael Swell to the LGW and SW fault zones (Baer and Rigby, 1978; Hood and Patterson, 1984; Kampman et al., 2014b; Wilkinson et al., 2009) (see Figs. 2 and 7). While CO_2-containing brines migrate up-dip on the limb of the Green River Anticline through the Navajo aquifer, only a small amount of CO_2 exsolves out and forms a thin layer of gaseous CO_2 plume (S_{CO2}=0.16) below the low-k Carmel Formation (Figs. 8a and 8c). During migration over a long distance of 4 km, gaseous CO_2 within the Navajo Sandstone is secured under the Carmel Formation with a very limited vertical mass flow rate (5.4 x 10^{-3} kg d^{-1}). This observation highlights the role of the Carmel Formation as an effective seal for CO_2 seepage unless there are flaws in it, which is also observed from the drilling cores in the field (Kampman et al., 2014b).

Once CO_2 gas enters the north trace of the LGW fault from the Navajo Sandstone, it goes through significantly enhanced vertical flow with a higher rate of four orders of magnitude (156 kg d^{-1}) (Figs. 8c and 8d). The strong tendency of CO_2 gas for upward

migration is most likely attributable to higher k_v of the LGW fault than that of the Navajo Sandstone and the absence of caprocks (Table 1). Besides, nearly doubled CO_2 saturation (0.30) due to high influx of both deeply-sourced CO_2 from the LGW fault and exsolved CO_2 from the Navajo Sandstone may enhance mobility of gaseous CO_2 by increasing relative permeability (Bachu and Bennion, 2008; Burton et al., 2009; Krevor et al., 2012). In consequence, most gaseous CO_2 from both deep and shallow sources escapes to the land surface, emphasizing a highly transmissive fault as an effective conduit (Figs. 8c and 8d). This is comparable to the previous field survey that all of the anomalous CO_2 fluxes (>10 g m^{-2} d^{-1}) were localized within ~20 m of the LGW fault traces (Fig. 4) (Jung et al., 2014).

Temporal Variations of Free CO_2 Migration

CO_2 inventory within the model progressively increases over time whereas a significant portion of CO_2 still escapes to the surface (Fig. 8e). As more free CO_2 is supplied from the sources, the saturation and relative permeability of CO_2 increase along the flow paths. Accordingly, more free CO_2 rises and gets into the southern aquifers at t=1,000 yr (Fig. 8e). For example, more CO_2 of the southern Wingate ascends and coalesces with CO_2 within the overlying Navajo and Kayenta Sandstones, forming a large CO_2 plume. In addition, the CO_2 plume along the fault slightly advances in a lateral direction through time.

The most notable changes in underground free CO_2 distribution between 100 and 1,000 yr appear near the land surface (Figs. 8c and 8d). At t=100 yr, both the north and

south traces of the LGW fault emit substantial amounts of gaseous CO_2 at high rates of 98.5 kg d^{-1} and 207 kg d^{-1}, respectively. However, at t=1,000 yr, CO_2 gas is no longer leaking through the north trace while still discharging from the south trace at a reduced mass flow rate of 163 kg d^{-1}. This shift in spatial CO_2 flux with time results from CO_2 plume migration to the south by the combined effects of south-dipping fault structure and the buoyant nature of CO_2. The CO_2 plume at the surface initially extended for about 170 m involving the north and south traces of the LGW fault (Fig. 8c). As more free CO_2 preferentially migrates vertically rather than following the fault, more CO_2 reaches the southern hanging wall of the LGW fault. Therefore, the left boundary of the CO_2 plume also moves 50 m more southward at the surface (Fig. 8d). Moreover, the extent of the CO_2 plume is almost twice as large (320 m) at t=1,000 yr but CO_2 release rate decreases in the southern part of the LGW fault.

4.2.1.2. Dissolved CO_2 Migration along with Brine

Most $SCCO_2$ released from the LGW fault at 1,416 m depth dissolves into ambient brine during upward migration along the fault (Fig. 9). As a consequence, CO_2 travels predominantly as an aqueous phase (X_{CO2}=~4.5%) rather than a supercritical or gaseous phase. Indeed, the dissolution of CO_2 into brine leads to a shrinking of CO_2 plume along flow paths and a consequent retardation of free CO_2 migration. For example, the CO_2 plume near the bottom source displays saturation of only ~0.5 despite the abundant supply of free CO_2 from depth (S_{CO2}=0.9) (Figs. 7, 8a and 8e). The field brine-meteoric groundwater dilution factors (the ratio of CO_2/Cl^- between sandstone formation fluids and Carboniferous brine) similarly suggested that ~75% of dissolved CO_2 in the

Navajo is obtained during upward migration of free CO_2 and brine from Permian aquifers, e.g., the White Rim (Kampman et al., 2014b). It should be noted that the dissolution of CO_2 may occur more intensely in the real field than in our model because we assumed homogeneous brines within each aquifer (X_{NaCl}=0.011) in which salinity substantially reduces the solubility of CO_2. On the other hand, in the field, meteoric groundwater mixing with brines in each aquifer may further accelerate the dissolution of free phase CO_2 into brines during migration (Kampman et al., 2014a and 2014b).

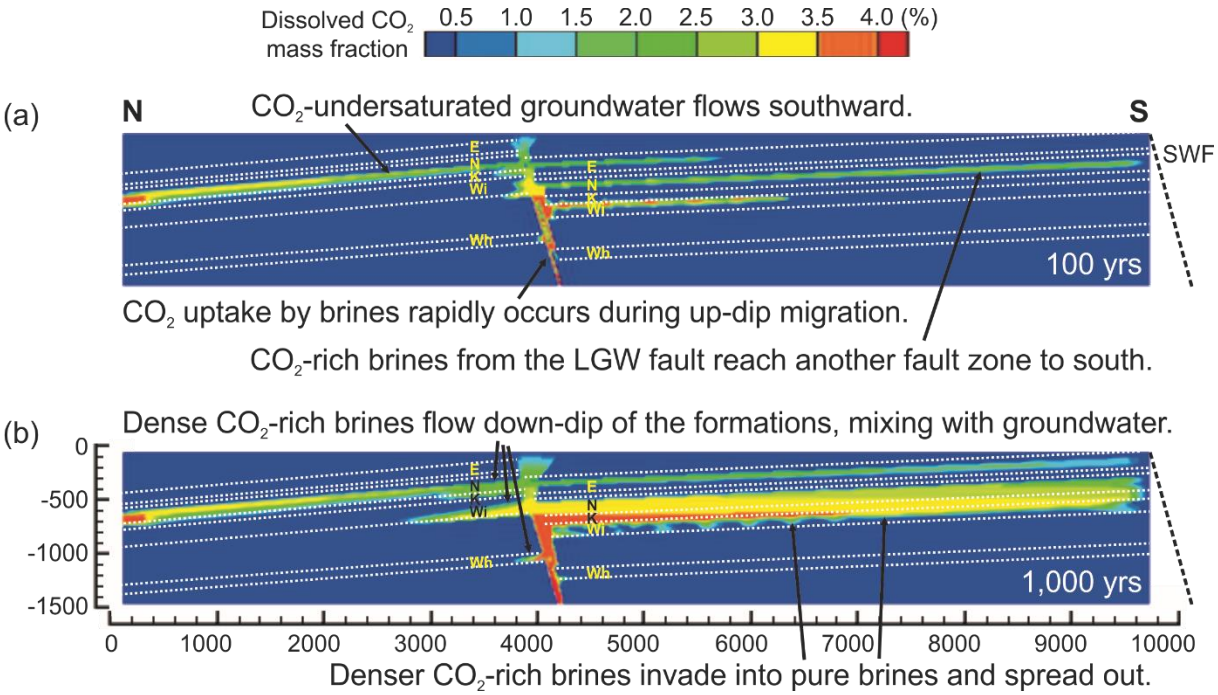

Figure 9. Computed dissolved CO_2 leakage within the LGW fault zone through time for case 1 (high-k fault of k_v=500 md with γ=50) delineated by mass fraction (%) at (a) t=100 yr and (b) t=1,000 yr after CO_2 releases into the system.

However, the density of CO_2-saturated brine is approximately 10 kg m^{-3} greater than brine with no CO_2 (García, 2001; Lindeberg and Bergmo, 2003), resulting in unique

feature of its transport. Unlike free CO_2, a significant fraction of CO_2-sauturated brine flows laterally into the northern aquifers (e.g., Navajo, Wingate, White Rim) from the fault during up-dip migration (Fig. 9b). Then, CO_2-rich brine migrates down-dip along the base of each aquifer due to its higher density than ambient pure brine. In fact, inflow of CO_2-saturated brine from the fault to the northern aquifers occurs slowly because its northward movement is impeded by southward flow of the regional groundwater; for instance, the velocities of CO_2-saturated brine flowing to the Navajo, Wingate, and White Rim were 22, 33, and 16 cm yr^{-1} respectively. Nevertheless, this CO_2-saturated brine also mixes with the less-dense regional groundwater, enhancing the dissolution of CO_2. This result elucidates why CO_2-saturated fluids were found at the base of the Navajo from the drilling core (Kampman et al., 2014b).

The aqueous CO_2 in brine also gives rise to an unstable state where denser CO_2-rich brine overlies less-dense pure brine, particularly within the southern aquifers (e.g., Entrada, Navajo, Wingate) (Fig. 9). This density instability could cause convective mixing of the fluid, which could greatly facilitate the transfer of free CO_2 into the dissolved phase depending on Rayleigh number and formation heterogeneity (Ennis-King and Paterson, 2003; Hassanzadeh et al., 2005; Kneafsey and Pruess, 2010). The presented regional-scale model is not able to capture the convective mixing due to the issues related to grid-scale. Nevertheless, based upon linear stability analysis (Ennis-King and Paterson, 2003), critical time (t_c) required for the convective instability to develop within each anisotropic aquifer can be estimated as

$$t_c \approx \frac{t_{mix} c_1(\gamma) \gamma \mu_w \phi^2 D}{k_h \Delta\rho g \alpha L} \qquad (1).$$

Here, t_{mix} is the time (s) for CO_2/water mixing to occur calculated from $t_{mix} \approx (\alpha L \mu_w)/(k_v \Delta\rho g)$, $c_1(\gamma)$ is the numerical constant function of the anisotropic ratio γ (=k_v/k_h), which can be determined from $c_1(\gamma)/c_1(1) = (1+\gamma^{1/2})^4/(16\gamma^2)$ where $c_1(1)$≈78, μ_w is the dynamic viscosity of the fluid (Pa·s), ϕ is the formation porosity, D is the effective diffusion coefficient of CO_2 (10^{-9} m^2 s^{-1}), $\Delta\rho$ is the density increase by dissolved CO_2 (kg m^{-3}), g is the gravitational acceleration (9.81 m s^{-2}), α is the CO_2 density ratio between the free and aqueous phases, and L is the thickness of the initial layer of free CO_2 (m). The linear stability analysis of our base model at t=100 yr reveals that the gravitational instability within each southern aquifer develops in only a few years: 5.8, 0.2, and 0.3 yr for the Entrada, Navajo, and Wingate, respectively. Subsequently, it is predicted in the field that small convective fingers might form, widen, and coalesce together over time, dissolving a large amount of CO_2. If there were no more CO_2 supply from the LGW fault, the CO_2 plume within the southern aquifers shown in Fig. 9a would completely dissolve into aquifer fluids in a couple of hundred years (t_{mix}): specifically, 445, 136, and 492 yr within the Entrada, Navajo, and Wingate, respectively. Eventually, a substantial portion of CO_2 derived from the deep Carboniferous reservoir is transported away from the LGW to SW fault zones as an aqueous phase, which was similarly indicated by Bickle and Kampman (2013).

4.2.2. A General Estimate of Regional Permeability of the Little Grand Wash Fault

As shown in the field observations, faulting is a key factor controlling the magnitude and location of CO_2 leakage (Jung et al., 2014). Therefore, fault zone

properties must be identified to understand fluid flow. However, the heterogeneous and complex nature of fault zones (e.g., geometry, fault population, and transient properties) makes it impossible to accurately predict fluid transmissibility properties along faults (Aydin, 2000; Foxford et al., 1998; Knipe et al., 1998). Nonetheless, numerical simulations in this study could draw a rough sketch of permeability of the LGW fault, which can be used as a good starting point for future studies.

For comparison with the base case model (case 1) representing a high permeability fault, case 2 was chosen with the same γ (=50) for delineating a low permeability fault (k_v=0.5 md). In both cases, $SCCO_2$ from depth undergoes phase transition to gas under subcritical conditions (the critical point of CO_2 at T=31.04 ℃ and P=7.38 MPa by Span and Wagner (1996)) at depths of 700-800 m. The phase transition is followed by drastic drops in free CO_2 density from ~530 to ~200 kg m^{-3} towards the land surface, increasing buoyancy and vertical movement of CO_2. In case 1, as previously addressed, high-k fault does not constrain rapid ascent of free CO_2. Consequently, CO_2 leaks only within the southern hanging wall of the LGW fault (Figs. 8d, 8e and 10a).

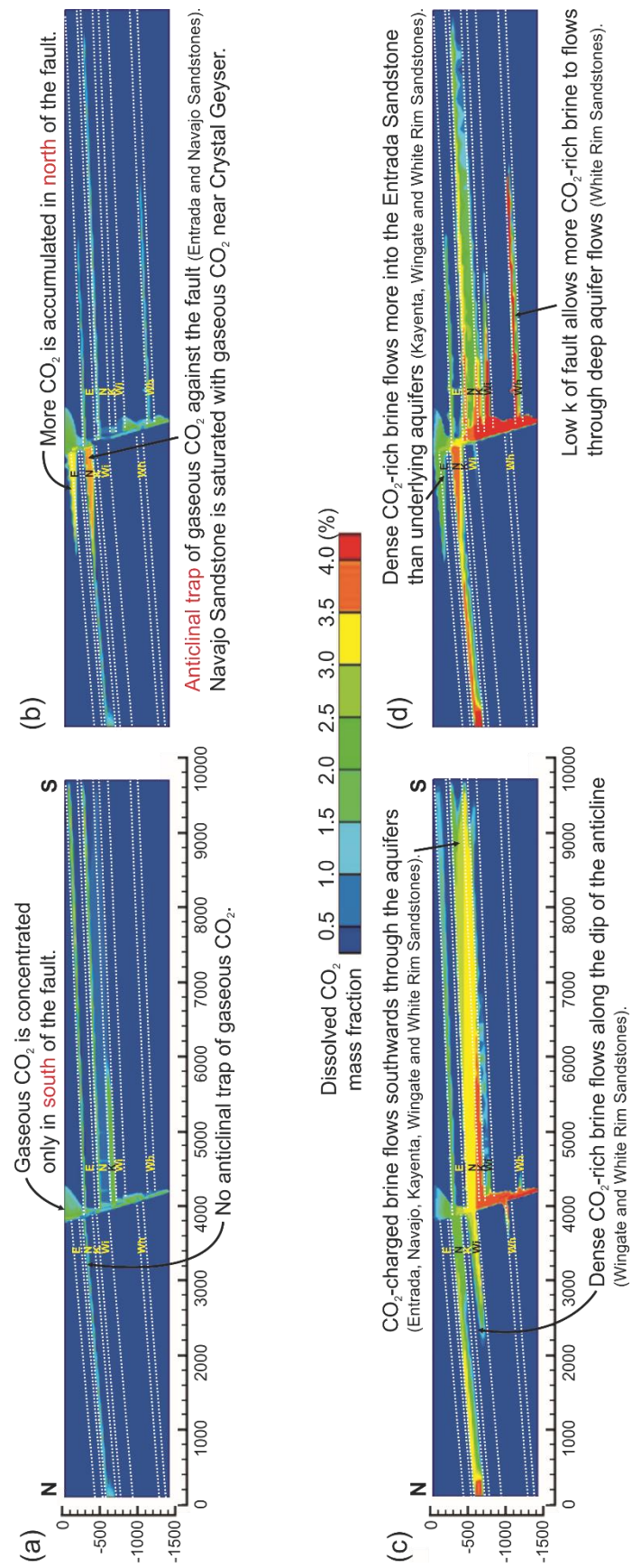

Figure 10. Computed CO_2 and brine migration within the LGW fault zone for (a), (c): case 1 (high-k fault of k_v=500 md with γ=50) and (b), (d): case 2 (low-k fault of k_v=0.5 md with γ=50) after steady-state reached. Gaseous and dissolved CO_2 are respectively represented by S_{CO2} and X_{CO2}.

By contrast, the low-k fault in case 2 significantly slows down the free CO_2 movement from depth although it also acts as a conduit similar to case 1. As a result, the steady-state conditions for case 2 were acquired approximately 20 ka later than case 1. Furthermore, a low-k fault causes more free CO_2 to flow horizontally into the relatively deep aquifer, the southern White Rim, as the residence time of CO_2 in the fault increases due to a very low flow rate (e.g., 3 kg d^{-1} across the bottom source cell) (Fig. 10b). The increased CO_2 residence time also leads to an enhanced diagonal migration of free CO_2 since its ascent is limited by the low-k fault so that free CO_2 moves uniformly in both x and z directions. Thus, more CO_2 gas reaches the top boundary following the LGW fault plane and the resultant leakage is localized more within the northern footwall than the southern hanging wall (Fig. 10b). This result from case 2 is compatible with the field survey in which 74% of anomalous CO_2 fluxes were found in the northern footwall of the LGW fault (Jung et al., 2014).

Indeed, the low-k fault in case 2 also behaves as an effective baffle to cross-fault flow of CO_2 from north to south. Accordingly, this induces the compartmentalization of pore pressures across the fault and the development of an anticlinal trap of CO_2 within the northern shallow aquifers (the Navajo and Entrada) (Fig. 10b), as implied by Heath et al. (2009) and Jung et al. (2014). The pore pressure and CO_2 saturation of these aquifers obviously demonstrates the discriminations between case 1 and 2, resulting from the presence of an anticlinal trap (Fig. 11a). Under this circumstance, the CO_2 solubility depends largely on the pressure and slightly on salinity (Duan and Sun, 2003); that is, the solubility of CO_2 in brine is greatly affected by whether an anticlinal trap exists or not (Fig. 11a). In case 1 (high-k fault), the Navajo and Entrada are under hydrostatic

conditions with almost no gaseous CO_2 except at the top of the Navajo. Therefore, the CO_2 solubility is predicted to decrease towards the surface, which is analogous to the theoretical CO_2 solubility curve calculated for hydrostatic pressures (see Figs. 12b and 21d in Kampman et al. (2014b)) based on the equations of (Duan and Sun, 2003). To the contrary, excess pressure of ~4 MPa and ~2 MPa builds up within the Navajo and Entrada in case 2 (low-k fault), respectively. Increased pressure also causes more CO_2 to dissolve, resulting in an almost vertical profile of the CO_2 solubility within each aquifer (Fig. 11a). The predicted CO_2 solubility is still smaller within the upper formation (Entrada) compared to the bottom formation (Navajo). Moreover, the CO_2 solubility curve is not continuous between them attributable to the effective sealing of the Carmel Formation. High CO_2 saturation of ~0.8 in case 2 indicates that large amounts of gaseous CO_2 exsolves out of CO_2-rich fluids ponding within the anticlinal trap.

Computed CO_2 fluxes from case 1 and 2 are now compared with the field results in order to validate the model and to assess regional permeability of the LGW fault. Figs. 11b (case 1) and 11c (case 2) depict the profiles of the field and simulated CO_2 fluxes at the surface across Crystal Geyser and the LGW fault against the distance from the north fault trace. The results obtained from the different anisotropy ratios of the fault (γ=1, 10, 50, 100) with a constant k_h are also plotted together for each case. The field survey results show that highest CO_2 fluxes (~613 g m^{-2} d^{-1}) appear along the fault traces, particularly close to the north fault zone. Distant from the fault traces, the CO_2 flux exponentially decreases to the background level (<10 g m^{-2} d^{-1}), suggesting that bioactivities in soil are the dominant sources of CO_2 in the surrounding area. Correspondingly, the simulated

fluxes showed zero values in these areas because CO_2 sourcing from bioactivity in the soil is not assigned in the model.

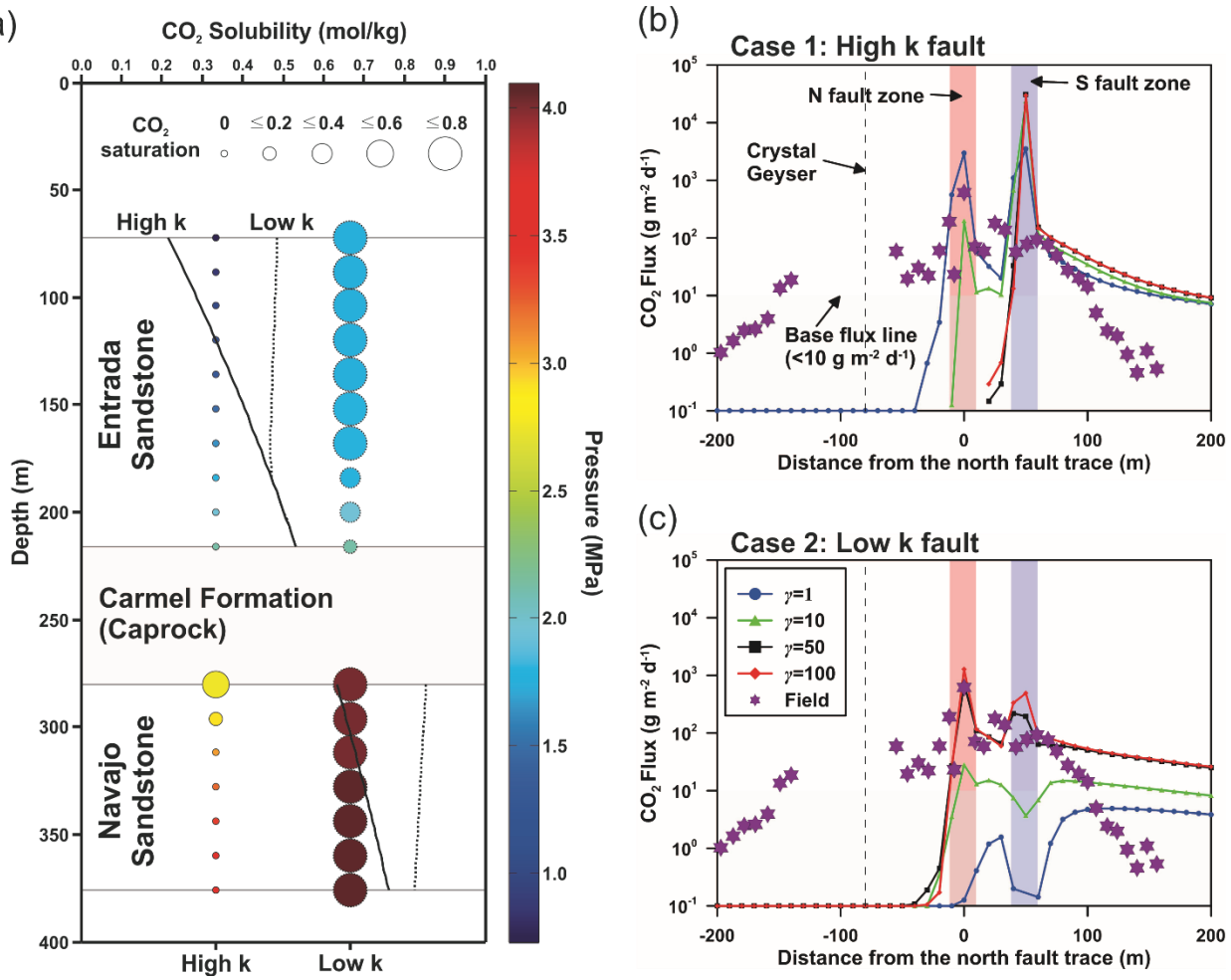

Figure 11. Differences in characteristics of CO_2 leakage between high- (case 1 of k_h=10 md) and low-k (case 2 of k_h=0.01 md) fault models. (a) Pressure (MPa), CO_2 saturation and solubility (mol kg^{-1}) in the shallow aquifer (Navajo and Entrada Sandstones) with depth when γ=50. Colors and sizes of the circles delineate pressure and CO_2 saturation; CO_2 solubility in brine is represented by a solid line for case 1 and a dotted line for case 2. Vertical profiles of field (star) and simulated CO_2 flux at the surface against the north trace of the LGW fault for (b) case 1 and (c) case 2. Negative values for distance are the distances to north from the north major fault trace while positive values to south. The north fault trace zone is highlighted in red, the south trace zone in blue, and background CO_2 flux (<10 g m^{-2} d^{-1}) in gray. The location of Crystal Geyser is represented by a dashed line.

High-k fault cases (case 1) always display the highest CO_2 flux at the south fault trace (blue box in Fig. 11b) unlike the observation in the field. In addition, the amounts of leaking CO_2 are much greater than the field; for example, the maximum simulated CO_2 flux of 31,000 g m^{-2} d^{-1} is recognized at the south fault trace for case 1 (γ=50). However, CO_2 fluxes at the north fault trace decrease to zero as more CO_2 escapes out from the southern hanging wall with increasing anisotropy ratio of the LGW fault. In contrast, the most anomalous CO_2 fluxes are observed at the north fault trace in low-k fault cases except the isotropic case (γ=1) in which the fault is extremely low-transmissive (k_v=0.01 md) (Fig. 11c). When γ=50 and 100, CO_2 fluxes appear up to 717 and 1,273 g m^{-2} d^{-1}, respectively, which agree well with the field survey. These cases also show high CO_2 fluxes at the south fault trace akin to the field observation (~178 g m^{-2} d^{-1}): ~220 and ~419 g m^{-2} d^{-1} each for γ=50 and 100. However, CO_2 leak is too suppressed when γ=10 with a very low k_v (=0.1 md) so that less anomalous CO_2 fluxes of ~28 g m^{-2} d^{-1} are recorded nearby the north trace while only background CO_2 fluxes are captured in other area. Consequentially, it can be surmised from entire simulations results that the LGW fault is likely low-permeable (Shipton et al., 2004) with 0.01 md $\leq k_h <$0.1 md and 0.5 md $\leq k_v <$ 1 md.

4.2.3. Computed Prediction of Dynamic Geysering Processes

4.2.3.1. Geyser Eruption Behavior of a Well

After placing a well (k_w=1×10^4 md) representing Crystal Geyser in the model (Fig. 7), CO_2 and brine rapidly emanate from the well at a rate of up to 1,447 kg d^{-1} until

$t=7.88\times10^3$ s, leading to corresponding sharp increases of XCO_2 (0.8 to 1%) and pressure (0.6 to 0.8 MPa) at the surface (Fig. 12b). XCO_2 and pressure then abruptly drop as water is emitted to the surface, which results in a relatively slow increase in S_{CO2} (0.3 to 0.4) (Fig. 12b). A high S_{CO2} (>0.2) with very limited XCO_2 (<0.4 %) indicates that CO_2 escapes predominantly as a gas phase at the surface (the 1st discharge regime in Fig. 12a). Yet S_{CO2} begins to diminish after reaching a peak at $t=3.47\times10^5$ s as CO_2 leak continues. Then, the well acts like a CO_2-spring, consistently emitting both CO_2-laden brine and CO_2 gas. As gaseous CO_2 is radically depleted with a limited recharge, the single-phase conditions are reached where only brine escapes the well quickly with no interference of gas flow at $t=6.31 \times 10^6$ s (73 d) (the onset of 2nd regime in Fig. 12a). Pressure also suddenly decreases in response to a large amount of the fluid discharge, but shortly thereafter recovers a hydrostatic state (0.26 MPa) by a rapid feed of pure brine under artesian conditions. No CO_2 gas is emitted from the well in the following incubation period of 8.01×10^6 s [93 d] (between $t=6.59\times10^6$ s [76 d] and 1.46×10^7 s [169 d]) since entire CO_2 recharged from the anticlinal trap of CO_2 in the shallow aquifers (Entrada and Navajo Sandstones) dissolves into brine, slowly increasing XCO_2 of ~0.35%.

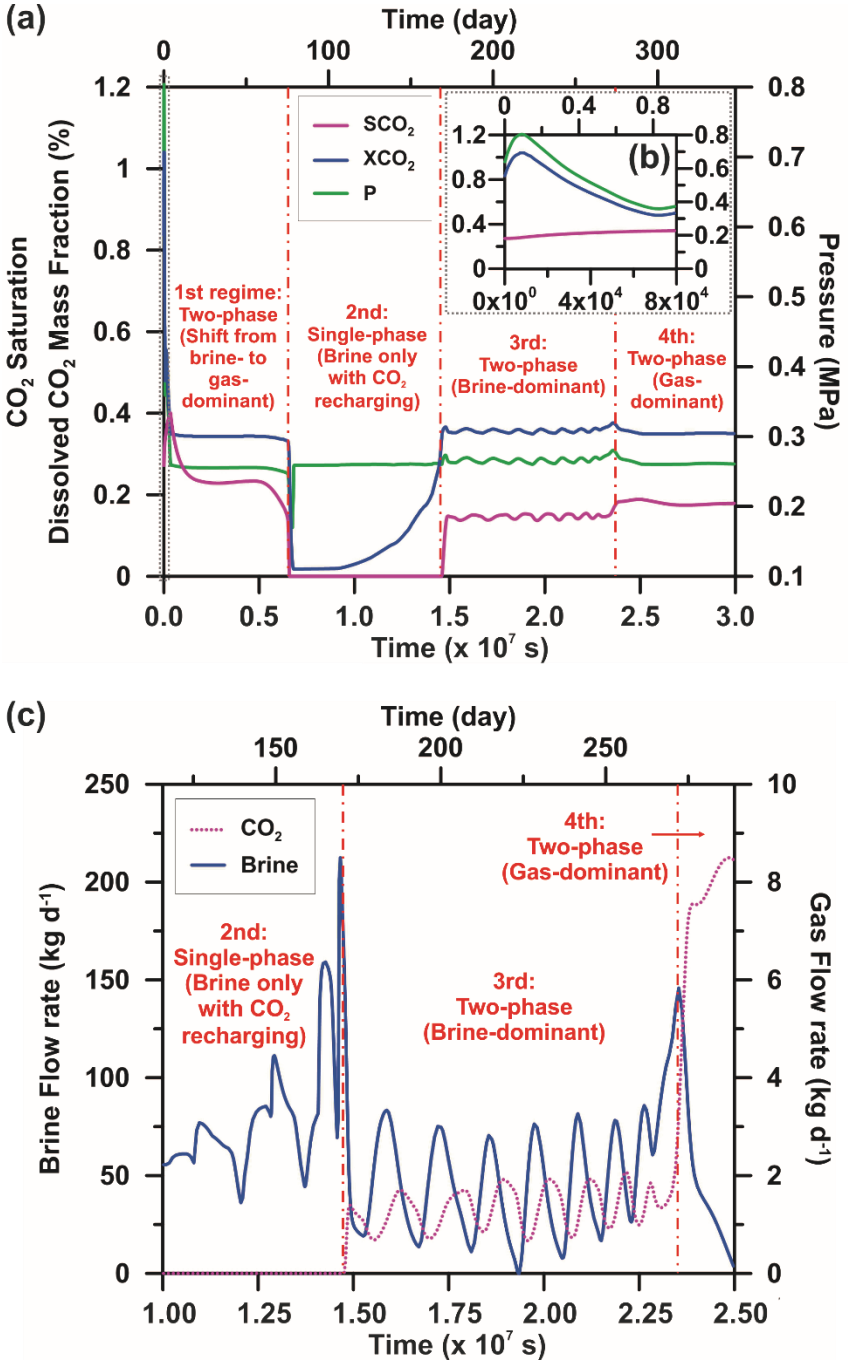

Figure 12. Simulated temporal variations of CO_2 discharge from the well (k_w=1 x 10^4 md) at the surface. (a) Changes in S_{CO2} (purple line), X_{CO2} (blue line), and pressure (green line) through time (~3 x 10^7 s [347 d]) at the surface with 4 discharge regimes denoted. (b) Magnified view of initial discharge from the well (~8 x 10^4 s [1 d]) shown in (a) by a dotted box. (c) Geyser-like periodic eruption represented by the flow rate of brine (blue solid line) and gaseous CO_2 (purple dotted line) in the 2nd-4th regime (1 x 10^7 s [116 d]-2.5 x 10^7 s [289 d]).

Attaining two-phase conditions again as CO_2 eventually exsolves, the well serves as a geyser, i.e. the discharge goes through geyser-like periodic cycling with a duration of ~1.40×10^6 s (16 d) (the 3rd regime in Figs. 12a and 12c). The onset of geysering is characterized by an acute peak of brine outflow rate of ~212 kg d^{-1} (Fig. 12c). Exsolution and coalescence of CO_2 gas within the well bolster the discharge, attributed to a large increase in buoyancy resulting from volumetric expansion with decreasing average density of the two-phase mixture (Pruess, 2008b). However, the favored ascent of CO_2 also rapidly consumes a stream of gas within the well, reducing and eventually eliminating the driving force for enhanced emanation. These self-enhancing and -limiting procedures repetitively alternate, yielding a series of cyclic eruptions of the well (from $t=1.46 \times 10^7$ s [169 d] to $t=2.35 \times 10^7$ s [272 d] in Fig. 12a). As more brine is replaced by CO_2 gas, i.e. S_{CO2} increases from 0.14 to 0.19 at $t=2.40 \times 10^7$ s (278 d), the flow rate of CO_2 also increases significantly to 8 kg d^{-1} whereas the brine flow rate is reduced even to zero (Figs. 12a-c). Subsequently, the well demonstrates no geyser-like eruptions but maintains only CO_2 gas emission akin to fumaroles (the 4th regime in Figs. 12a and 12c).

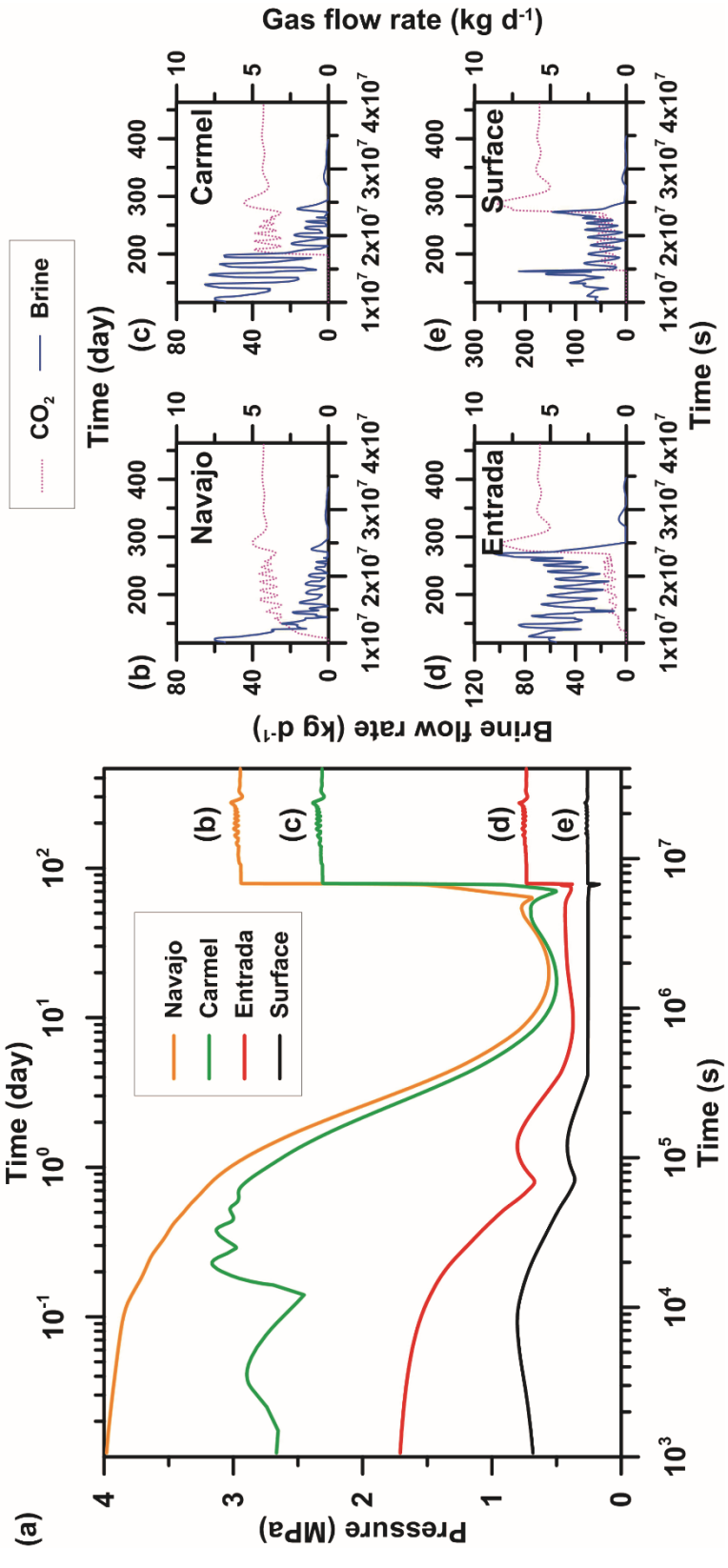

Figure 13. Simulated time-series data on CO_2 discharge from the well (k_w=1 x 10^4 md) with the depths corresponding to the top of each formation and the surface. (a) Pressure variation (MPa) with time at different depths. Periodic cycling patterns of the flow rates of brine (blue solid lines) and free CO_2 (pink dotted lines) are presented: (b) for the Navajo Sandstone, (c) for the Carmel Formation, (d) for the Entrada Sandstone depths, and (e) for the surface (t=1 x 10^7 s [116 d]-4.0 x 10^7 s [463 d]).

The almost same processes and cyclic variations are found at different depths within the well (Figs. 13a-e). The pressure and fluid flow rates given in Figs. 13a-e are chosen from the well at depths corresponding to the top of the each formation and surface. The Entrada and Navajo Sandstones were initially present under overpressures of ~1.1 MPa attributable to focused accumulations of CO_2 within the anticlinal trap (Figs. 10b and 11a), which well agrees with the field overpressure estimation of ~1.3 MPa (Kampman et al., 2014b). Under actual field conditions, fractures within the Carmel near Crystal Geyser would expedite pressure dissipation and thus the aquifers are less overpressured than our model (Hood and Patterson, 1984; Kampman et al., 2014b). After putting a well (Crystal Geyser) into the model, overpressures within the well are immediately removed by a runaway discharge of CO_2-brine mixtures; then, pressures at all depths are further reduced (up to 3.4 MPa at Navajo Sandstone depth) under hydrostatic states until restored by an inflow of pure brine from the ambient aquifers at t= 6.78×10^6 s (78 d) (Fig. 13a). Variations in pressure are more severe for the Navajo Sandstone because it hosts more CO_2 from an anticlinal trap with higher concentration of CO_2 than the Entrada (Fig. 10b).

Figs. 13b-e reflect upward migration of both brine and CO_2 in terms of the flow rate within the well after recharge. The Navajo and Entrada depths show earlier recharge of gaseous CO_2 than other depths because they gain CO_2 rapidly from adjacent CO_2-host reservoirs; that is, the well at both depths develops two-phase conditions faster so that the discharge of brine is substantially suppressed by a gas flow (Figs. 13b and 13d). Then, the upflow of CO_2 from host reservoirs dissolves into brine as denoted earlier. As a result, a gas stream of CO_2 appears later (~6.33×10^6 s [73 d]) at the Carmel and the

surface than the Navajo and Entrada (Figs. 13b-e). In particular, the flow rate of gaseous CO_2 sharply rises to ~8 kg d^{-1} at upper depths (Entrada and surface) when CO_2 gases from both aquifers combine together at t=2.35 x 10^7 s (271 d), which is accompanied by a rapid reduction in the brine flow rate due to the flow interference.

4.2.3.2. Sensitivity Analysis of Geysering Patterns

Different parameters imposed on the model provide several useful implications for predicting or estimating various CO_2 leakage patterns at a well, although the model in this study has a few innate limitations. The reference case for sensitivity analysis of geysering is presented by a green dotted line in Figs. 14a-d (k_w=1 x 10^5 md; k_a=1x10^{-4} md, ϕ_w=0.2, r_w=0.5 m). Varying permeability of a well does not significantly alter discharge pattern of a well at the surface (Fig. 14a). The flow rate increases proportionally with k_w; and therefore, the maximum discharge of gaseous CO_2 also occurs nearly 10 times earlier with increasing k_w by 10 times. Gaseous CO_2 recharges predominantly from the bottom as the well is almost insulated from the surroundings (k_a=1 x 10^{-4} md). Consequentially, the difference in time for gaseous CO_2 to reappear is only 28 d between the cases of k_w=1 x 10^4 (t=1.46 x 10^7 s [169 d]) and 1 x 10^5 md (t=1.22 x 10^7 s [141 d]) even though CO_2 was completely depleted 74 d earlier in the latter case (Fig. 14a). However, upward movement of CO_2 gas within a less-permeable well (k_w=1 x 10^4 md) requires more time and pressure build-up, resulting in more CO_2 pockets within the well before eruption. Thus, the quasi-cyclic eruption of CO_2 gas occurs more vigorously in the less-permeable well case (S_{CO2}=0.13-0.15) than more-permeable one (S_{CO2}=0.11-0.12).

CO_2 recharge rate to a well appears as a crucial factor to affect discharge behavior (Fig. 14b). When entirely isolated from the surroundings (k_a=1 x 10^{-6} md), the well gains CO_2 solely from the bottom but not laterally from the adjacent formations, i.e. the time interval between the complete depletion and re-discharge of CO_2 is more than threefold greater (>4 x 10^7 s [462 d]) than the reference case with a higher k_a of 1 x 10^{-4} md (1.2 x 10^7 s [139 d]). With increased connectivity (k_a=1 x 10^{-2} md) between the well and adjacent aquifers, more CO_2 hosted from the Navajo and Entrada Sandstones inflows into the well. In this case, CO_2 never depletes within the well in 2 yr and discharges continuously at the surface like a CO_2-spring rather than a geyser, maintaining S_{CO2} of ~0.23. However, k_a values assessed in this study are still small enough to limit water supply to the well, increasing CO_2 gas occupation and then developing more gas-dominant eruptions.

Compared with other parameters, differing well porosity (ϕ_w) does not considerably change eruption pattern of a well (Fig. 14c). Increased well ϕ_w possesses more room for the formation of CO_2 gas bubbles and allows sufficient supply of CO_2 to the well. In other words, CO_2 bubbles, which are necessary to expel the fluids and create oscillatory eruption (Lu et al., 2005), should fill more pores in the higher ϕ_w case. This gives rise to a delay in the onset of pseudo-cyclic eruptions, i.e. redevelopment of two-phase conditions of CO_2 gas and brine. For example, quasi-cycling eruption begins 6.13 x 10^6 s (71 d) earlier in the low ϕ_w case of 0.1 than the reference (ϕ =0.2) whereas 1.81 x 10^7 s (209 d) later in the high ϕ_w case of 0.5 (Fig. 14c). But the magnitude (S_{CO2}=0.11-0.12) and duration (4 x 10^6 s [46 d]) of eruption remain the same in all cases.

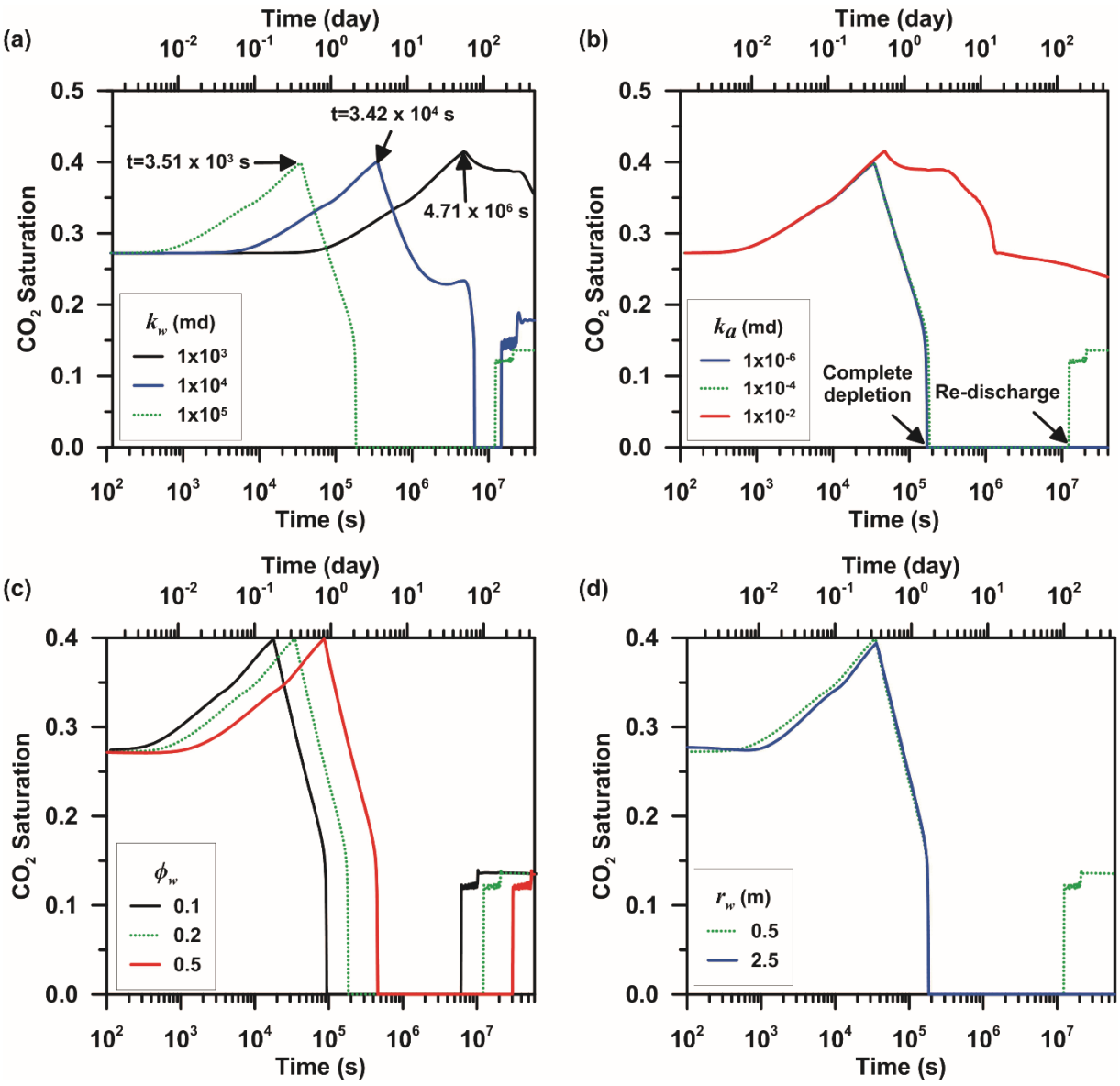

Figure 14. The responses of the well discharge behavior to various parameters at the surface: (a) well permeability (k_w), (b) permeability of the matrix adjoining to the well (k_a), (c) well porosity (ϕ_w), and (d) well radius (r_w). The reference case computed with the identical parameters (k_w=1 x 10^5 md; k_a=1x10^{-4} md, ϕ_w=0.2, r_w=0.5 m) is shown by green dotted lines in plot (a)-(d).

Lastly, well discharge behavior was tested with varying a well radius (r_w). Historically, the majority of studies suggest that geothermal-driven hot geysers should involve a long, narrow channel attached to a source in order for geysering to occur (Allen and Day, 1935; Lu et al., 2005; Nechayev, 2012; Sherzer, 1933; Steinberg et al., 1982). A

high ratio of channel length to diameter (30-110) has been also proposed, which assures a vigorous cyclic discharge by developing a slug fluid flow regime with the formation of Taylor bubbles (Lu, 2004). For CO_2-driven geysers, Watson et al. (2014) reported a greater eruption height from a well with a smaller cross-sectional area due to a limited lateral expansion of CO_2 bubbles and consequent increase in vertical acceleration. Similarly, no geysering behavior is observed from a well with r_w >0.5 m in our model since larger amounts of CO_2 are required to occupy the well before eruption (Fig. 14d): gas slugs (Taylor bubbles) would get more difficult to become large enough to possess the entire cross section of the well with a greater r_w.

5. Discussions

5.1. Factors that Control CO_2 Fluxes in the LGW Fault Zone

Spatial variations of CO_2 flux in the LGW fault zone were divided into 16 zones (the 1^{st} -16^{th} zone from left to right) with ~120 m distance in order to observe the east-west trend of CO_2 fluxes (Fig. 15a). A topographic profile was also developed along the north major trace of the LGW fault (Fig. 15b). The maximum (red star), mean (green circle) and median (blue rectangular) values of CO_2 fluxes in each zone are presented in Fig. 15c. Mean CO_2 fluxes generally decrease eastwards from 211 g m^{-2} d^{-1} (4^{th} zone) to 0.68 g m^{-2} d^{-1} (15^{th} zone) as being further eastward from Crystal Geyser. CO_2 gas leaks most actively through underground pathways in the vicinity of Crystal Geyser including the borehole. Figs. 15b and 15c show that anomalous mean CO_2 fluxes were seemingly related to the zones with relatively lower elevation (e.g., 28.74 g m^{-2} d^{-1} in the 3^{rd} zone

whose elevation below 1,240 masl). However, the zones with higher elevation (~1,280 masl) had the most anomalous CO_2 fluxes (e.g., mean CO_2 fluxes of 587.30 g m^{-2} d^{-1} in the 6th and 409.28 g m^{-2} d^{-1} in the 10th zones). Therefore, it could be inferred that the surface elevation is not directly correlated with CO_2 flux anomalies. In addition, Fig. 15b and 5c indicate no relationship between CO_2 flux anomalies and travertine ages even if travertines are the evidences of current/ancient pathways for CO_2-rich fluids in the subsurface. Rather, larger ancient travertines strongly coincide with CO_2 anomalies (Fig. 16). For instance, based on maximum values within 30 m of each travertine, high CO_2 fluxes of 5,917 g m^{-2} d^{-1} and 887 g m^{-2} d^{-1} were observed at L5 [69,660 m^3] and at L7 [10,213 m^3], respectively (see Fig. 4.14 and Table 4.7 in Burnside (2010) for the volumes of travertines in the study area; also see Table 3 for different notions of name for ancient travertines in Burnside (2010) and this study). This observation implies that more highly-transmissive conduits conveyed more CO_2-rich fluids to the surface and left larger volumes of ancient travertines, but that these conduits were not self-sealed completely by mineral precipitation. Hence, CO_2 gas still escapes through them even after several hundred thousand years (Burnside et al., 2013).

In contrast, at Crystal Geyser, the eruption height has been significantly reduced from 25-45 m in 1936 (Kelsey, 1991) to 1-5 m in 2013 (see Han et al. (2013b) for further references and information on changes in eruption patterns at Crystal Geyser). These historic observations indicate that the eruption intensity at Crystal Geyser has decreased since it was initially drilled in the 1930's. Even if continuous decrease in the eruption intensity results principally from mineral precipitation, the preferential pathways for CO_2 around the geyser are unlikely to be sealed completely by mineral deposits. Rather, if

mineral precipitation prevents CO_2 leakage, CO_2 gas would take other relatively high-permeability conduits in the crust and release at different locations (Burnside et al., 2013). The different positions of ancient travertines with varying ages along the LGW faults show evidence of switching in the CO_2 leakage pathways over time (Shipton et al., 2005).

Six north-south profiles (the 1^{st}~6^{th} profiles from left to right) of CO_2 fluxes were selected from the 7 zones and plotted against the distance from the north major fault trace (Fig. 15d). The highest CO_2 fluxes observed next to Crystal Geyser were excluded in the 2^{nd} profile. They distinctively show that more CO_2 flux anomalies are present in the northern footwall relative to the southern hanging wall. In addition, the areas where two traces of the LGW fault are closely spaced manifest much higher CO_2 anomalies. For example, the 2^{nd} and 5^{th} profiles in which distances between two major fault traces are below 30 m displayed up to 613 g m^{-2} d^{-1} and 5,515 g m^{-2} d^{-1} of maximum CO_2 flux anomalies, respectively (Fig. 15d). However, the other profiles where the distances between these two major fault traces are above 30 m gave relatively smaller CO_2 flux anomalies (<100 g m^{-2} d^{-1}). Hence, it can be inferred that more fracture and joint zones might have been developed by the concentrated accommodation of strains as two major fault traces developed closely in space. Subsequently, the net permeability in these zones became higher relative to the other zones in which the major fault traces were widely spaced. As a result, upward transport of gaseous CO_2 to the surface may be enhanced by the increased net permeability. The presence of more conduits in the zones of closely-spaced fault traces can be further supported by eruptive or consistent discharge of brine

through Crystal Geyser in the 3rd and washes in the 10th zones in Fig. 15a, which correspond to the 2nd and 5th profiles in Fig. 15d, respectively.

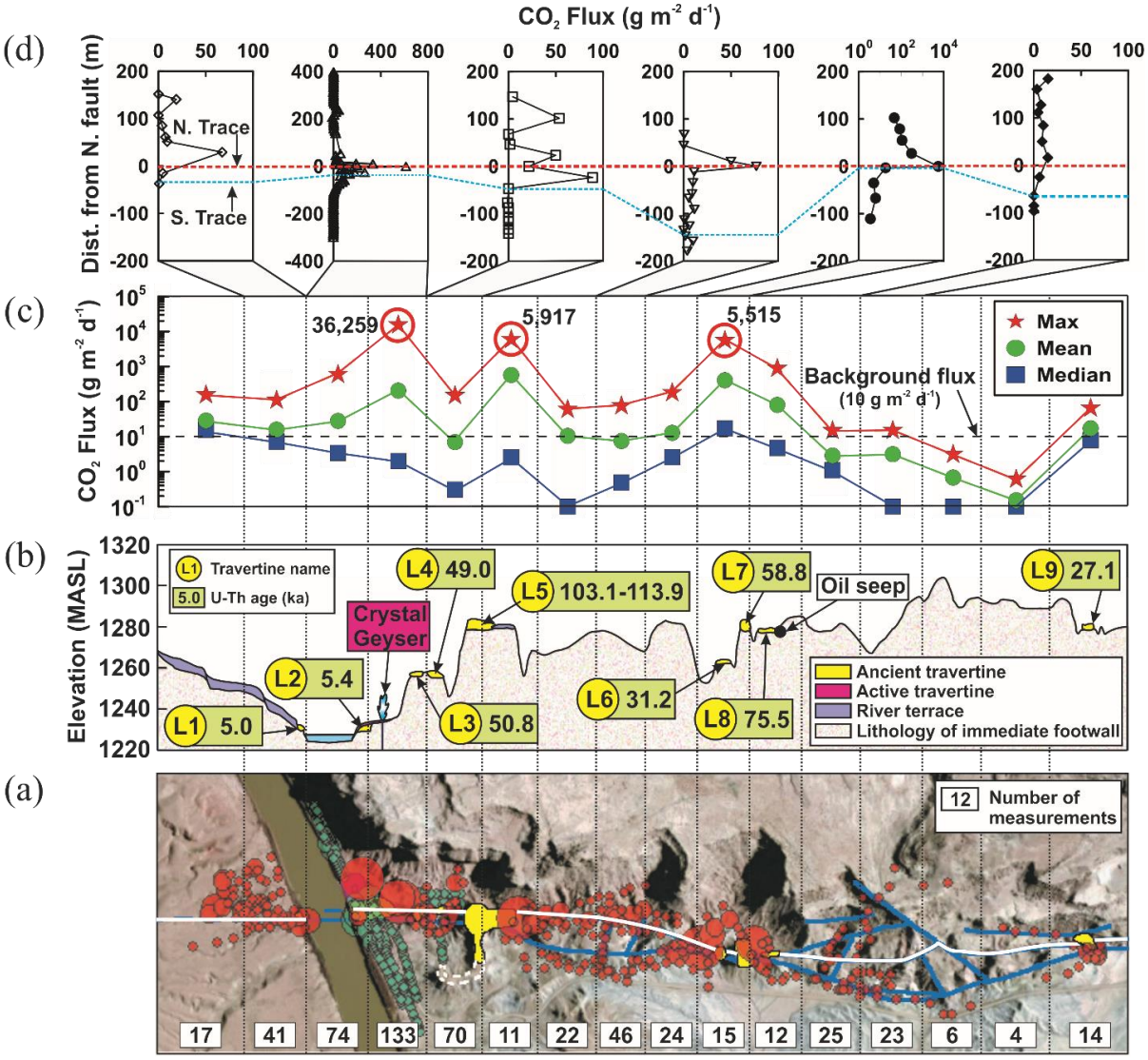

Figure 15. Analysis of soil gas CO_2 measurements in the LGW fault zone. (a) The CO_2 flux map with measurement population in each zone. (b) A topographic profile along the major north fault trace indicated by white line in (a) (modified from Burnside (2010); Burnside et al. (2013); Doelling (2002)). (c) Plots show calculated maximum/minimum and median values of CO_2 fluxes in each zone. Bold numbers with red circles indicate the three most anomalous CO_2 fluxes. Dashed line represents an upper limit of background flux (<10 g m^{-2} d^{-1}). (d) Vertical profiles of CO_2 fluxes in 7 "designated zones in (c) against the distance from the north major fault trace. Red and blue dotted lines delineate the north and south fault traces, respectively.

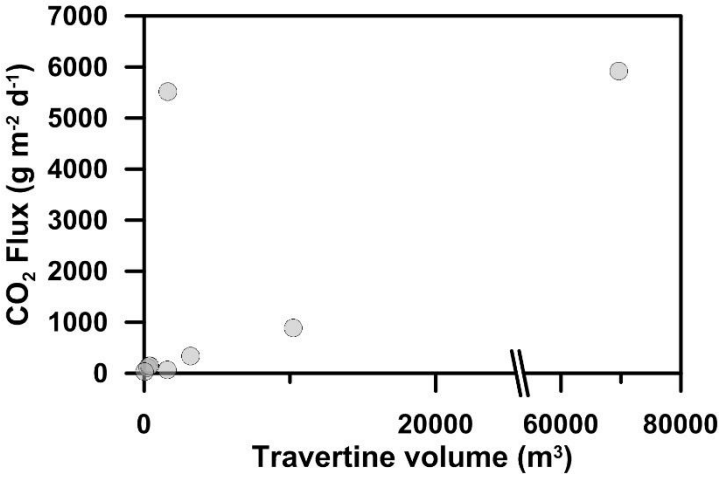

Figure 16. A cross plot of CO_2 flux with travertine volume within the LGW fault zone. CO_2 flux generally increases with travertine volume except the ancient L6 travertine. This implies that more CO_2-rich fluids discharge from highly-transmissive subsurface conduits, depositing larger travertine mounds.

Table 3. Notions of name for ancient travertines around the Little Grand Wash fault in this study compared with in Burnside (2010).

This study	Burnside (2010)
L1	L2.1
L2	L2.2
L3	L3.1
L4	L3.2
L5	L4
L6	L5
L7	L6
L8	L7
L9	L8

5.2. Soil CO_2 Diffusive vs. Advective Transport in the Faults

Soil CO_2 gas transport to the atmosphere can be either diffusive and/or advective (Lewicki et al., 2003). Assuming a constant rate of CO_2 production across the fault zones, a correlation between CO_2 concentration ($[CO_2]$) and flux could reveal zones of high/low diffusive/advective transport (Lewicki and Brantley, 2000). For example, zones of high diffusivity/permeability governed by advective transport should demonstrate a positive correlation between $[CO_2]$ and flux with consistently high $[CO_2]$ as those zones enhance both diffusion near the surface and advection at depths. In this section, three groups representing zones of diffusive or advective CO_2 flux were identified based on the correlation of mean $[CO_2]$ and flux.

Fig. 17 illustrates the relationship between mean $[CO_2]$ and flux measured in the LGW fault zone. Background CO_2 fluxes (<10 g m^{-2} d^{-1}) were observed from 85% of data measured at both the south major fault trace and fault splays, indicating no advective transport of CO_2 (Group 1 in Fig. 17a). Group 1 also showed consistently low $[CO_2]$ with an average of 432.5 ppm, ranging 388-477 ppm. Additionally, 55% of data observed at the north major fault trace also fell into Group 1 with consistently low CO_2 fluxes and $[CO_2]$ (397-457 ppm). A linear regression of Group 1 (slope=0.1864 and R^2=0.0004, Fig. 18a) showed no distinct relationship between $[CO_2]$ and flux, reflecting low diffusivity/permeability zones dominated by diffusive CO_2 transport with no advection.

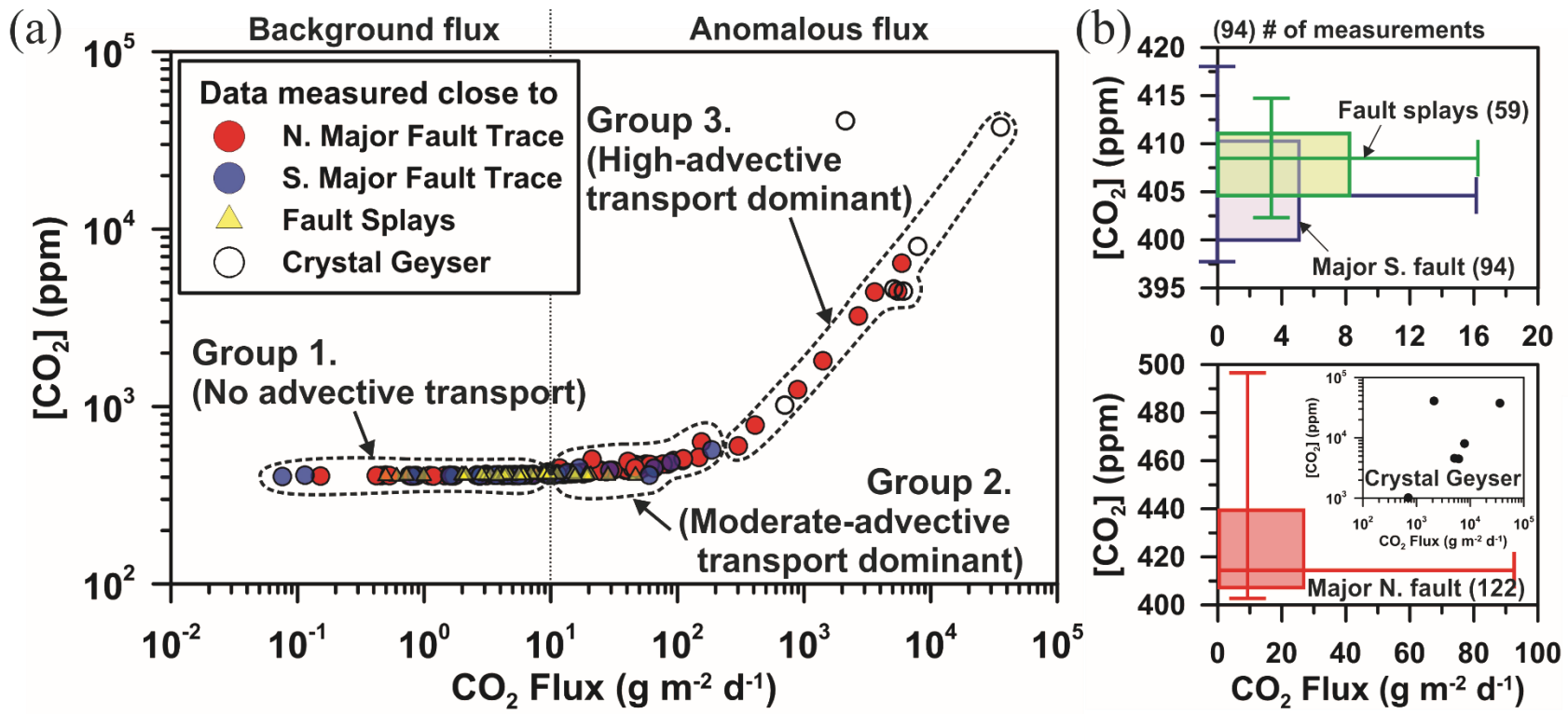

Figure 17. Analysis of $[CO_2]$ against CO_2 flux in the Little Grand Wash fault zone. (a) Plot of mean $[CO_2]$ versus CO_2 flux showing different correlations between them. (b) Box-whisker plots of $[CO_2]$ and flux measured in each fault type and at Crystal Geyser. The large box represents the 25^{th} and 75^{th} percentiles and whiskers represent the 10^{th}, 50^{th}, and 90^{th} percentiles.

The remaining 15% of the data at both the southern major fault trace and fault splays exhibited a positive correlation of CO_2 flux anomalies (11-186 g m^{-2} d^{-1}) with moderate [CO_2] (405-569 ppm) (Group 2 in Fig. 17a). Within the northern major fault trace zone, more CO_2 fluxes (38%; 11-155 g m^{-2} d^{-1}) are positively correlated with [CO_2] (413-632 ppm). This linear positive correlation of Group 2 between anomalous CO_2 flux and low [CO_2] (slope=0.9323 and R^2=0.7503, Fig. 18b) may represent low diffusivity but high permeability zones with moderately advective CO_2 transport; that is, the LGW fault zone selectively provides preferential pathways for CO_2 leakage and enhances advective transport of CO_2 at the same time.

The remainder (7%) of the data in the north major fault zone and all data measured at the pre-mud pots adjacent to Crystal Geyser showed much more anomalous CO_2 fluxes (301-36,259 g m^{-2} d^{-1}) and [CO_2] (600-37,513 ppm) (Group 3 in Fig. 17a). Group 3 displayed the strongest positive correlation between [CO_2] and flux, and fit well to a linear regression (slope=1.0388 and R^2=0.9939, Fig. 18c). These high [CO_2] and CO_2 fluxes therefore may imply the zones of high diffusivity/permeability with advective transport of CO_2 prevailing; furthermore, they suggest that the north major fault trace and associated fracture networks adjacent to Crystal Geyser serve as the most crucial pathways for CO_2 in the LGW fault zone.

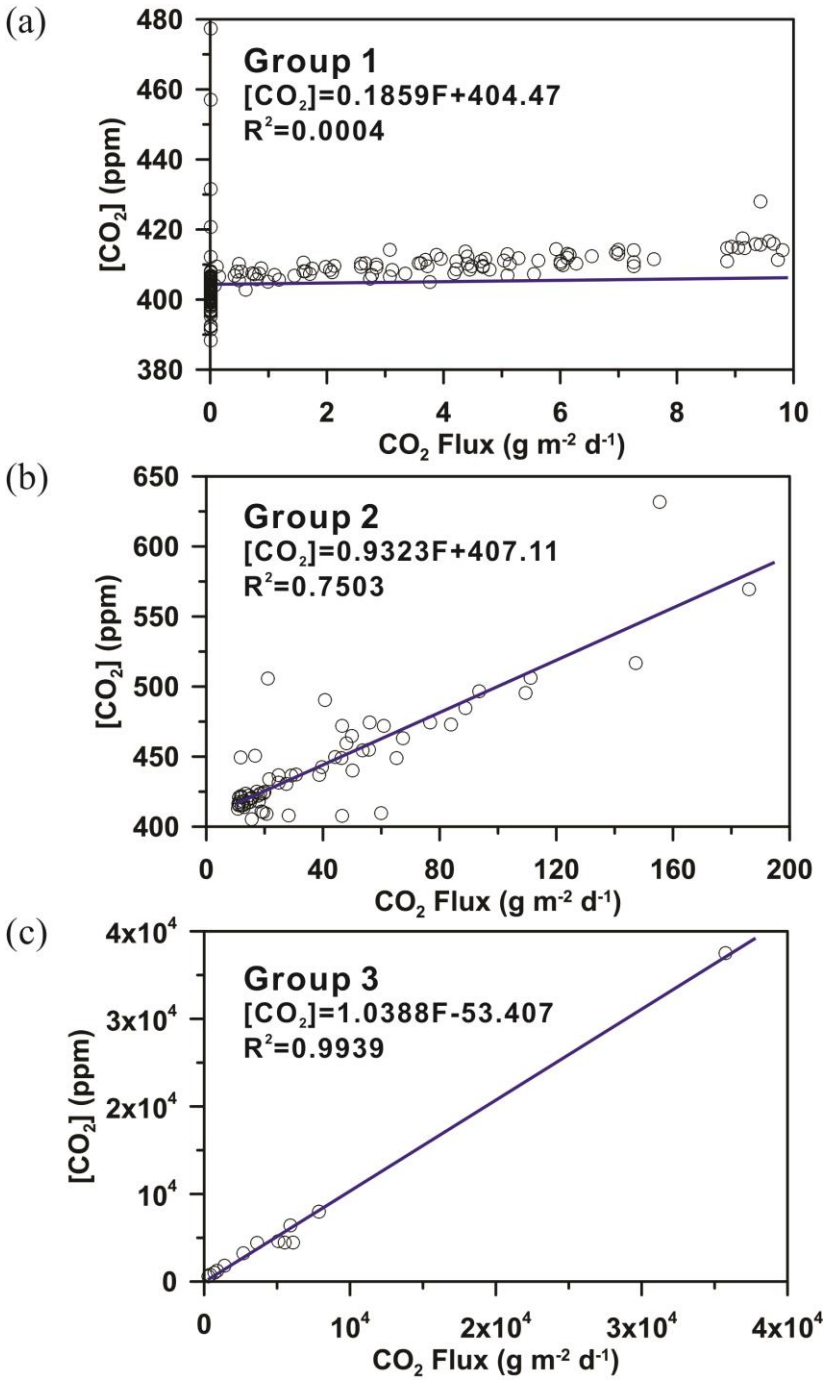

Figure 18. A linear regression of the correlation between $[CO_2]$ and flux with an equation and R^2, for (a) Group 1, (b) Group 2, and (c) Group 3 shown in Fig. 17a.

Percentile statistics of $[CO_2]$ and flux specifically describe differences in CO_2 emission from each type of the LGW fault (Fig. 17b). The 50th percentiles of $[CO_2]$ and

CO_2 flux (408.52 ppm and 3.35 g m^{-2} d^{-1}) in the fault splay zone are slightly higher than those in the south major fault trace zone (405 ppm and 0.01 g m^{-2} d^{-1}). The 75th percentiles of [CO_2] and CO_2 flux are also slightly higher in the fault splay zone (411.09 ppm and 8.23 g m^{-2} d^{-1}) relative to the south major fault zone (410.31 ppm and 5.08 g m^{-2} d^{-1}) but still manifests low [CO_2] and flux at a background level. Compared to the south major fault trace zone, the higher [CO_2] and flux seen in the fault splay zone may be attributed to the influence of the north major fault trace. This may be due to the fact that a majority of fault splays were found within the northern footwall adjacent to the north major fault trace. However, similar ranges of low [CO_2] and anomalous CO_2 flux are observed at the 90th percentiles for both the south major fault (418.05 ppm and 16.16 g m^{-2} d^{-1}) and fault splay zones (414.75 ppm and 16.25 g m^{-2} d^{-1}). This may be attributable to more substantial CO_2 degassing through smaller areas of the south major fault trace zone relative to the fault splay zone.

The north major fault trace zone gives much higher values of [CO_2] and flux at each percentile compared to other fault zones (Fig. 17b). The 50th percentile of CO_2 flux (9.24 g m^{-2} d^{-1}) is close to flux anomaly (>10 g m^{-2} d^{-1}) and the 75th percentile (26.81 g m^{-2} d^{-1}) exceeds more than two times the background level of CO_2 flux. Furthermore, the 90th percentile of CO_2 flux is much more anomalous (92.60 g m^{-2} d^{-1}), highlighting the potential of the north major fault trace as a conduit again. In contrast, [CO_2] appears to be very low even at the 90th percentile (496.55 ppm), which means most north fault trace have low diffusivity but high permeability intensifying advective transport of CO_2 as previously addressed.

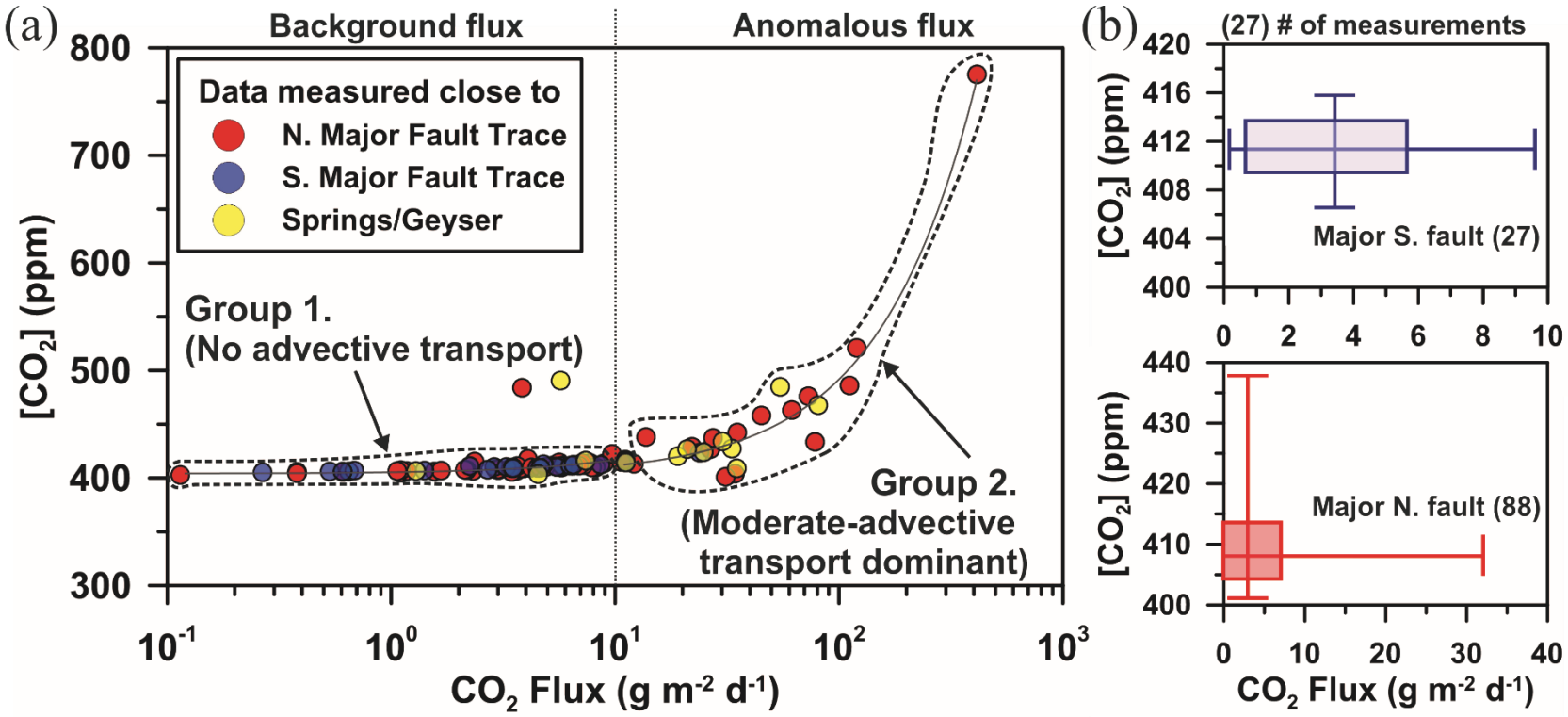

Figure 19. Analysis of $[CO_2]$ against CO_2 flux in the Salt Wash fault zone. (a) Plot of mean $[CO_2]$ versus CO_2 flux showing different correlations between them. Gray lines are the linear regressions for each group (group 1, slope=1.2958, R^2=0.3634; group 2, slope=0.8922, R^2=0.0.949). (b) Box-whisker plots of $[CO_2]$ and flux measured in northern and southern Salt Wash fault zones. The large box represents the 25th and 75th percentiles and whiskers represent the 10th, 50th, and 90th percentiles.

[CO_2] and fluxes measured in the SW fault zone showed similar results to the LGW fault; higher CO_2 flux anomalies (32.10 g m^{-2} d^{-1} at 90^{th} percentile) were observed in the north fault trace zone, particularly around the CO_2-driven springs, compared with the south fault trace zone (9.61 g m^{-2} d^{-1} at the 90^{th} percentile). However, both [CO_2] and flux anomalies were distinctively lower than those measured in the LGW fault, indicating less significant leakage of CO_2 in the SW fault zone. See Figs. 18 and 19 and Table 4-7 for further information on [CO_2] and flux recorded with respect to types of the faults and springs/geysers in the LGW and SW fault zones.

Table 4. Percentiles of [CO_2] and flux with respect to types of fault traces in the Little Grand Wash fault zone.

	North Major Fault		South Major Fault		Fault Splays	
	[CO_2] (ppm)	Flux (g m^{-2} d^{-1})	[CO_2] (ppm)	Flux (g m^{-2} d^{-1})	[CO_2] (ppm)	Flux (g m^{-2} d^{-1})
10%	402.76	0.01	397.76	0.01	402.34	0.01
25%	407.24	0.47	400.00	0.01	404.61	0.01
50%	414.33	9.24	404.65	0.01	408.52	3.35
75%	439.42	26.81	410.31	5.08	411.09	8.23
90%	496.55	92.60	418.05	16.16	414.75	16.25

Table 5. Mean [CO_2] and fluxes measured adjacent to Crystal Geyser[a].

[CO_2] (ppm)	Flux (g m^{-2} d^{-1})
7,991.31	7,882.51
40,680.1	2,125.58
4,465.51	6,100.10
4,591.59	5,092.07
37,513.30	35,757.50
1,019.98	704.29

[a]Data were measured within ~5 m of the Crystal Geyser.

Table 6. Percentiles of [CO_2] and flux with respect to types of fault traces in the Salt Wash fault zone.

	Salt Wash Fault Zone			
	North Major Fault (88)[a]		South Major Fault (27)[a]	
	[CO_2] (ppm)	Flux (g m^{-2} d^{-1})	[CO_2] (ppm)	Flux (g m^{-2} d^{-1})
10%	401.01	0.01	415.81	0.16
25%	404.15	0.01	406.58	0.67
50%	407.98	3.00	409.43	3.42
75%	413.52	7.14	411.39	5.65
90%	437.65	32.10	413.71	9.61

[a]The number indicates the measurement population.

Table 7. Mean [CO_2] and fluxes measured adjacent to CO_2-driven springs and geysers in the Salt Wash fault zone.

[CO_2] (ppm)	Flux (g m^{-2} d^{-1})	Adjacent Springs/geysers
408.86	34.87	Big Bubbling
467.65	80.63	Big Bubbling
427.24	33.16	Big Bubbling
406.48	1.29	Big Bubbling
484.58	54.68	Small Bubbling
419.98	19.01	Small Bubbling
434.09	30.15	Small Bubbling
426.90	20.99	Tenmile Geyser
403.57	4.52	Tenmile Geyser
424.12	24.83	Pseudo-Tenmile
416.02	7.38	Pseudo-Tenmile
414.25	11.18	Pseudo-Tenmile
490.61	5.70	Torrey’s Spring
416.59	0.00	Torrey’s Spring

5.3. Conceptual Model Demonstrating Potential CO_2 Sources and Leakage Pathways in Fault Zones

Based on the CO_2 flux observation and simulations, a conceptual model of a dynamic CO_2 leakage system within the LGW and SW fault zones was developed (Fig. 20). In order to determine CO_2 sources for the region, a number of studies previously analyzed chemical and isotopic compositions of gaseous CO_2 and fluids at CO_2-springs/geysers, travertine mounds, and carbonate veins (Assayag et al., 2009; Baer and Rigby, 1978; Heath et al., 2009; Kampman et al., 2009; Kampman et al., 2012; Mayo et al., 1991; Shipton et al., 2004; Wilkinson et al., 2008). In addition, Kampman et al. (2014a and 2014b) drilled a hole to a depth of 322 m, ~258 m west of Crystal Geyser, and presented downhole profiles of fluids chemistry. Their results demonstrate that free CO_2 exsolves within the fault and shallow aquifers above the bottom of the Navajo Sandstone. The local aquifers (e.g., the Entrada, Navajo, Kayenta, Wingate, and White Rim Sandstones) are very likely to be fed by (1) the influx of free CO_2 and CO_2-charged brine through the fault from the deep reservoirs (> 2 km depth), and (2) CO_2-undersaturated meteoric groundwater that recharges from the San Rafael Swell and flows laterally southeastward within the aquifers (Hood and Patterson, 1984). Combining these potential sources with the results of soil CO_2 flux survey could elucidate the subsurface CO_2 leakage processes and associated role of the faults on a regional scale.

The LGW fault is likely to be sealed to horizontal, cross-fault flow where low-permeable host rocks (e.g., Mancos Shale) are juxtaposed in the hanging wall. However, the fault is likely to be open to upwards-directed, along-fault flow via fractures in the fault damage zone (Dockrill and Shipton, 2010). Therefore, the LGW fault is thought to

impede a lateral flow of CO_2-rich brine in the aquifers (Fig. 20). Subsequently, gaseous CO_2 may be trapped in a north-plunging anticline against the south-dipping LGW fault (Kampman et al., 2014b). As more CO_2-charged brine is hampered by the fault, CO_2 gas exsolves and pools more and more within the anticlinal trap. High CO_2 flux anomalies concentrated in the northern footwall of the LGW fault support this preferential development of the anticlinal CO_2 trap within the northern aquifers. Furthermore, CO_2 gas from this anticlinal trap may be one of the factors that lead to the most intense eruption at Crystal Geyser than other geysers/springs throughout the LGW and SW fault zones.

The localized high CO_2 fluxes in the north part of the LGW fault could also result from the interplay of low permeability of the LGW fault and buoyant nature of CO_2. Field measurements of [CO_2] and flux indicated that low permeability/diffusivity zones are dominant in the LGW fault area (Fig. 17). Low permeability/diffusivity may be attributed to a clay-rich gouge or fault-related fractures, which were closed by mineral precipitation. Supercritical and gaseous CO_2 tend to ascend buoyantly in the subsurface due to its relatively lower density and viscosity than the surrounding brines (Han et al., 2012). However, in the LGW fault zone, upflow of deep-sourced CO_2 may be somewhat inhibited by low-transmissive faults or strata (e.g., the Summerville, Carmel, Chinle, and Moenkopi Formations). Hence free CO_2 would migrate not only upward but also laterally along the faults (Fig. 20). Open fractures aligned parallel to the faults in the damage zone may further allow this diagonal movement of CO_2 along the faults (Dockrill and Shipton, 2010; Shipton et al., 2004).

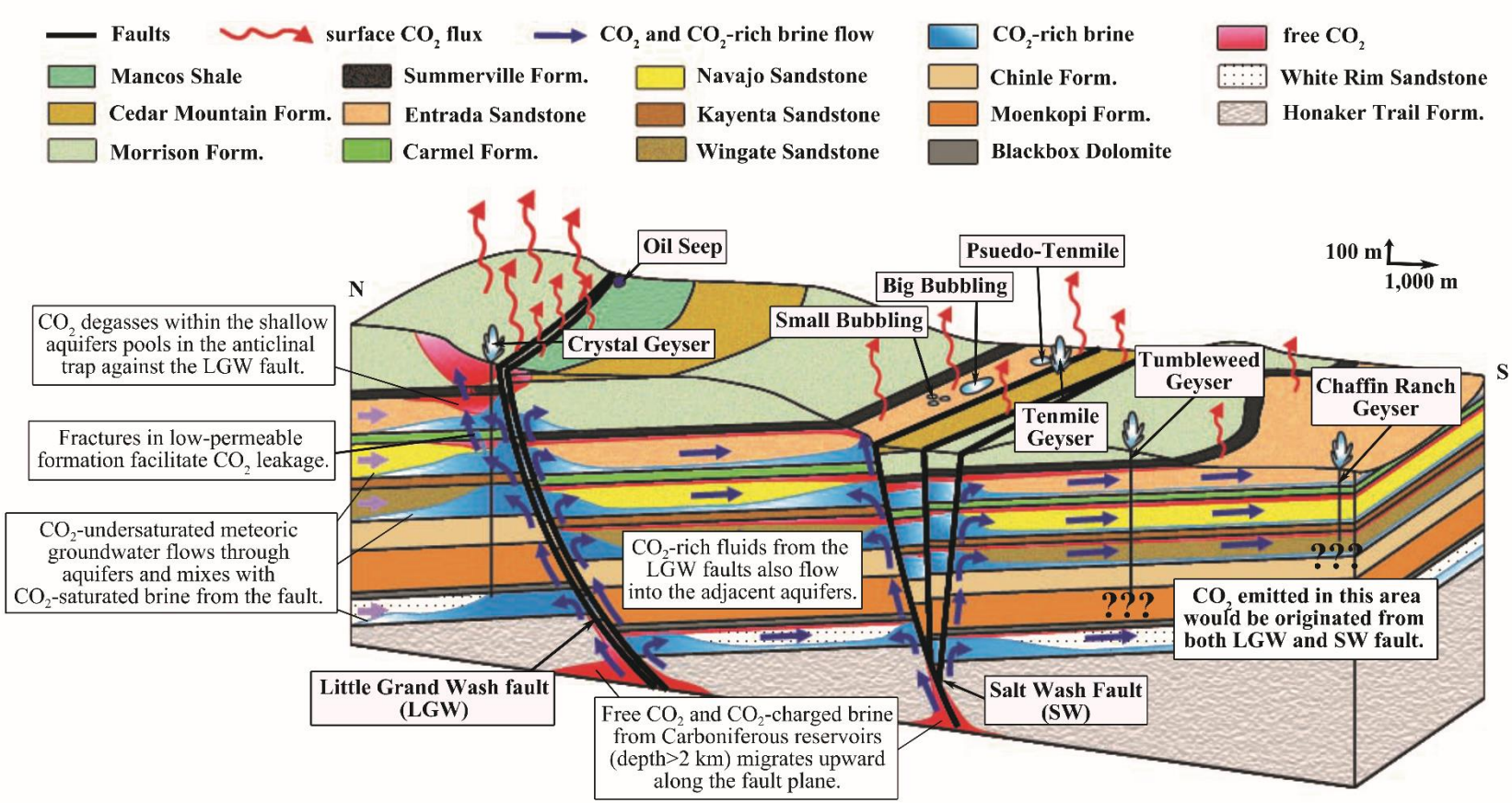

Figure 20. A conceptual diagram of potential CO_2 sources and likely CO_2 leakage pathways in the LGW and SW fault zones. Hypothetical free CO_2 and CO_2-saturated brine are highlighted in red and blue color, respectively. Note that meteoric groundwater migrates south through aquifers (Entrada, Navajo, Kayenta, Wingate, and White Rim Sandstones) even though it is not illustrated in the figure. Light purple arrows represent meteoric groundwater recharge from rainfall in the San Rafael Swell (Hood and Patterson, 1984), northwest of the study area.

Following the direction of regional groundwater flow in the major aquifers, some portion of upflow CO_2 from the deep crust in the LGW fault zone could be transported towards the SW fault zone (Fig. 20). In addition, CO_2-charged brine within the northern aquifers could also flow into the juxtaposed formations across the LGW fault. Moreover, even if the LGW fault completely seals cross-fault flow, a portion of CO_2-laden brine could skirt around the edge of the fault. This CO_2 from both deep and shallow depths is expected to migrate in dissolved and gas phases through the aquifers to the SW faults. Wilkinson et al. (2008) found that the solubility of CO_2 in brine dramatically decreases towards the surface at a depth above 650 m, considering an ambient geothermal gradient of 21.2 ℃/km (Heath et al., 2009). Since the depth of each aquifer decreases towards the SW fault due to the north-plunging anticline, more CO_2 gas exsolves out of the fluids during southward migration of CO_2-charged brine. Thus, the secondary anticline CO_2 trap may be developed against the SW fault. Furthermore, additional inputs of deep-sourced CO_2 and CO_2-rich brine to the northern SW fault has been inferred from a slight decrease in pH of the water effluent and increases in Cl^- concentration along the flow paths from Crystal Geyser to Small Bubbling Spring (Kampman et al., 2009). Kampman et al. (2012) also revealed historical inputs of both CO_2 and brine along the SW fault by examining trace-element and stable isotopic composition of carbonate deposits. Consequently, CO_2 leaks more in the northern footwall of the SW fault by the same mechanism as in the LGW fault zone. This idea could be corroborated by the fact that soil CO_2 flux anomalies and springs are more abundant in the north area than the south area of the SW fault (Figs. 5 and 19).

Despite new and potential inputs of CO_2 from the deep crust and from the LGW fault, the SW fault zone exhibited relatively few anomalous CO_2 fluxes compared with the LGW fault zone. This discrepancy between CO_2 fluxes along each fault are most likely the result of differences in fault zone architecture and related permeability structure (Caine et al., 1996). For example, the fault may give the most favorable conduit for CO_2 leakage within the LGW fault zone because the local aquifers are overlain by low-permeable formations. Burnside et al. (2013) suggested "fault-focused leakage" for CO_2 degassing in the LGW fault zone based on the observation that the travertine mounds are limited to areas of high fracture density along the LGW fault (Dockrill and Shipton, 2010). Thus, our observation of CO_2 flux anomalies predominantly appeared along the LGW fault. In contrast, the Entrada Sandstone is exposed at the surface in the SW fault zone, which allows "unconfined aquifer leakage" of CO_2 (Burnside et al., 2013). This outcropped Entrada Sandstone may disperse CO_2 away from the SW fault and attenuate CO_2 flux, leaving highly distributed and smaller travertine deposits in the SW fault zone. Furthermore, our data on the relationship between [CO_2] and flux suggest that the LGW fault zone has more areas (30%) of high permeability than the SW fault zone (22%), which facilitate CO_2 transport and result in high CO_2 fluxes (Figs. 17 and 19).

The decline in CO_2 flux from north to south can be partly attributed to a decrease in CO_2 concentration as CO_2 escapes to the surface during transport of CO_2-rich fluids from the LGW to the SW fault zone. Subsequently, CO_2 and CO_2-laden brine would cross or skirt around the SW fault through the local aquifers and finally encounter Tumbleweed and Chaffin Ranch Geysers (Fig. 20). Then, CO_2 degasses through the boreholes and results in periodic eruptions at those geysers even though they are distant

from the faults. A systematic and progressive evolution of water chemistry (e.g., an increase in $(Na^{+}+K^{+})/(Ca^{2+}+Mg^{2+})$ by silicate dissolution and precipitation of carbonate and clay minerals) from north to south supports the same sources of CO_2-charged brine that discharges at all springs/geysers around the LGW and SW fault zones (Kampman et al., 2009). In addition, Wilkinson et al. (2008) showed little variations of $CO_2/^{3}He$ (0.291×10^{11}-4.47×10^{11}, except Tenmile Geyser) and $^{3}He/^{4}He$ (0.224-0.265 R_a, except Pseudo-Tenmile) ratios in gas samples, which were collected from all springs/geysers in the study area. This isotope abundance also supports that CO_2 is of the same crustal origins in the LGW/SW fault zones as well as Tumbleweed and Chaffin Ranch Geysers. However, the amount of CO_2 brought to these geysers is perhaps not considerable since CO_2 becomes depleted due to leakage within the fault zones during transport. As a result, CO_2 eruptions occur on a smaller scale at Tumbleweed and Chaffin Ranch Geysers than other springs/geysers in the LGW and SW fault zones (Glennon and Pfaff, 2005).

6. Conclusions

CO_2-driven geysers and springs and associated soil CO_2 discharge within the LGW and SW fault zones well demonstrate the potential consequences of the GCS project failures and importance of geologic features (Bickle and Kampman, 2013; Han et al., 2013a; Shipton et al., 2005). Specifically, fault has three basic elements of architecture which affect fluid movement as a conduit or barrier: (1) juxtaposition, (2) fault core, and (3) the surrounding damage zone (Aydin, 2000). Other parameters such as slip magnitude, cementation, and stress state (shearing) could also have an effect on fluid

migration in the subsurface. Although our model was not capable of distinguishing fault core and the damage zone due to a grid-scale effect, simulation results showed that aquitards being juxtaposed to aquifers cannot be an ultimate seal for CO_2 and brine leak without much help from low-k fault (Figs. 10a-d). In addition, even very low-k fault cannot completely prevent CO_2 ascent towards the surface (Fig. 8b) if sufficient amount of CO_2 is supplied from deep sources over geological time (~20 ka) and thus the related pressure build-up exceeds a critical threshold. Consequentially, low-k fault facilitates the formation of a CO_2 anticlinal trap within the shallow aquifers (Navajo and Entrada Sandstones) at a depth above 300 m, resulting in high fluid pressure build-up capable of opening fractures (Fig. 9a). If so, a large amount of CO_2 that can be comparable to the high-k fault case could leak to the surface via newly formed fractures albeit the fault is low-permeable.

Combined with the fact of regional groundwater flowing southward, the Green River anticline plunging north gives rise to a distinctive feature of CO_2 transport between the LGW and SW fault zones. Simulation results always exhibited the potential CO_2 contribution from the LGW to SW fault zones irrespective of the regional k values of the fault (Figs. 10a and 10b). In other words, certain amounts of CO_2 and brine originated in the LGW fault zone are brought southward to shallower depths in the SW fault zone (6 km distance), following the dip of the Green River anticline (Figs. 8e, 9b, and 10). Because a new input of CO_2 and brine comes from north (the LGW fault zone), the northern area of the SW fault manifests more CO_2 leaking characteristics: the abundance of CO_2-driven geysers and springs, and higher soil CO_2 flux (32.10 g m^{-2} d^{-1} at the 90^{th} percentile) relative to the southern area (9.61 g m^{-2} d^{-1} at the 90^{th} percentile) (Table 6). In

addition, the computed results showing the shared CO_2 origin between two fault zones coincide with the previous observations of a progressive chemical evolution of water discharge from the LGW to SW fault zones (Kampman et al., 2009) and constant gas isotopic ratio throughout the region (Wilkinson et al., 2009) (refer to the section 2.2 for detail). This provides an idea that one should carefully determine the location and depth of a target reservoir for GCS over a large lateral extent as the spreading of CO_2 plume could advance to shallower depths and finally reach the surface along the formation slope.

The formation of an anticlinal trap also appears as an important process to cause a "high-energy" CO_2 discharge through a well in the geyser simulations. Such secondary CO_2 reservoir near the surface provides a conducive environment for amplifying geyser-like eruptions such as: (1) multiphase conditions which reduce fluid mobility of each phase and thus enable large accumulations of CO_2 before discharge, (2) resultant overpressures (Figs. 11a and 13a) which drive the first burp of brine (Figs. 12a and 12b) and high rate discharge of CO_2 and brine in the later stage (Figs. 12a, 12c and 13e), and (3) sufficient heat transfer between flowing CO_2-rich fluids and surrounding formations that enhances the development of multiphase conditions by exsolution of aqueous CO_2 and/or boiling of liquid CO_2. In addition, the creation of a secondary CO_2 reservoir could be much more harmful since it is generally accompanied by contamination of shallow potable groundwater resources. Therefore, the fact that low-k fault could form a secondary CO_2 reservoir at shallow depths needs to be taken into account during the initial screening stage of GCS.

CO_2-driven cold-water geysering appears around the world yet it is not a universal phenomenon, which can be observed only from a manmade well (Glennon and Pfaff, 2005). The exact reason has not been fully elucidated but may be deeply related to the formation of Taylor bubbles essential for geyser-like eruption (Lu, 2004). This is because an artificial wellbore could provide an intact, adequate opening neither too large nor too small to develop gas slugs and also to enhance vertical acceleration; by contrast, natural fractures/faults are generally too tiny in their size and lack uniform flow paths due to innate obstacles such as mineral matrix and cementation, and rock fragments.

Unfortunately, it could not be evaluated from our simulations that how long the eruption at Crystal Geyser would last. However, the vigorous eruption at Crystal Geyser over the last 8 decades implies that tremendous supply of CO_2 makes a century-long high velocity discharge possible. The computed results also displayed pseudo-geyser eruptions at the surface under incessant CO_2 feed to a wellbore assured (Figs. 12a, 12c, 13e, and 14a-c). The cycling behavior of CO_2 leakage indeed culminated in a constant discharge of CO_2 gas with or without brine, suggesting the potential shift of Crystal Geyser to a CO_2-driven cold-water spring or even a fumarole in the future. However, our assumptions on the model exerted several limitations on an exact representation of the field including Crystal Geyser and the LGW fault. Further study is needed to investigate an intimate conditions that induces CO_2-driven geyser eruption and a long-term fate of geyser by taking crucial parameters (e.g., water drain back at the surface during the eruption and an exact distinction in fault structure between fault core and damage zone) into consideration and using more accurate model of wellbore flow (e.g., pipe flow (Lu, 2004;

Lu et al., 2006; Watson et al., 2014) or drift flux model (Pruess, 2008b)) rather than Darcian approach under specific circumstances at the targeted region.

References

Allen, E.T., Day, A.L., 1935. Hot springs of the Yellowstone National Park. Carnegie Institution of Washington, Washington, D.C.

Allis, R., Bergfeld, D., Moore, J., McClure, K., Morgan, C., Chidsey, T., Heath, J., McPherson, B., 2005a. Implications of results from CO_2 flux surveys over known CO_2 systems for long-term monitoring, the 4th Annual Conference on Carbon Capture and Sequestration. U.S. DOE/NETL, Alexandria, VA, pp. 2-5.

Allis, R., Bergfeld, D., Moore, J., McClure, K., Morgan, C., Chidsey, T.C., Heath, J., McPherson, B.J., 2005b. Implications of results from CO_2 flux surveys over known CO_2 systems for long-term monitoring, the 4th Annual Conference on Carbon Capture and Sequestration, Alexandria, VA.

Allis, R., Chidsey, T.C., Gwynn, W., Morgan, C., White, S., Adams, M., Moore, J., 2001. Natural CO_2 reservoirs on the Colorado plateau and southern Rocky Mountains: candidates for CO_2 sequestration, the 1st Annual Conference on Carbon and Sequestration. U.S. DOE/NETL, Alexandria, VA.

Anderson, S., Newell, R., 2004. PROSPECTS FOR CARBON CAPTURE AND STORAGE TECHNOLOGIES. Annual Review of Environment and Resources 29, 109-142.

Arts, R., Chadwick, A., Eiken, O., Thibeau, S., Nooner, S., 2008. Ten years' experience of monitoring CO_2 injection in the Utsira Sand at Sleipner, offshore Norway. First break 26, 65-72.

Assayag, N., Bickle, M., Kampman, N., Becker, J., 2009. Carbon isotope constraints on CO_2 degassing in cold-water geyser, Green river, Utah. Energy Procedia 1, 2361-2366.

Aydin, A., 2000. Fractures, faults, and hydrocarbon entrapment, migration and flow. Marine and Petroleum Geology 17, 797-814.

Bachu, S., 2000. Sequestration of CO_2 in geological media: criteria and approach for site selection in response to climate change. Energy Conversion and Management 41, 953-970.

Bachu, S., Bennion, B., 2008. Effects of in-situ conditions on relative permeability characteristics of CO_2-brine systems. Environ Geol 54, 1707-1722.

Baer, J., Rigby, J., 1978. Geology of the Crystal geyser and environmental implications of its effluent, Grand County, Utah. Utah Geology 5, 125-130.

Bense, V.F., Person, M.A., 2006. Faults as conduit-barrier systems to fluid flow in siliciclastic sedimentary aquifers. Water Resources Research 42, W05421.

Benson, S.M., Hepple, R., Apps, J., Tsang, C.-F., Lippmann, M., 2002. Lessons Learned from Natural and Industrial Analogues for Storage of Carbon Dioxide in Deep Geological Formations. Lawrence Berkeley National Laboratory, Berkeley, CA.

Bickle, M., Kampman, N., 2013. Lessons in carbon storage from geological analogues. geology 41, 525-526.

Birkholzer, J.T., Zhou, Q., Tsang, C.-F., 2009. Large-scale impact of CO_2 storage in deep saline aquifers: A sensitivity study on pressure response in stratified systems. International Journal of Greenhouse Gas Control 3, 181-194.

Burnside, N.M., 2010. U-Th dating of travertine on the Colorado Plateau: Implications for the leakage of geologically stored CO_2, Department of Geographical and Earth Sciences. University of Glasgow, Scotland, UK, p. 290.

Burnside, N.M., Shipton, Z.K., Dockrill, B., Ellam, R.M., 2013. Man-made versus natural CO_2 leakage: A 400 k.y. history of an analogue for engineered geological storage of CO_2. geology 41, 471-474.

Burton, M., Kumar, N., Bryant, S.L., 2009. CO_2 injectivity into brine aquifers: Why relative permeability matters as much as absolute permeability. Energy Procedia 1, 3091-3098.

Caine, J.S., Evans, J.P., Forster, C.B., 1996. Fault zone architecture and permeability structure. Geology 24, 1025-1028.

Cappa, J., Rice, D., 1995. Carbon dioxide in Mississippian rocks of the Paradox Basin and adjacent areas, Colorado, Utah, New Mexico, and Arizona. U.S. GPO, Washington, D.C., p. 21.

Carey, J.W., Wigand, M., Chipera, S.J., WoldeGabriel, G., Pawar, R., Lichtner, P.C., Wehner, S.C., Raines, M.A., Guthrie Jr, G.D., 2007. Analysis and performance of oil well cement with 30 years of CO_2 exposure from the SACROC Unit, West Texas, USA. International Journal of Greenhouse Gas Control 1, 75-85.

Castelletto, N., Teatini, P., Gambolati, G., Bossie-Codreanu, D., Vincké, O., Daniel, J.-M., Battistelli, A., Marcolini, M., Donda, F., Volpi, V., 2013. Multiphysics modeling of CO_2 sequestration in a faulted saline formation in Italy. Advances in Water Resources 62, Part C, 570-587.

Celia, M.A., Bachu, S., 2003. Geological Sequestration of CO_2: Is Leakage Unavoidable and Acceptable?, in: Gale, J., Kaya, Y. (Eds.), Greenhouse Gas Control Technologies - 6th International Conference. Pergamon, Oxford, pp. 477-482.

Chidsey, T.C., Jr., Wakefield, S., Hill, B.G., Hebertson, M., 2004. Oil and gas fields map of Utah, p. Utah Geological Survey Map 203DM.

Class, H., Ebigbo, A., Helmig, R., Dahle, H.K., Nordbotten, J.M., Celia, M.A., Audigane, P., Darcis, M., Ennis-King, J., Fan, Y., Flemisch, B., Gasda, S.E., Jin, M., Krug, S.,

Labregere, D., Beni, A.N., Pawar, R.J., Sbai, A., Thomas, S.G., Trenty, L., Wei, L., 2009. A benchmark study on problems related to CO2 storage in geologic formations. Computational Geoscience 13, 409-434.

Dockrill, B., Shipton, Z.K., 2010. Structural controls on leakage from a natural CO_2 geologic storage site: Central Utah, U.S.A. Journal of Structural Geology 32, 1768-1782.

Doelling, H., 2002. Interim geologic map of the San Rafael Desert 30′ x 60′ quadrangle, Emery and Grand Counties, Utah, Emery and Grand Counties, Utah: Utah Geological Survey Open-File Report. Utah Geological Survey Division of Utah Department of Natural Resources, Salt Lake City, UT.

Duan, Z., Sun, R., 2003. An improved model calculating CO_2 solubility in pure water and aqueous NaCl solutions from 273 to 533 K and from 0 to 2000 bar. Chemical Geology 193, 257-271.

Ennis-King, J., Paterson, L., 2003. Role of Convective Mixing in the Long-Term Storage of Carbon Dioxide in Deep Saline Formations, SPE annual technical conference and exhibition. Society of Petroleum Engineers.

Farrar, C., Sorey, M., Evans, W., Howle, J., Kerr, B., Kennedy, B.M., King, C.-Y., Southon, J., 1995. Forest-killing diffuse CO_2 emission at Mammoth Mountain as a sign of magmatic unrest. Nature 376, 675-678.

Foxford, K.A., Walsh, J.J., Watterson, J., Garden, I.R., Guscott, S.C., Burley, S.D., 1998. Structure and content of the Moab Fault Zone, Utah, USA, and its implications for fault seal prediction. Geological Society, London, Special Publications 147, 87-103.

Gale, J., 2004. Geological storage of CO2: What do we know, where are the gaps and what more needs to be done? Energy 29, 1329-1338.

Gale, J., Christensen, N.P., Cutler, A., Torp, T.A., 2001. Demonstrating the Potential for Geological Storage of CO_2: The Sleipner and GESTCO Projects. Environmental Geosciences 8, 160-165.

García, J.E., 2001. Density of aqueous solutions of CO_2. Lawrence Berkeley National Laboratory, Berkeley, CA.

Gherardi, F., Xu, T., Pruess, K., 2007. Numerical modeling of self-limiting and self-enhancing caprock alteration induced by CO_2 storage in a depleted gas reservoir. Chemical Geology 244, 103-129.

Glennon, J.A., Pfaff, R.M., 2005. The operation and geography of carbon-dioxide-driven, cold-water geysers. GOSA Transactions 9, 184-192.

Gouveia, F.J., Friedmann, S.J., 2006. Timing and prediction of CO_2 eruptions from crystal geyser, UT. Lawrence Livermore National Laboratory, Livermore, CA, p. 14.

Han, W.S., Kim, K.-Y., Esser, R.P., Park, E., McPherson, B.J., 2011. Sensitivity study of simulation parameters controlling CO_2 trapping mechanisms in saline formation. Transport in Porous Media 90, 807-829.

Han, W.S., Kim, K.-Y., Park, E., McPherson, B.J., Lee, S.-Y., Park, M.-H., 2012. Modeling of Spatiotemporal Thermal Response to CO_2 Injection in Saline Formations: Interpretation for Monitoring. Transport in Porous Media 93, 381–399.

Han, W.S., Lu, M., McPherson, B.J., Keating, E.H., Moore, J., Park, E., Watson, Z.T., Jung, N.-H., 2013a. Characteristics of CO_2-driven cold-water geyser, Crystal Geyser in Utah: experimental observation and mechanism analyses. Geofluids 13, 283-297.

Han, W.S., Lu, M., McPherson, B.J., Keating, E.H., Moore, J., Park, E., Watson, Z.T., Jung, N.H., 2013b. Characteristics of CO_2-driven cold-water geyser, Crystal Geyser in Utah: experimental observation and mechanism analyses. Geofluids 13, 283-297.

Han, W.S., McPherson, B.J., Lichtner, P.C., Wang, F.P., 2010a. Evaluation of trapping mechanisms in geologic CO_2 sequestration: Case study of SACROC northern platform, a 35-year CO_2 injection site. American Journal of Science 310, 282-324.

Han, W.S., Stillman, G.A., Lu, M., Lu, C., McPherson, B.J., Park, E., 2010b. Evaluation of potential nonisothermal processes and heat transport during CO_2 sequestration. Journal of Geophysical Research: Solid Earth 115, B07209.

Hansley, P.L., 1995. Diagenetic and burial history of the Lower Permian White Rim Sandstone in the tar sand triangle, Paradox basin, southeastern Utah. U.S. GPO, Washington, D.C., p. 24.

Hassanzadeh, H., Pooladi-Darvish, M., Keith, D.W., 2005. Modelling of Convective Mixing in CO_2 Storage. Journal of Canadian Petroleum Technology 44, 43-51.

Haszeldine, R., S., Quinn, O., England, G., Wilkinson, M., Shipton, Z., K., Evans, J., P., Heath, J., Crossey, L., Ballentine, C., J., Graham, C., M., 2005. Natural Geochemical Analogues for Carbon Dioxide Storage in Deep Geological Porous Reservoirs, a United Kingdom Perspective. Oil & Gas Science and Technology - Rev. IFP 60, 33-49.

Heath, J.E., Lachmar, T.E., Evans, J.P., Kolesar, P.T., Williams, A.P., 2009. Hydrogeochemical characterization of leaking, carbon dioxide-charged fault zones in east-central Utah, with implications for geologic carbon storage, in: Mcpherson, B.J., Sundquist, E.T. (Eds.), Carbon Sequestration and Its Role in the Global Carbon Cycle. American Geophysical Union, Washington, D. C., pp. 147-158.

Holloway, S., 2005. Underground sequestration of carbon dioxide—a viable greenhouse gas mitigation option. Energy 30, 2318-2333.

Hood, J.W., Patterson, D.J., 1984. Bedrock aquifers in the northern San Rafael Swell area, Utah, with special emphasis on the Navajo Sandstone. The State of Utah Department of Natural Resources, Salt Lake City, UT, p. 128.

Ingebritsen, S.E., Rojstaczer, S.A., 1996. Geyser periodicity and the response of geysers to deformation. Journal of Geophysical Research: Solid Earth 101, 21891-21905.

IPCC, 2005. IPCC Special Report on Carbon Dioxide Capture and Storage, in: Bert Metz, O.D., Heleen de Coninck, Manuela Loos, Leo Meyer (Ed.), Contribution of Working Group III. Cambridge University Press, Cambridge, UK and New York, NY, USA, p. 442.

IPCC, 2007. Climate Change 2007: The Physical Science Basis, in: Solomon, S., Qin, D., Manning, M., Chen, Z., Marquis, M., Averyt, K.B., Tignor, M., Miller,H.L. (Ed.), Contribution of Working Group I. Cambridge University Press, Cambridge, UK and New York, NY, USA, p. 996.

Jung, N.-H., Han, W.S., Watson, Z.T., Graham, J.P., Kim, K.-Y., 2014. Fault-Controlled CO_2 Leakage from Natural Reservoirs in the Colorado Plateau, East-Central Utah. Earth and Planetary Science Letters 403, 358-367.

Kampman, N., Bickle, M., Becker, J., Assayag, N., Chapman, H., 2009. Feldspar dissolution kinetics and Gibbs free energy dependence in a CO_2-enriched groundwater system, Green River, Utah. Earth and Planetary Science Letters 284, 473-488.

Kampman, N., Bickle, M., Wigley, M., Dubacq, B., 2014a. Fluid flow and CO_2–fluid–mineral interactions during CO_2-storage in sedimentary basins. Chemical Geology 369, 22-50.

Kampman, N., Burnside, N.M., Shipton, Z.K., Chapman, H.J., Nicholl, J.A., Ellam, R.M., Bickle, M.J., 2012. Pulses of carbon dioxide emissions from intracrustal faults following climatic warming. Nature Geoscience 5, 352-358.

Kampman, N., Maskell, A., Chapman, H.J., Bickle, M.J., Evans, J.P., Purser, G., Zhou, Z., Gattacceca, J., Schaller, M., Bertier, P., Chen, F., Turchyn, A.S., Assayag, N., Rochelle, C., Busch, A., 2014b. Drilling and sampling a natural CO_2 reservoir: Implications for fluid flow and CO_2-fluid-rock reactions during CO_2 migration through the overburden. Chemical Geology 369, 51-82.

Kampman, N., Maskell, A., Chapman, H.J., Bickle, M.J., Evans, J.P., Purser, G., Zhou, Z., Gattacceca, J., Schaller, M., Bertier, P., Chen, F., Turchyn, A.S., Assayag, N., Rochelle, C., Busch, A., 2014b. Drilling and sampling a natural CO_2 reservoir: Implications for fluid flow and CO_2-fluid-rock reactions during CO_2 migration through the overburden. Chemical Geology 369, 51-82.

Keating, E.H., Fessenden, J., Kanjorski, N., Koning, D., Pawar, R., 2010. The impact of CO_2 on shallow groundwater chemistry: observations at a natural analog site and implications for carbon sequestration. Environ Earth Sci 60, 521-536.

Kelsey, M.R., 1991. River Guide to Canyonlands National Parks and Vicinity: Hiking, Camping, Geology, Archaeology, and Steamboating, Cowboy, Ranching & Trail Building History. Kelsey Publishing, Salt Lake City, Utah.

Kharaka, Y.K., Thordsen, J., Kakouros, E., Ambats, G., Herkelrath, W., Beers, S., Birkholzer, J., Apps, J., Spycher, N., Zheng, L., Trautz, R., Rauch, H., Gullickson, K., 2010. Changes in the chemistry of shallow groundwater related to the 2008 injection of CO_2 at the ZERT field site, Bozeman, Montana. Environ Earth Sci 60, 273-284.

Klusman, R.W., 2005. Baseline studies of surface gas exchange and soil-gas composition in preparation for CO_2 sequestration research: Teapot Dome, Wyoming. AAPG bulletin 89, 981-1003.

Kneafsey, T.J., Pruess, K., 2010. Laboratory Flow Experiments for Visualizing Carbon Dioxide-Induced, Density-Driven Brine Convection. Transport in Porous Media 82, 123-139.

Knipe, R.J., Jones, G., Fisher, Q.J., 1998. Faulting, fault sealing and fluid flow in hydrocarbon reservoirs: an introduction. Geological Society, London, Special Publications 147, vii-xxi.

Korbøl, R., Kaddour, A., 1995. Sleipner vest CO_2 disposal - injection of removed CO_2 into the utsira formation. Energy Conversion and Management 36, 509-512.

Krevor, S.C.M., Pini, R., Zuo, L., Benson, S.M., 2012. Relative permeability and trapping of CO_2 and water in sandstone rocks at reservoir conditions. Water Resources Research 48, W02532.

Lewicki, J.L., Birkholzer, J., Tsang, C.-F., 2007. Natural and industrial analogues for leakage of CO_2 from storage reservoirs: identification of features, events, and processes and lessons learned. Environ Geol 52, 457-467.

Lewicki, J.L., Brantley, S.L., 2000. CO_2 degassing along the San Andreas fault, Parkfield, California. Geophysical Research Letters 27, 5-8.

Lewicki, J.L., Evans, W.C., Hilley, G.E., Sorey, M.L., Rogie, J.D., Brantley, S.L., 2003. Shallow soil CO_2 flow along the San Andreas and Calaveras Faults, California. Journal of Geophysical Research: Solid Earth 108, 2187.

Lindeberg, E., Bergmo, P., 2003. The long-term fate of CO_2 injected into an aquifer. Greenhouse Gas Control Technologies 1, 489-494.

Lu, X., 2004. An Investigation of Transient Two-phase Flow in Vertical Pipes with Particular Reference to Geysering, Department of Mechanical Engineering. University of Auckland, Auckland, New Zealand, p. 254.

Lu, X., Watson, A., Gorin, A.V., Deans, J., 2005. Measurements in a low temperature CO_2-driven geysering well, viewed in relation to natural geysers. Geothermics 34, 389-410.

Lu, X., Watson, A., Gorin, A.V., Deans, J., 2006. Experimental investigation and numerical modelling of transient two-phase flow in a geysering geothermal well. Geothermics 35, 409-427.

Mathias, S.A., Gluyas, J.G., Oldenburg, C.M., Tsang, C.-F., 2010. Analytical solution for Joule–Thomson cooling during CO_2 geo-sequestration in depleted oil and gas reservoirs. International Journal of Greenhouse Gas Control 4, 806-810.

Mayo, A.L., Shrum, D.B., Chidsey, T.C., 1991. Factors contributing to exsolving carbon dioxide in ground water systems in the Colorado plateau, Utah in: Chidsey, T.C. (Ed.), Geology of east-central Utah. Utah Geological Survey, Salt Lake City, pp. 335-341.

McCord, S.A., Schladow, S.G., 1998. Numerical simulations of degassing scenarios for CO_2-rich Lake Nyos, Cameroon. Journal of Geophysical Research: Solid Earth 103, 12355-12364.

Mukhopadyay, S., Birkholzer, J.T., Nicot, J.-P., Hosseini, S.A., 2012. A model comparison initiative for a CO_2 injection field test: an introduction to Sim-SEQ. Environ Earth Sci 67, 601-611.

Murray, C., 1989. The cold water geyser of Utah, II: Observation of Crystal Geyser. The Geyser Observation and Study Association 2, 133-139.

Nechayev, A., 2012. About the mechanism of geyser eruption. arXiv preprint arXiv:1204.1560, 13 p.

Nuccio, V.F., Condon, S.M., 1996. Burial and Thermal History of the Paradox Basin, Utah and Colorado, and Petroleum Potential of the Middle Pennsylvanian Paradox Formation. U.S. GPO, Washington, D.C., p. 41.

Oldenburg, C.M., 2007. Joule-Thomson cooling due to CO_2 injection into natural gas reservoirs. Energy Conversion and Management 48, 1808-1815.

Oldenburg, C.M., Lewicki, J., Dobeck, L., Spangler, L., 2010. Modeling Gas Transport in the Shallow Subsurface During the ZERT CO_2 Release Test. Transport in Porous Media 82, 77-92.

Oldenburg, C.M., Pruess, K., Benson, S.M., 2001. Process Modeling of CO_2 Injection into Natural Gas Reservoirs for Carbon Sequestration and Enhanced Gas Recovery. Energy & Fuels 15, 293-298.

Oldenburg, C.M., Rinaldi, A., 2011. Buoyancy Effects on Upward Brine Displacement Caused by CO_2 Injection. Transport in Porous Media 87, 525-540.

Oldenburg, C.M., Unger, A.J.A., 2003. On Leakage and Seepage from Geologic Carbon Sequestration Sites. Vadose Zone J. 2, 287-296.

Pearce, J., Czernichowski-Lauriol, I., Lombardi, S., Brune, S., Nador, A., Baker, J., Pauwels, H., Hatziyannis, G., Beaubien, S., Faber, E., 2004. A review of natural CO_2 accumulations in Europe as analogues for geological sequestration. Geological Society, London, Special Publications 233, 29-41.

Price, P.N., McKone, T.E., Sohn, M.D., 2007. Carbon Sequestration Risks and Risk Management. Lawrence Berkeley National Laboratory, Berkeley, CA, p. 22.

Pruess, K., 2008a. Leakage of CO2 from geologic storage: Role of secondary accumulation at shallow depth. International Journal of Greenhouse Gas Control 2, 37-46.

Pruess, K., 2008b. On CO_2 fluid flow and heat transfer behavior in the subsurface, following leakage from a geologic storage reservoir. Environ Geol 54, 1677-1686.

Pruess, K., García, J., 2002. Multiphase flow dynamics during CO_2 disposal into saline aquifers. Environ Geol 42, 282-295.

Pruess, K., Moridis, G., Oldenburg, C.M., 1999. TOUGH2 user's guide, version 2.0. Lawrence Berkeley National Laboratory Berkeley, Berkeley, CA.

Raich, J., Schlesinger, W.H., 1992. The global carbon dioxide flux in soil respiration and its relationship to vegetation and climate. Tellus B 44, 81-99.

Reichle, D., Houghton, J., Kane, B., Ekmann, J., 1999. Carbon sequestration research and development, Other Information: PBD: 31 Dec 1999. U.S. Department of Energy, Washington, D.C.

Roberts, J.J., Wood, R.A., Haszeldine, R.S., 2011. Assessing the health risks of natural CO_2 seeps in Italy. Proceedings of the National Academy of Sciences 108, 16545-16548.

Rochelle, C., Pearce, J., Holloway, S., 1999. The underground sequestration of carbon dioxide: containment by chemical reactions in the deep geosphere. Geological Society, London, Special Publications 157, 117-129.

Rogie, J.D., Kerrick, D.M., Chiodini, G., Frondini, F., 2000. Flux measurements of nonvolcanic CO_2 emission from some vents in central Italy. Journal of Geophysical Research: Solid Earth 105, 8435-8445.

Rogie, J.D., Kerrick, D.M., Sorey, M.L., Chiodini, G., Galloway, D.L., 2001. Dynamics of carbon dioxide emission at Mammoth Mountain, California. Earth and Planetary Science Letters 188, 535-541.

Sherzer, W.H., 1933. An interpretation of Bunsen's geyser theory. The Journal of Geology 41, 501-512.

Shipton, Z.K., Evans, J.P., Dockrill, B., Heath, J., Williams, A., Kirchner, D., Kolesar, P.T., 2005. Natural leaking CO_2-charged system as analogs for failed geologic storage reservoirs, in: Thomas, D.C., Benson, S.M. (Eds.), Carbon Dioxide Capture for Storage in Deep Geologic Formations. Elsevier, New York, NY, pp. 699-712.

Shipton, Z.K., Evans, J.P., Kirschner, D., Kolesar, P.T., Williams, A.P., Heath, J., 2004. Analysis of CO_2 leakage through 'low-permeability' faults from natural reservoirs in the

Colorado Plateau, east-central Utah, in: Baines, S.J., Worden, R.H. (Eds.), Geological Storage of Carbon Dioxide. Geological Society of London, London, pp. 43-58.

Sigurdsson, H., Devine, J.D., Tchua, F.M., Presser, F.M., Pringle, M.K.W., Evans, W.C., 1987. Origin of the lethal gas burst from Lake Monoun, Cameroun. Journal of Volcanology and Geothermal Research 31, 1-16.

Siirila, E.R., Navarre-Sitchler, A.K., Maxwell, R.M., McCray, J.E., 2012. A quantitative methodology to assess the risks to human health from CO_2 leakage into groundwater. Advances in Water Resources 36, 146-164.

Smyth, R.C., Hovorka, S.D., Lu, J., Romanak, K.D., Partin, J.W., Wong, C., Yang, C., 2009. Assessing risk to fresh water resources from long term CO_2 injection–laboratory and field studies. Energy Procedia 1, 1957-1964.

Span, R., Wagner, W., 1996. A New Equation of State for Carbon Dioxide Covering the Fluid Region from the Triple-Point Temperature to 1100 K at Pressures up to 800 MPa. Journal of Physical and Chemical Reference Data 25, 1509-1596.

Steinberg, G., Merzhanov, A., Steinberg, A., Rasina, A., 1982. Geyser process: its theory, modeling, and field experiment. Part 2. A laboratory model of a geyser. Modern Geology 8, 71-74.

Taku Ide, S., Jessen, K., Orr Jr, F.M., 2007. Storage of CO_2 in saline aquifers: Effects of gravity, viscous, and capillary forces on amount and timing of trapping. International Journal of Greenhouse Gas Control 1, 481-491.

Tueckmantel, C., Fisher, Q.J., Manzocchi, T., Skachkov, S., Grattoni, C.A., 2012. Two-phase fluid flow properties of cataclastic fault rocks: Implications for CO_2 storage in saline aquifers. Geology 40, 39-42.

van Genuchten, M.T., 1980. A closed-form equation for predicting the hydraulic conductivity of unsaturated soils. Soil Science Society of America Journal 44, 892-898.

Vilarrasa, V., Bolster, D., Dentz, M., Olivella, S., Carrera, J., 2010. Effects of CO_2 Compressibility on CO_2 Storage in Deep Saline Aquifers. Transport in Porous Media 85, 619-639.

Watson, Z.T., Han, W.S., Keating, E.H., Jung, N.-H., Lu, M., 2014. Eruption dynamics of CO_2-driven cold-water geysers: Crystal, Tenmile geysers in Utah and Chimayó geyser in New Mexico. Earth and Planetary Science Letters 408, 272-284.

White, C.M., Strazisar, B.R., Granite, E.J., Hoffman, J.S., Pennline, H.W., 2003. Separation and Capture of CO_2 from Large Stationary Sources and Sequestration in Geological Formations—Coalbeds and Deep Saline Aquifers. Journal of the Air & Waste Management Association 53, 645-715.

White, S.P., Allis, R.G., Bergfeld, D., Moore, J.N., Chidsey, T.C., Morgan, C., McClure, K., Adams, M., Rauzi, S., 2004. Evaluating the seal integrity of natural CO_2 reservoirs of

the Colorado Plateau, Proceedings of the 3rd National Conference on Carbon Sequestration, Washington D.C., p. 32.

Wigley, M., Dubacq, B., Kampman, N., Bickle, M., 2013a. Controls of sluggish, CO2-promoted, hematite and K-feldspar dissolution kinetics in sandstones. Earth and Planetary Science Letters 362, 76-87.

Wigley, M., Kampman, N., Chapman, H., Dubacq, B., Bickle, M., 2013b. In situ redeposition of trace metals mobilized by CO2-charged brines. Geochemistry, Geophysics, Geosystems 14, 1321-1332.

Wigley, M., Kampman, N., Dubacq, B., Bickle, M., 2012. Fluid-mineral reactions and trace metal mobilization in an exhumed natural CO2 reservoir, Green River, Utah. Geology 40, 555-558.

Wilkinson, M., Gilfillan, M.V., Haszeldine, R.S., Ballentine, C.J., 2008. Plumbing the depths: Testing natural tracers of subsurface CO_2 origin and migration, Utah, in: Grobe, M., Pashin, J.C., Dodge, R.L. (Eds.), Carbon dioxide sequestration in geologic media-State of the scienec. American Association of Petroleum Geologists, pp. 619-634.

Wilkinson, M., Gilfillan, M.V., Haszeldine, R.S., Ballentine, C.J., 2009. Plumbing the depths: Testing natural tracers of subsurface CO_2 origin and migration, Utah, in: Grobe, M., Pashin, J.C., Dodge, R.L. (Eds.), Carbon dioxide sequestration in geologic media-State of the science. American Association of Petroleum Geologists, pp. 619-634.

Williams, A.P., 2005. Structural Analysis of CO_2 Leakage Through the Salt Wash and Little Grand Wash Faults from Natural Reservoirs in the Colorado Plateau, Southeastern Utah, Department of Geology. Utah State University, Logan, UT, p. 188.

Zhang, K., Wu, Y.-S., Pruess, K., 2008. User's guide for TOUGH2-MP-a massively parallel version of the TOUGH2 code, SPE-106817-PA. Lawrence Berkeley National Laboratory, Berkeley, CA.

Appendix A

Soil Gaseous CO_2 Flux and Concentration Raw Data: the Little Grand Wash Fault Zone

Observation Name	Decimal Degrees Latitude	Decimal Degrees Longitude	CO_2 Flux ($g\ m^{-2}\ d^{-1}$)	Mean [CO_2] (ppm)
CGMUDPOT2	38.9384	-110.1352	7882.5	7991.3
CGMUDPOT3	38.9384	-110.1352	2125.6	40680.1
CGMUDPOT4	38.9384	-110.1352	6100.1	4465.5
CGMUDPOT5	38.9384	-110.1352	5092.1	4591.6
CGMUDPOT6mean	38.9384	-110.1352	35757.5	37513.3
CGMUDPOT7mean	38.9384	-110.1352	704.3	1020.0
LINE1.1	38.9354	-110.1228	3.6	410.4
LINE1.2mean	38.9358	-110.1228	6.3	410.3
LINE1.3mean	38.9361	-110.1228	5.0	411.1
LINE1.4mean	38.9364	-110.1228	18.0	418.0
LINE1.5mean	38.9367	-110.1228	301.4	599.8
LINE1.6mean	38.9369	-110.1226	109.5	495.5
LINE1.7mean	38.9371	-110.1225	83.9	472.8
LINE1.8	38.9374	-110.1228	0.0	406.2
LINE10.1	38.9363	-110.1294	0.0	399.4
LINE10.10	38.9357	-110.1261	4.4	410.2
LINE10.11	38.9362	-110.1255	0.0	404.0
LINE10.12	38.9362	-110.1253	0.0	400.0
LINE10.13	38.9362	-110.1249	0.0	398.0
LINE10.14	38.9364	-110.1245	0.0	400.0
LINE10.15	38.9365	-110.1244	2.6	410.3
LINE10.16mean	38.9364	-110.1239	186.1	569.4
LINE10.17	38.9364	-110.1237	0.0	400.2
LINE10.2	38.9364	-110.1288	10.0	413.2
LINE10.3	38.9363	-110.1285	0.0	403.0
LINE10.4	38.9363	-110.1283	0.1	404.1
LINE10.5	38.9363	-110.1282	12.7	415.4
LINE10.6	38.9361	-110.1278	10.3	412.1
LINE10.7	38.9361	-110.1272	0.0	388.4
LINE10.8	38.9362	-110.1269	0.0	400.9
LINE10.9	38.9362	-110.1266	0.0	392.5
LINE11.10	38.9369	-110.1266	8.9	414.7
LINE11.11	38.9369	-110.1269	2.9	410.0
LINE11.12	38.9370	-110.1273	0.0	406.7
LINE11.13	38.9371	-110.1280	0.0	397.0
LINE11.14	38.9369	-110.1286	0.0	405.9
LINE11.15	38.9368	-110.1296	2.6	409.3
LINE11.16	38.9368	-110.1301	0.0	405.3
LINE11.1mean	38.9365	-110.1230	5514.7	4455.1
LINE11.2	38.9365	-110.1232	17.3	424.9

Observation Name	Decimal Degrees Latitude	Decimal Degrees Longitude	CO_2 Flux ($g\ m^{-2}\ d^{-1}$)	Mean [CO_2] (ppm)
LINE11.3	38.9365	-110.1234	0.1	409.4
LINE11.4	38.9366	-110.1240	3.9	412.7
LINE11.5	38.9369	-110.1245	17.7	422.2
LINE11.6	38.9370	-110.1250	0.5	408.0
LINE11.7	38.9370	-110.1253	0.0	402.3
LINE11.8	38.9370	-110.1255	0.0	420.7
LINE11.9	38.9370	-110.1259	0.0	408.1
LINE12.1	38.9373	-110.1298	0.0	412.2
LINE12.10	38.9373	-110.1269	4.2	407.5
LINE12.11	38.9376	-110.1266	0.0	399.2
LINE12.12	38.9376	-110.1259	14.6	422.1
LINE12.13	38.9375	-110.1255	24.8	436.6
LINE12.14	38.9376	-110.1253	0.0	400.9
LINE12.15	38.9376	-110.1251	38.7	437.0
LINE12.16	38.9375	-110.1246	3.1	414.2
LINE12.17	38.9374	-110.1243	12.2	415.5
LINE12.18	38.9374	-110.1239	0.0	401.0
LINE12.19	38.9372	-110.1239	0.0	404.3
LINE12.2	38.9371	-110.1293	0.0	396.2
LINE12.3mean	38.9373	-110.1290	408.6	787.0
LINE12.4	38.9372	-110.1287	9.4	428.0
LINE12.5	38.9373	-110.1284	9.4	415.8
LINE12.6	38.9373	-110.1282	0.0	401.7
LINE12.7	38.9372	-110.1279	0.0	403.3
LINE12.8	38.9373	-110.1275	0.0	402.7
LINE12.9	38.9373	-110.1271	60.8	471.9
LINE13.1	38.9383	-110.1250	2.7	410.4
LINE13.10	38.9377	-110.1291	19.0	missing
LINE13.11	38.9376	-110.1292	7.8	missing
LINE13.12	38.9376	-110.1294	0.0	missing
LINE13.13mean	38.9374	-110.1296	5917.3	6414.7
LINE13.2	38.9382	-110.1256	0.0	401.3
LINE13.3	38.9381	-110.1258	0.0	404.1
LINE13.4	38.9380	-110.1263	0.5	408.0
LINE13.5	38.9380	-110.1267	0.5	410.2
LINE13.6	38.9379	-110.1270	0.0	404.0
LINE13.7	38.9378	-110.1274	5.9	414.4
LINE13.8	38.9376	-110.1281	55.7	454.9
LINE13.9	38.9375	-110.1286	56.0	474.3
LINE14.1	38.9353	-110.1180	0.0	396.6

Observation Name	Decimal Degrees Latitude	Decimal Degrees Longitude	CO_2 Flux ($g\ m^{-2}\ d^{-1}$)	Mean [CO_2] (ppm)
LINE14.10	38.9355	-110.1163	0.0	403.6
LINE14.11	38.9354	-110.1162	0.0	391.5
LINE14.12	38.9353	-110.1167	0.0	403.6
LINE14.13	38.9353	-110.1168	3.8	405.0
LINE14.14	38.9353	-110.1171	0.0	402.8
LINE14.15	38.9354	-110.1173	0.0	399.7
LINE14.16	38.9353	-110.1177	0.0	395.2
LINE14.2	38.9355	-110.1179	0.0	400.0
LINE14.3	38.9356	-110.1176	0.0	398.6
LINE14.4	38.9358	-110.1174	6.0	410.2
LINE14.5	38.9358	-110.1172	14.2	417.0
LINE14.6	38.9358	-110.1169	0.0	406.3
LINE14.7	38.9357	-110.1166	0.0	402.2
LINE14.8	38.9358	-110.1162	0.0	400.2
LINE14.9	38.9357	-110.1162	0.0	402.9
LINE15.1	38.9361	-110.1211	0.0	406.1
LINE15.10	38.9354	-110.1185	0.9	408.9
LINE15.11	38.9353	-110.1181	3.6	410.4
LINE15.12	38.9353	-110.1179	0.0	404.6
LINE15.13	38.9352	-110.1173	0.0	404.7
LINE15.14	38.9351	-110.1173	0.0	399.6
LINE15.15	38.9351	-110.1167	0.0	405.8
LINE15.16	38.9350	-110.1160	0.0	397.1
LINE15.17	38.9350	-110.1153	0.0	405.0
LINE15.18	38.9349	-110.1148	0.0	402.2
LINE15.19	38.9346	-110.1143	0.0	402.4
LINE15.2	38.9360	-110.1208	29.2	436.4
LINE15.20	38.9346	-110.1140	0.0	401.8
LINE15.21	38.9348	-110.1133	0.0	400.8
LINE15.3	38.9358	-110.1207	15.4	420.4
LINE15.4	38.9356	-110.1205	0.0	404.1
LINE15.5	38.9357	-110.1200	4.4	413.7
LINE15.6	38.9356	-110.1201	0.0	401.0
LINE15.7	38.9357	-110.1196	11.2	417.5
LINE15.8	38.9356	-110.1190	5.1	412.9
LINE15.9	38.9356	-110.1189	13.5	423.5
LINE16.1	38.9356	-110.1189	4.6	410.9
LINE16.10	38.9368	-110.1181	0.0	405.4
LINE16.11	38.9369	-110.1180	2.1	408.5
LINE16.12	38.9370	-110.1179	0.0	404.0

Observation Name	Decimal Degrees Latitude	Decimal Degrees Longitude	CO_2 Flux ($g\ m^{-2}\ d^{-1}$)	Mean [CO_2] (ppm)
LINE16.2	38.9359	-110.1186	1.2	405.7
LINE16.3	38.9361	-110.1184	0.0	401.8
LINE16.4	38.9362	-110.1181	0.0	403.2
LINE16.5	38.9362	-110.1184	1.1	407.0
LINE16.6	38.9363	-110.1185	5.3	411.8
LINE16.7	38.9364	-110.1185	2.9	409.1
LINE16.8	38.9365	-110.1184	0.0	404.5
LINE16.9	38.9366	-110.1183	2.1	407.8
LINE17.1	38.9362	-110.1174	14.9	419.8
LINE17.10	38.9387	-110.1160	4.8	408.6
LINE17.11	38.9382	-110.1150	3.1	406.6
LINE17.12	38.9383	-110.1141	1.0	405.1
LINE17.2	38.9365	-110.1173	8.9	415.1
LINE17.3	38.9367	-110.1169	10.0	415.3
LINE17.4	38.9370	-110.1170	4.7	409.3
LINE17.5	38.9372	-110.1171	7.6	411.6
LINE17.6	38.9375	-110.1170	3.3	407.4
LINE17.7	38.9379	-110.1172	15.0	417.6
LINE17.8	38.9379	-110.1166	4.2	408.7
LINE17.9	38.9382	-110.1162	4.4	408.6
LINE18.1	38.9370	-110.1121	0.0	402.4
LINE18.10	38.9362	-110.1086	19.1	missing
LINE18.11	38.9363	-110.1087	16.5	missing
LINE18.12	38.9361	-110.1088	0.8	405.8
LINE18.13	38.9361	-110.1091	7.2	missing
LINE18.14	38.9363	-110.1091	40.5	missing
LINE18.15	38.9363	-110.1091	29.9	missing
LINE18.2	38.9369	-110.1117	0.6	402.8
LINE18.3	38.9369	-110.1110	0.0	399.4
LINE18.4	38.9368	-110.1102	8.9	410.9
LINE18.5	38.9365	-110.1096	5.1	406.9
LINE18.6	38.9364	-110.1091	7.3	410.6
LINE18.7	38.9363	-110.1087	65.3	449.0
LINE18.8	38.9362	-110.1087	60.0	409.8
LINE18.9	38.9365	-110.1086	7.0	412.9
LINE19.1	38.9361	-110.1091	9.2	414.6
LINE19.2	38.9359	-110.1094	0.0	398.4
LINE19.3	38.9357	-110.1098	0.0	402.2
LINE19.4	38.9356	-110.1106	0.0	404.3
LINE2.1	38.9377	-110.1222	0.0	399.1

Observation Name	Decimal Degrees Latitude	Decimal Degrees Longitude	CO_2 Flux ($g\ m^{-2}\ d^{-1}$)	Mean [CO_2] (ppm)
LINE2.2	38.9373	-110.1220	46.5	472.0
LINE2.3	38.9371	-110.1217	0.0	405.1
LINE2.4	38.9369	-110.1216	12.9	414.0
LINE2.5	38.9368	-110.1215	20.0	424.7
LINE2.6mean	38.9366	-110.1211	887.7	1243.0
LINE2.7	38.9367	-110.1206	0.4	406.8
LINE2.8	38.9366	-110.1208	0.0	406.0
LINE2.9	38.9365	-110.1206	9.1	417.5
LINE20.1	38.9386	-110.1383	7.0	414.2
LINE20.10	38.9379	-110.1393	9.4	415.7
LINE20.11	38.9380	-110.1392	7.3	414.1
LINE20.12	38.9378	-110.1391	18.5	423.6
LINE20.13	38.9377	-110.1390	6.5	412.3
LINE20.14	38.9378	-110.1387	11.3	420.9
LINE20.15	38.9379	-110.1389	39.7	442.5
LINE20.16	38.9379	-110.1388	19.6	423.7
LINE20.17	38.9380	-110.1390	11.0	416.1
LINE20.18	38.9381	-110.1385	0.0	408.0
LINE20.2	38.9385	-110.1387	6.1	413.1
LINE20.3	38.9382	-110.1394	4.0	411.6
LINE20.4	38.9381	-110.1399	3.7	411.3
LINE20.5	38.9378	-110.1397	15.7	420.6
LINE20.6	38.9377	-110.1396	27.5	430.4
LINE20.7	38.9373	-110.1394	4.7	411.6
LINE20.8	38.9374	-110.1391	6.2	412.7
LINE20.9mean	38.9377	-110.1393	67.4	463.0
LINE21.10	38.9368	-110.1405	1.6	408.1
LINE21.11	38.9367	-110.1414	0.8	407.4
LINE21.1mean	38.9374	-110.1372	111.2	506.2
LINE21.2	38.9373	-110.1378	7.0	413.5
LINE21.3	38.9373	-110.1378	44.1	449.7
LINE21.4	38.9374	-110.1380	30.8	437.3
LINE21.5	38.9374	-110.1382	0.0	407.7
LINE21.6	38.9372	-110.1386	1.7	408.9
LINE21.7	38.9372	-110.1390	0.0	404.1
LINE21.8	38.9371	-110.1394	0.8	407.2
LINE21.9	38.9369	-110.1399	0.0	402.4
LINE22.1	38.9372	-110.1375	40.7	490.3
LINE22.10	38.9386	-110.1403	28.3	408.0
LINE22.11	38.9385	-110.1403	20.6	409.2

Observation Name	Decimal Degrees Latitude	Decimal Degrees Longitude	CO_2 Flux ($g\ m^{-2}\ d^{-1}$)	Mean [CO_2] (ppm)
LINE22.12	38.9385	-110.1397	4.2	410.9
LINE22.13	38.9387	-110.1394	18.9	410.9
LINE22.14	38.9388	-110.1390	6.1	411.9
LINE22.15	38.9386	-110.1389	2.0	409.3
LINE22.16	38.9384	-110.1394	0.0	401.8
LINE22.17	38.9383	-110.1399	19.5	410.4
LINE22.18	38.9383	-110.1402	26.0	missing
LINE22.19	38.9379	-110.1401	2.9	missing
LINE22.2	38.9375	-110.1375	24.8	431.3
LINE22.20	38.9378	-110.1403	67.5	missing
LINE22.21mean	38.9378	-110.1406	155.4	631.8
LINE22.22mean	38.9376	-110.1408	93.6	496.7
LINE22.23	38.9372	-110.1392	17.9	missing
LINE22.24	38.9373	-110.1387	7.2	missing
LINE22.25	38.9375	-110.1383	21.1	missing
LINE22.26	38.9377	-110.1383	14.9	missing
LINE22.27	38.9376	-110.1387	12.6	418.1
LINE22.28	38.9374	-110.1391	0.0	missing
LINE22.29	38.9375	-110.1398	1.6	missing
LINE22.3	38.9377	-110.1377	11.9	422.0
LINE22.4	38.9382	-110.1382	2.1	409.6
LINE22.5	38.9388	-110.1383	4.4	412.3
LINE22.6	38.9392	-110.1385	9.0	414.8
LINE22.7	38.9389	-110.1391	46.5	407.6
LINE22.8	38.9388	-110.1394	0.0	405.4
LINE22.9	38.9387	-110.1400	15.6	405.4
LINE3.1	38.9363	-110.1212	5.1	410.2
LINE4.1	38.9383	-110.1329	0.0	457.0
LiNE4.2	38.9380	-110.1330	0.0	406.5
LINE4.3	38.9377	-110.1330	0.2	406.5
LINE4.4	38.9376	-110.1330	1.4	406.8
LINE4.5	38.9373	-110.1330	2.7	405.9
LINE4.6mean	38.9375	-110.1330	147.3	516.7
LINE4.7	38.9374	-110.1335	9.7	411.3
LINE4.8	38.9372	-110.1333	0.0	400.5
LINE5.1	38.9388	-110.1318	4.5	409.5
LINE5.10	38.9370	-110.1325	0.0	399.4
LINE5.11	38.9370	-110.1329	0.0	401.6
LINE5.12	38.9372	-110.1328	7.3	409.5
LINE5.2	38.9384	-110.1319	53.7	454.5

Observation Name	Decimal Degrees Latitude	Decimal Degrees Longitude	CO_2 Flux ($g\ m^{-2}\ d^{-1}$)	Mean [CO_2] (ppm)
LINE5.3	38.9384	-110.1316	9.6	416.7
LINE5.4	38.9379	-110.1319	1.6	410.6
LINE5.5mean	38.9377	-110.1320	49.9	464.6
LINE5.6	38.9375	-110.1321	21.6	433.9
LINE5.7	38.9374	-110.1323	12.1	420.8
LINE5.8mean	38.9373	-110.1322	88.9	484.6
LINE5.9mean	38.9373	-110.1323	0.0	399.5
LINE6.1	38.9356	-110.1257	0.0	477.3
LINE6.10	38.9369	-110.1254	0.0	401.9
LINE6.11	38.9368	-110.1254	0.0	401.8
LINE6.2	38.9358	-110.1257	0.0	431.6
LINE6.3	38.9361	-110.1255	0.0	406.8
LINE6.4	38.9362	-110.1256	5.7	441.6
LINE6.5	38.9364	-110.1256	0.0	401.0
LINE6.6	38.9364	-110.1255	0.0	401.4
LINE6.7	38.9367	-110.1255	0.0	401.6
LINE6.8	38.9368	-110.1255	1.7	406.2
LINE6.9	38.9368	-110.1255	12.2	421.4
LINE7.1	38.9358	-110.1266	3.7	409.5
LINE7.10mean	38.9374	-110.1263	76.8	474.4
LINE7.11	38.9378	-110.1263	0.0	397.0
LINE7.2	38.9360	-110.1267	9.7	416.0
LINE7.3	38.9361	-110.1267	1.7	407.3
LINE7.4	38.9363	-110.1267	6.0	410.9
LINE7.5	38.9364	-110.1266	0.7	407.5
LINE7.6	38.9366	-110.1266	11.2	415.1
LINE7.7	38.9368	-110.1265	5.6	411.1
LINE7.8	38.9371	-110.1265	9.8	414.1
LINE7.9	38.9373	-110.1264	11.1	416.1
LINE8.10	38.9372	-110.1246	0.0	400.2
LINE8.1mean	38.9375	-110.1262	50.1	440.1
LINE8.2mean	38.9374	-110.1261	48.1	459.4
LINE8.3	38.9373	-110.1259	4.7	409.6
LINE8.4	38.9373	-110.1255	46.4	449.0
LINE8.5	38.9371	-110.1255	0.5	405.5
LINE8.6	38.9372	-110.1255	3.1	408.4
LINE8.7	38.9370	-110.1253	0.0	396.6
LINE8.8	38.9370	-110.1249	10.3	414.9
LINE8.9	38.9371	-110.1248	10.9	412.7
LINE9.1	38.9359	-110.1233	16.7	450.7

Observation Name	Decimal Degrees Latitude	Decimal Degrees Longitude	CO_2 Flux ($g\ m^{-2}\ d^{-1}$)	Mean [CO_2] (ppm)
LINE9.10	38.9359	-110.1264	0.0	398.6
LINE9.11	38.9359	-110.1269	0.0	399.1
LINE9.12	38.9359	-110.1274	0.0	397.9
LINE9.13	38.9360	-110.1278	0.0	396.8
LINE9.14	38.9361	-110.1282	0.0	392.2
LINE9.15	38.9360	-110.1287	0.0	396.5
LINE9.16	38.9360	-110.1293	6.0	409.8
LINE9.2	38.9361	-110.1238	0.0	403.1
LINE9.3	38.9361	-110.1243	2.8	407.0
LINE9.4	38.9360	-110.1247	0.0	400.7
LINE9.5	38.9361	-110.1249	5.6	407.3
LINE9.6	38.9360	-110.1251	0.0	404.4
LINE9.7	38.9359	-110.1255	0.0	403.7
LINE9.8	38.9359	-110.1258	0.0	400.4
LINE9.9	38.9359	-110.1263	1.6	408.1
LONG TERM T1&2	38.9379	-110.1339	3627.4	4412.1
LONG TERM T3&4	38.9380	-110.1340	1405.3	1812.2
STATIONARY1	38.9379	-110.1339	2682.1	3244.4
SW GEYSER1	38.9375	-110.1354	21.1	505.7
SW GEYSER2	38.9375	-110.1355	11.8	449.5

Appendix B

Soil Gaseous CO_2 Flux and Concentration Raw Data: the Salt Wash Fault Zone

Observation Name	Decimal Degrees Latitude	Decimal Degrees Longitude	CO_2 Flux ($g\ m^{-2}\ d^{-1}$)	Mean [CO_2] (ppm)
BBSL1.1	38.8712	-110.1125	34.9	408.9
BBSL1.10	38.8698	-110.1142	0.6	405.5
BBSL1.11	38.8700	-110.1142	0.0	404.0
BBSL1.12	38.8691	-110.1146	0.0	390.9
BBSL1.2mean	38.8711	-110.1116	80.6	467.7
BBSL1.3	38.8712	-110.1110	33.2	427.2
BBSL1.4	38.8710	-110.1122	1.3	406.5
BBSL1.5	38.8706	-110.1130	3.6	406.4
BBSL1.6	38.8703	-110.1135	0.0	402.9
BBSL1.7	38.8700	-110.1140	0.0	395.7
BBSL1.8	38.8699	-110.1141	0.0	403.4
BBSL1.9	38.8699	-110.1141	0.0	402.7
PTMLINE1.2	38.8661	-110.1003	24.8	424.1
SBSL1.1	38.8726	-110.1163	54.7	484.6
SBSL1.2	38.8725	-110.1169	19.0	420.0
SBSL1.3	38.8723	-110.1173	30.2	434.1
SBSL1.4	38.8721	-110.1179	22.1	428.8
SBSL1.5	38.8719	-110.1184	0.0	405.0
SBSL1.6mean	38.8716	-110.1188	111.2	485.8
SBSL1.7	38.8710	-110.1191	5.6	414.4
SBSL1.8	38.8701	-110.1202	0.0	404.7
SWFL1.1	38.8644	-110.0981	4.2	409.3
SWFL1.10	38.8651	-110.1026	26.6	427.0
SWFL1.11	38.8654	-110.1029	10.6	414.7
SWFL1.12	38.8657	-110.1032	34.3	403.7
SWFL1.13	38.8655	-110.1033	0.1	402.6
SWFL1.2	38.8643	-110.0985	3.9	408.8
SWFL1.3	38.8646	-110.0989	0.0	404.2
SWFL1.4	38.8643	-110.0993	1.6	406.2
SWFL1.5	38.8641	-110.0999	7.2	411.7
SWFL1.6	38.8644	-110.1009	3.7	408.7
SWFL1.7	38.8646	-110.1013	1.1	404.7
SWFL1.8	38.8650	-110.1018	8.9	413.4
SWFL1.9mean	38.8651	-110.1022	412.3	775.4
TMLINE1.1	38.8665	-110.1031	3.8	483.9
TMLINE1.2	38.8658	-110.1028	13.7	438.2
TMLINE1.3	38.8651	-110.1026	78.3	433.4
TMLINE1.4	38.8646	-110.1026	3.7	410.9
TMLINE1.5	38.8640	-110.1022	5.5	410.5
TMLINE1.6	38.8627	-110.1014	21.0	426.9

Observation Name	Decimal Degrees Latitude	Decimal Degrees Longitude	CO_2 Flux ($g\ m^{-2}\ d^{-1}$)	Mean [CO_2] (ppm)
TMLINE10.1	38.8680	-110.0996	31.2	401.2
TMLINE10.10mean	38.8681	-110.1018	119.8	520.8
TMLINE10.11	38.8678	-110.1015	3.0	407.4
TMLINE10.12	38.8676	-110.1021	5.7	409.9
TMLINE10.13	38.8672	-110.1025	45.0	458.2
TMLINE10.14	38.8672	-110.1018	0.0	401.4
TMLINE10.15	38.8673	-110.1012	2.3	406.6
TMLINE10.16	38.8668	-110.1012	12.1	413.2
TMLINE10.17	38.8667	-110.1020	1.7	406.8
TMLINE10.18	38.8667	-110.1027	27.3	437.4
TMLINE10.19	38.8566	-110.1031	3.3	410.2
TMLINE10.2	38.8676	-110.1001	3.0	408.0
TMLINE10.20	38.8662	-110.1029	8.2	410.0
TMLINE10.21	38.8662	-110.1036	4.9	410.4
TMLINE10.22	38.8657	-110.1035	0.0	402.1
TMLINE10.23	38.8657	-110.1036	0.0	396.4
TMLINE10.24	38.8656	-110.1040	0.0	403.4
TMLINE10.25	38.8655	-110.1047	0.0	401.3
TMLINE10.26	38.8661	-110.1046	0.4	405.4
TMLINE10.27	38.8665	-110.1045	7.7	413.8
TMLINE10.28	38.8663	-110.1039	0.4	404.6
TMLINE10.29	38.8662	-110.1039	0.0	399.2
TMLINE10.3	38.8677	-110.1009	3.7	409.3
TMLINE10.30	38.8652	-110.1041	0.0	395.9
TMLINE10.31	38.8650	-110.1041	0.0	399.1
TMLINE10.4	38.8680	-110.1013	2.9	407.9
TMLINE10.5	38.8685	-110.1013	2.4	415.2
TMLINE10.6mean	38.8685	-110.1012	61.5	463.3
TMLINE10.7mean	38.8685	-110.1019	73.0	475.8
TMLINE10.8	38.8686	-110.1022	35.2	442.4
TMLINE10.9	38.8683	-110.1017	2.2	407.1
TMLINE2.1	38.8631	-110.1010	4.5	403.6
TMLINE2.2	38.8637	-110.1008	3.5	405.5
TMLINE2.3	38.8642	-110.1006	4.9	410.3
TMLINE2.4	38.8646	-110.1001	7.9	409.9
TMLINE2.5	38.8648	-110.0999	3.0	408.2
TMLINE2.6	38.8654	-110.1000	7.4	416.0
TMLINE3.1	38.8659	-110.0995	11.2	414.3
TMLINE4.1	38.8660	-110.0949	0.0	426.3
TMLINE4.10	38.8638	-110.0974	0.0	395.1

Observation Name	Decimal Degrees Latitude	Decimal Degrees Longitude	CO_2 Flux ($g\ m^{-2}\ d^{-1}$)	Mean [CO_2] (ppm)
TMLINE4.11	38.8638	-110.0978	0.0	400.1
TMLINE4.2	38.8655	-110.0951	1.2	406.3
TMLINE4.3	38.8651	-110.0954	0.0	404.7
TMLINE4.4	38.8649	-110.0955	2.1	407.8
TMLINE4.5	38.8646	-110.0955	0.0	405.8
TMLINE4.6	38.8643	-110.0957	0.0	404.6
TMLINE4.7	38.8638	-110.0963	5.7	412.0
TMLINE4.8	38.8638	-110.0970	0.0	404.0
TMLINE4.9	38.8637	-110.0972	0.0	400.5
TMLINE5.1	38.8591	-110.0812	0.0	429.5
TMLINE5.10	38.8551	-110.0870	11.1	416.7
TMLINE5.11	38.8546	-110.0875	2.9	410.1
TMLINE5.12	38.8542	-110.0884	23.8	423.6
TMLINE5.13	38.8539	-110.0889	8.6	412.3
TMLINE5.14	38.8535	-110.0893	0.5	405.9
TMLINE5.15	38.8530	-110.0898	6.3	411.3
TMLINE5.16	38.8530	-110.0898	4.8	412.8
TMLINE5.2	38.8585	-110.0819	5.3	412.0
TMLINE5.3	38.8584	-110.0825	4.1	417.6
TMLINE5.4	38.8583	-110.0829	5.9	410.6
TMLINE5.5	38.8580	-110.0835	6.5	411.4
TMLINE5.6	38.8577	-110.0843	9.7	422.2
TMLINE5.7	38.8572	-110.0851	7.1	413.9
TMLINE5.8	38.8564	-110.0858	6.9	411.6
TMLINE5.9	38.8557	-110.0865	0.6	406.0
TMLINE6.1	38.8541	-110.0874	4.5	409.2
TMLINE6.10	38.8565	-110.0946	0.0	405.8
TMLINE6.11	38.8568	-110.0959	0.7	406.8
TMLINE6.12	38.8568	-110.0964	2.2	411.2
TMLINE6.13	38.8568	-110.0966	0.0	406.4
TMLINE6.14	38.8571	-110.0968	5.8	411.5
TMLINE6.15	38.8566	-110.0972	0.6	405.8
TMLINE6.16	38.8569	-110.0979	0.0	403.9
TMLINE6.17	38.8566	-110.0989	4.6	409.3
TMLINE6.18	38.8570	-110.0996	3.5	409.6
TMLINE6.2	38.8541	-110.0893	3.5	408.8
TMLINE6.3	38.8545	-110.0897	2.7	407.5
TMLINE6.4	38.8549	-110.0903	11.1	415.0
TMLINE6.5	38.8553	-110.0915	6.5	412.1
TMLINE6.6	38.8556	-110.0920	5.5	410.2

Observation Name	Decimal Degrees Latitude	Decimal Degrees Longitude	CO_2 Flux ($g\ m^{-2}\ d^{-1}$)	Mean [CO_2] (ppm)
TMLINE6.7	38.8560	-110.0930	1.4	406.8
TMLINE6.8	38.8561	-110.0932	0.3	405.4
TMLINE6.9	38.8562	-110.0937	3.4	409.4
TSL1.1	38.8587	-110.0727	5.7	490.6
TSL1.2	38.8579	-110.0738	0.0	416.6
TSL1.3	38.8563	-110.0755	1.1	407.1
TSL1.4	38.8559	-110.0765	4.2	409.7
TSL1.5	38.8557	-110.0773	1.1	406.5
TSL1.6	38.8552	-110.0783	0.0	401.7